UNIVERSITY OF CALIFORNIA, SAN DIEGO

Studies of Chlorophyll Dynamics using Moored Irradiance Sensors

A dissertation submitted in partial satisfaction of the requirements for the degree

Doctor of Philosophy

in

Oceanography

by

Samuel Johnson Wilson

Committee in charge:

Uwe Send, Chair
Peter Franks
Sarah Gille
B. Greg Mitchell
Geno Pawlak

2016

Dissertation of Samuel Johnson Wilson is approved, and it is acceptable in quality and form for publication on microfilm and electronically:

_____

_____

_____

_____

_____

Chair

University of California, San Diego

2016

TABLE OF CONTENTS

LIST OF FIGURES

LIST OF TABLES

ACKNOWLEDGEMENTS

I would like to thank my wife, she is everything to me.

Uwe Send played a role in each aspect of this thesis, especially the science. Thank you for your guidance and patience throughout my time at Scripps. The remaining members of my committee have also played an important role in my PhD.

Chapter 1, in part, is currently being prepared for submission for publication. Co-authors include Send, Uwe; B. G. Mitchell; D. Antoine. The dissertation author was the primary investigator of this material. The data were collected with California Current Ecosystem Mooring, California Cooperative Oceanic Fisheries Investigations, and the Buoy for the acquisition of long term optical time series (BOUSSOLE). The CCE moorings and some of this analysis work were supplemented by the NOAA Office of Climate Observation. The National Science Foundation, Graduate Research Fellowship also funded much of this analysis work.

Chapter 2, in part, is currently being prepared for submission for publication. Co-authors include Send, Uwe; B. G. Mitchell. The dissertation author was the primary investigator of this material. The data were collected from the California Current Ecosystem Mooring, and this research would not be possible without the Mooring Lab at Scripps Institution of Oceanography. The CCE moorings and some of this analysis work were supplemented by the NOAA Office of Climate Observation. The National Science Foundation, Graduate Research Fellowship also funded much of this analysis work.

Chapter 3, in part, is currently being prepared for submission for publication. Co-authors include Send, Uwe; D. Antoine; J. Uitz. The dissertation author was the primary

investigator of this material. The data were collected from the Buoy for the acquisition of long term optical time series (BOUSSOLE). The BOUSSOLE team at Laboratoire Oceanographique de Villefranche was instrumental in collecting that data. The National Science Foundation, Graduate Research Fellowship and Chateaubriand Fellowship funded this analysis work.

VITA

2009	Bachelor of Science, University of California, Los Angelos
2009-2010	Field Research and Personal Travel
2011-2016	National Science Foundation, Graduate Research Fellow
2011	Field work in Zanzibar, Tanzania
2013	Master of Science, University of California, San Diego
2014	Awarded Chateaubriand Fellowship to research at Laboratoire d'Océanographie de Villefranche-sur-Mer, affiliated with UPMC-Sorbonne
2015	Initial group for Global Environmental Leadership in Sustainability, group for high schoolers to Communicate Environmental Policy to Congress
2016	Ocean Science Meeting 2016, Planning Committee
2016	Doctor of Philosophy, University of California, San Diego

ABSTRACT OF DISSERTATION

Studies of Chlorophyll Dynamics using

Moored Irradiance Sensors

by

Samuel Johnson Wilson

Doctor of Philosophy in Oceanography

University of California, San Diego, 2016

Professor Uwe Send, Chair

Understanding oceanic chlorophyll dynamics requires new measurement methods and novel analyses. Moored irradiance sensors provide long time series of diffuse attenuation, and through a technique developed here, can provide estimates of average chlorophyll concentration between the sensors. This technique is applied to the California Current Ecosystem moorings, where simultaneous current measurements coupled with

the chlorophyll time series describe chlorophyll transport. Cross-shore transport events occur on timescales longer than 25 days in the offshore site, and account for offshore chlorophyll transport of 31.20 g/(day) per meter of coastline. In the near shore site, successive upwelling events transport large amounts of chlorophyll offshore, while single upwelling events do not. In total, events account for 94.80 g/(day) offshore chlorophyll transport per meter of coastline at this site. The method is then applied to recover 9 years of 0-9m chlorophyll concentration estimates in the Northwestern Mediterranean Sea. This region is dominated by a spring chlorophyll bloom, and the chlorophyll model used describes interannual variability in the initiation of this event by 25 days or more. During the bloom, hiatuses can occur where the 0-9m chlorophyll concentration decreases due to mixing, and they are often associated with Spring cooling events. The date of the last cooling event in January to April is a significant determinant of the delay in the 0-9m signature of the Spring Chlorophyll Bloom.

INTRODUCTION

Phytoplankton feed the base of the oceanic food web, convert inorganic carbon to organic carbon, and provide half of the oxygen we breathe. Understanding how these processes will change requires new tools to measure chlorophyll and new analysis methods. This need will be the focus of the thesis presented here, and several processes controlling chlorophyll growth and transport will be better understood by applying these new tools in two locations.

The current techniques for measuring chlorophyll resolve several spatial and temporal scales. Satellite chlorophyll provides excellent spatial coverage of surface chlorophyll, but lacks information below the surface and can be interrupted by clouds. Hydrographic sampling from research vessels provides information spanning many variables and can sample large regions [*Sosik and Mitchell*, 1995; *Bograd et al.*, 2003], but research vessels are expensive to operate and therefore lack temporal resolution. Biogeochemical floats and gliders provide information along a trajectory, but are restricted by the number of instruments they can hold [*Xing et al.*, 2012]. Moored fluorometers provide information at a single depth in tandem with other measurements, but are influenced by vertical movement of chlorophyll [*Franks*, 2005; *Antoine et al.*, 2006]. Moorings provide an opportunity for obtaining integrated chlorophyll measurements taken in tandem with other measurements, resolving daily to interannual changes in chlorophyll. Chapter 1 develops a method to determine vertically integrated chlorophyll using moored irradiance sensors.

This technique uses diffuse attenuation, a relatively easy quantity to measure. Multi-year time series of diffuse attenuation exist in several established moored systems around the world's oceans. In Chapter 2, the technique is applied to the California Current Ecosystem moorings (CCE1 and CCE2) to examine chlorophyll transport away from the California Coast near Point Conception. Chapter 3 uses the technique to examine nine years of the spring bloom in the Northwestern Mediterranean Sea using irradiance measured on the BOUSSOLE mooring. Though not discussed in this work, other potential applications of the technique include the M1 Mooring operated by MBARI [*Chavez et al.*, 2008] and the MOBY station near Hawaii [*Clark et al.*, 2002].

A major benefit from oceanic sampling using moored systems is the available measurement load. The CCE moorings have an ADCP measuring current profile information. Once the time series of chlorophyll concentration for the 0-80m or 0-40m layer is established, transport of chlorophyll past the mooring can be computed from the dot product of chlorophyll and currents. Fluxes of biogeochemical variables provide an understanding of the system, and here the offshore transport of chlorophyll is shown to occur in events that vary in duration and timing. Offshore, these events occur on 25+ day timescales and include both upwelling filaments and eddies. Near shore, upwelling transports large amounts of chlorophyll offshore, but only if consecutive upwelling events occur.

A second benefit for moored systems is the potential for measurement longevity. The BOUSSOLE mooring has sampled in the Northwestern Mediterranean since 2004, and presented here are results focusing on the spring bloom from 2004 to 2012. The

bloom timing varies on the order of ± 30 days in the North Atlantic [*Henson et al.*, 2009], and these results show that similar variation can occur in this region. The work then discusses hiatuses in the Spring bloom, where mixing events decrease surface chlorophyll concentrations, while integrated chlorophyll continues to increase. These events have been shown to increase vertical biogeochemical fluxes [*Bernardello et al.*, 2012] in ecosystem models, but observing them is difficult because of their sporadic and short nature. They are described using surface chlorophyll concentrations and upward heat fluxes.

This new method for chlorophyll concentration provides layer-integrated measurements in several regions. Daily measurements are able to identify the onset of an important feature, while interannual comparisons can describe how features vary from year to year. This tool and these analyses will aid in understanding oceanic chlorophyll, specifically how much there is and what it is doing.

CHAPTER 1: A NEW BULK CHLOROPHYLL RETRIEVAL USING PAIRED MEASUREMENTS OF WAVELENGTH-SPECIFIC DIFFUSE ATTENUATION

Introduction

Oceanic chlorophyll dynamics are controlled by several complicated processes, including physics of the medium, chemistry of the available nutrients, and biological growth. Understanding the interaction of these processes requires many types of chlorophyll measurements. Presented here is a method for estimating chlorophyll from moored measurements of irradiance.

The primary method for autonomous chlorophyll observation is fluorometric yield. This technique focuses on the photochemical response whereby phytoplankton emit photons at one wavelength due to excitation at another wavelength [*Mobley*, 1994]. This varies by species, time of day, and depth [*Horwood*, 1981; *Mobley*, 1994], and provides information only at a single depth. In contrast, the technique presented in this work focuses on absorption of light by chlorophyll, and provides information for a full water layer.

Chlorophyll absorption varies by a reproducible relation with chlorophyll concentration [*Bricaud et al.*, 1998; *Mitchell et al.*, 2000]. With higher chlorophyll levels, the diffuse attenuation of the water column increases, and less light reaches depth. Several studies have used the absorptive properties of chlorophyll to relate water column attenuation to chlorophyll level. [*Nahorniak and Pegau*, 2001] uses single depth

measurements, comparing the attenuation of irradiance at several wavelengths to estimate chlorophyll concentrations in model data. Bio-Argo is a program with radiometers and fluorometers fixed to Argo floats with [*Xing et al.*, 2012] using the paired irradiance and fluorescence profiles to assign the measured absorption into chlorophyll concentration and Chromophoric Dissolved Organic Matter (CDOM) absorption at 412 nm. [*Brown, C.A. et al.*, 2004] deployed a glider with a five-wavelength radiometer on the New Jersey shelf and computed chlorophyll concentrations using the derivative of the light field with depth. Though there has been work with moored irradiance sensors for the use biogeochemical sampling [*Chavez et al.*, 1997], to our knowledge, there has been no major effort to determine integrated chlorophyll using paired irradiance sensors from a mooring.

There are several time series where paired irradiance measurements exist, but no model for integrated chlorophyll has been developed. The California Current Ecosystem-Long Term Ecological Research Project (CCE) has two surface moorings on CalCOFI line 80 off Point Conception, spanning 5 and 7 years. The BOUSSOLE mooring operated through Laboratoire Oceanographique de Villefranche in the Northwest Mediterranean Sea has irradiance measurements over 11 years, with monthly cruises to calibrate the sensors for comparison with satellites [*Antoine et al.*, 2006]. Similarly, the MOBY time series near Hawaii uses monthly cruises to clean and calibrate sensors for satellite comparisons [*Clark et al.*, 2002]. Finally, the MBARI OASIS mooring has several years of interdisciplinary measurements, similarly featuring measurements of irradiance [*Chavez et al.*, 1997]. At these locations, it would be useful to have a method to

determine the surface integrated chlorophyll signal, and analyze the results alongside other physical or biogeochemical time series.

The work here develops a technique to infer the chlorophyll signal from paired measurements of irradiance. The model is tested with the data from hydrographic sampling programs in the optically diverse regimes off of California and in the Northwest Mediterranean.

Model Framework

The model is developed as a modular algorithm, diagrammed in figure 1.1. The basic idea is that the measured attenuation of light between the surface and depth across several wavelengths can provide the average chlorophyll concentration over the layer of water. Each module represents an optical property which is tested individually. Once the components have proven consistent and accurate, they are combined into the algorithm comprising the full chlorophyll retrieval method. The components of this modular algorithm include optical geometry, absorption constituents, and backscattering constituents. They are discussed briefly here and more in depth the following sections.

A model is developed that uses irradiance at two depths to describe the average chlorophyll concentration over that depth. Downwelling irradiance (E_d) decays exponentially with depth (z), following the Beer-Lambert Law;

$$E_d(z) = E_0 e^{-k_d z} \quad . \tag{1.1}$$

The term k_d is the measured, layer-averaged diffuse attenuation, and it is found by measuring irradiance at the surface (E_0) and the irradiance at depth (E_d), and solving for k_d ;

$$k_d = -\frac{1}{z}\log\left(\frac{E_d}{E_0}\right) \quad . \tag{1.2}$$

Diffuse attenuation has been used previously for in situ bio-optical algorithms [*Abbott and Letelier*, 1998; *Nahorniak and Pegau*, 2001; *Brown, C.A. et al.*, 2004; *Xing et al.*, 2012]. This is an apparent optical property (AOP), meaning it is dependent on light geometry. Inherent optical properties (IOP), including absorption (a) and backscattering (b_b) are independent of optical geometry. Previous bio-optical models use relationships to convert between IOPs and AOPs, for example,

$$\overline{k_d} = \overline{k_d}(a, b_b) \quad . \tag{1.3}$$

The overbar designates model representation of diffuse attenuation, and distinguishes it from the measured diffuse attenuation given in equation 1.2. Each term in this equation is dependent on wavelength (λ). The geometric approximation introduced by equation 1.3 is one of the algorithm's modules, and a simple relationship is discussed in the Light Geometry subsection.

Contributors to absorption include water (a_w), CDOM (a_s), and particulates (a_p), and the contributions to backscattering are due to water (b_{bw}) and particles (b_{bp}) [*Morel and Maritorena*, 2001]. The absorption and scattering properties of particles are dependent on chlorophyll concentration ($\langle chl \rangle$) [*Bricaud et al.*, 1998; *Morel and Maritorena*, 2001], and the absorption properties of CDOM are expressed using CDOM absorption at 412nm ($a_s(412)$) [*Bricaud and Prieur*, 1981]. Each of the absorption and backscattering components are represented in a module of the model. Combined, their form can be described as

$$\begin{aligned} a(\langle chl\rangle, a_s(412)) &= a_w + a_p(\langle chl\rangle) + a_s(a_s(412)) \\ b_b(\langle chl\rangle) &= b_{bw} + b_{bp}(\langle chl\rangle) \end{aligned} \quad . \tag{1.4}$$

As stated before, each term is also dependent on wavelength (λ). These equations are combined with equation 1.3 to give the full $\overline{k_d}$ as a function of ($\langle chl\rangle, a_s(412)$);

$$\begin{aligned} \overline{k_d}(\lambda) &= \overline{k_d}(a, b_b) \\ &= \overline{k_d}(\langle chl\rangle, a_s(412)) \end{aligned} \quad . \tag{1.5}$$

The goal of the model is to arrive at a $\overline{k_d}(\langle chl\rangle, a_s(412))$ that gives the best representation of the measured k_d spectrum. There are two assumptions associated with this goal; (1) the water being measured is case 1 waters [*Jerlov*, 1968], and therefore only chlorophyll, CDOM, and water contribute to the optical properties and (2) correctly representing the optical properties of the water column correctly represents the chlorophyll concentration present. Both of these assumptions are standard assumptions in open ocean bio-optical models [*Bricaud et al.*, 1998; *Morel and Maritorena*, 2001].

With all modules of the algorithm determined, the best representation is defined as the $\overline{k_d}(\langle chl\rangle, a_s(412))$ spectrum which provides the minimum of a least-squares cost function,

$$Cost(\langle chl\rangle, a_s(412)) = \sum_{\lambda} \left[k_d(\lambda) - \overline{k_d}(\lambda;\ \langle chl\rangle, a_s(412)) \right]^2 \quad . \tag{1.6}$$

To keep the solution overdetermined, at least three wavelengths of the diffuse attenuation spectra must be measured. The result is a layer-averaged chlorophyll concentration ($\langle chl\rangle$) and a layer averaged CDOM absorption at 412nm ($a_s(412)$) which best explains the measured diffuse attenuation spectrum.

Organizing the algorithm into modules allows users to replace individual pieces for their own preference. For example, CDOM has many different optical representations

[*Twardowski et al.*, 2004]. The modular nature also organizes model uncertainty, with each module having self-contained uncertainty that propagates through the full system. As each module is developed below, the values of associated variables and appropriate error are presented.

Instruments and Data

There are two major types of in situ data used in the model; IOPs derived from bottle samples to build the model, and radiometric measurements to apply it. The optical modeling program Hydrolight is used to build lookup tables of parameters which estimate optical geometry. The model is applied in both the California Current System (CCS) and the Northwest Mediterranean Sea; bottle samples and radiometric measurements are required in both locations, and the HydroLight Model runs are used across both geographies.

The two hydrographic programs used to develop and validate the model are the bio-optical portion of the California Cooperative Oceanic Fisheries Investigation (CalCOFI) hydrographic sampling operation undertaken by B. Greg Mitchell from 1992 to 2004 [*Sosik and Mitchell*, 1995; *Kahru et al.*, 2012] and the monthly sampling associated with the BOUSSOLE research mooring in the Northwest Mediterranean led by David Antoine. For each discrete bottle sample, laboratory hyperspectral measurements of particulate and CDOM absorption ($a_p(\lambda)$ and $a_s(\lambda)$, respectively) are found from using the filter and resuspension method [*Mitchell et al.*, 2000]. Simultaneous measurements of chlorophyll-a (chlorophyllids, and phaeopigment-a) are found using High Powered Liquid Chromotography (HPLC). Two representative examples of these

profiles of inherent optical properties and chlorophyll are given in figures 1.3. In total, there are 116 profiles of CDOM absorption spectra, particulate absorption, and chlorophyll concentration used from CalCOFI and 252 profiles of particulate absorption and chlorophyll concentration used from BOUSSOLE; example profiles and spectra are given in figure 1.3. Information for the CDOM absorption at BOUSSOLE is provided by Emanuele Organelli (personal communication), following a technique similar to that described in the Model Constituent section. The discrete spectra of a_s , a_p , and $\langle chl \rangle$ are used to calculate the various coefficients in the optical modules. For validation of the entire model, it is essential to have layer-averaged chlorophyll concentration.

The profiles of chlorophyll are linearly interpolated to 1m bins, and then averaged over appropriate depths (10m, 40m, and 80m) using a trapezoidal method, and assuming constant values above the top measurement. For a layer-averaged result to be used in this analysis, there must be at least two measurements over the depth of the layer (including 1 measurement above 10m) and measurements must extend to depths deeper than the layer depth. These layer-averaged measurements are used to derive validations of the technique.

During these same cruises, the AOP planar irradiance is measured at the surface (E_s) on the boat and at depth (E_d) using a radiometer attached to a CTD. The surface and depth irradiances are measured simultaneously, and referenced to the depth of the profiling instrument calculated using the CTD; the goal is to determine observed k_d using this information. First, any values are removed if the tilt sensor on the CTD

is registering a tilt greater than 1.5 degrees on either the E_s sensor or the E_d sensor; greater tilt results in less accurate reading of irradiance. Surface E_s and depth E_s run through a box-car mean filter equivalent to 6 meters of vertical movement of the E_d sensor. The surface measurement also has the reflective zenith angle applied to it from [*Neumann and Pierson*, 1966], which has an error of 2.54%. Measurements of k_d are then calculated using equation 1.2 for the full layer. The values associated with the depths of interest (10m, 40m, and 80m) are calculated as the mean value of layer diffuse attenuation collected within 3 meters of the desired layer depth. For a measurement to be valid, there must be at least 5 samples in this range and the standard deviation must be less than 5% of the mean. Finally, only those measurements for which the solar zenith angle is less than 70 degrees are used due to increased complications in light geometry [*Kirk*, 2010]. These restrictions limit the number of simultaneous layer-averaged diffuse attenuation and layer-averaged chlorophyll. For BOUSSOLE, there are 52, 33, and 38 usable measurements for the 10, 40, and 80m layers, respectively, and for CalCOFI there are 122, 81, and 11 spectra of $\overline{k_d}$ for layer depths 10, 40, and 80m, respectively. These measurements are used to validate the model.

Finally, runs from the widely accepted HydroLight Modeling [*Mobley and Sundman*, 2012] software provides lookup tables to convert from AOPs to IOPs in various light geometries. The HydroLight runs follow [*Lee et al.*, 2005], a previous method for calculating diffuse attenuation from absorption and backscattering. The technique derived by [*Lee et al.*, 2005] could be used for the light geometric module, but

it was unnecessarily complicated without a significant improvement in model accuracy. HydroLight model inputs follow [*Lee et al.*, 2005, paragraph 13], but expands on layer depths and zenith angle inputs for broader coverage. As in [*Lee et al.*, 2005], these inputs include absorption and backscattering spectra taken from the International Ocean Colour Coordinating Group (IOCCG) when $a+b_b$ is less than 0.5; their portfolio of values have absorption and backscattering values much greater than the optical regimes discussed here. As in [*Lee et al.*, 2005], the runs use a wind speed of 5 m/s providing a suitable approximation for estimates of surface reflectance [*Kirk*, 2010]. They also are run across separate particle phase functions (PPFs); these include Petzoldt with $b_b/b=1.83$, Fournier Fourand with $b_b/b=0.01$, Fournier Fourand with $b_b/b=0.04$, Morel large particles with $b_b/b=0.019$, and Morel small particles with $b_b/b=0.014$ [*Mobley*, 1994; *Morel and Maritorena*, 2001; *Mobley and Sundman*, 2012]. The goal for examining these different PPFs is to understand the variability of light geometry, instead of assuming that a single phase function dominates.

Constant profiles of $a+b_b$ are provided as inputs to HydroLight. Following a run, layer-diffuse attenuation is returned. The result is 0-10m, 0-40m and 0-80m layer-averaged values of a, b_b, and $\overline{k_d}$ for zenith angle 0 to 70 degrees spaced by 5 degrees for several realistic particle phase functions.

Light Geometry

The parameterization of light geometry is the major test of the algorithm's modularity. There have been many forms of this relationship [*Gordon*, 1989; *Lee et al.*,

2005; *Kirk*, 2010]. We introduce the most common method [*Gordon*, 1989], argued that it is incomplete, and then slightly modify it. This new technique, while imperfect, provides a useful and simple realization to convert between $\overline{k_d}$ and $a+b_b$.

Previous bio-optical models [*Abbott and Letelier*, 1998; *Nahorniak and Pegau*, 2001; *Brown et al.*, 2004; *Xing et al.*, 2012] that extract chlorophyll from diffuse attenuation use the [*Gordon*, 1989] geometric correction given in equation 1.3, specifically $\frac{\overline{k_d}}{D_0}=a+b_b$, to connect the layer-averaged values of diffuse attenuation to absorption plus backscattering. Equation 1.3 says that the light at any level is proportional to the average absorption and backscattering over that layer. When introducing the concept, [*Gordon*, 1989] stated that under ideal conditions, this path length correction term can be estimated as $D_0=1/\mu_d$. The term μ_d is the "average cosine", defined as downward planar irradiance (E_d) over spherical irradiance (E_0) [*Mobley*, 1994, chap.3];

$$\mu_d=\frac{E_d}{E_0} \quad . \tag{1.7}$$

This AOP is important in understanding sunlight geometry in the ocean and asymptotes in depth to a value determined by the IOPs [*Mobley*, 1994]. Near the surface, irradiance is approximately from a point source sun and at depth irradiance has been sufficiently scattered to be approximately isotropic [*Mobley*, 1994]. The average cosine value is not specifically dependent on water depth, but rather, the ratio of spherical and planar irradiance (equation 1.7). If $a+b_b$ increases over a given depth, the ratio given in

equation 1.7 changes, so assuming the D_0 or μ_d term is constant across different values of $a+b_b$ is incorrect.

HydroLight Optical Modeling Software has been used before to understand the relationship between $\overline{k_d}$ and layer $a+b_b$ [*Lee et al.*, 2005], and the HydroLight runs are defined in the Instruments and Data Section.

Figure 1.4 displays the relationship between $\overline{k_d}$ and $a+b_b$ for 412nm and 555nm at 20-degree zenith angle. Profiles of $k_d/(a+b_b)$ (figure 1.4, profile) display how this term asymptotes in depth, similar to μ_d [*Mobley*, 1994]. If $\overline{k_d}$ and $a+b_b$ were proportional, the profiles in figure 1.4 would have the same shape; this is not true.

The [*Gordon*, 1989] relationship states $\overline{k_d}$ and $a+b_b$ are proportional, so the best linear fit through this data would also go through the origin in figure 1.4. This assumption is easy to test, and ultimately proved inaccurate by figure 1.4; the best fit line for 412nm is approximately through the origin, but the best fit line for 555nm is significantly not through the origin. This module in the algorithm uses the best fit line through this data, with D_1 representing the multiplier and D_2 representing the offset. The new relationship can be presented as

$$K_d = D_1 \cdot (a+b_b) + D_2 \quad . \tag{1.8}$$

The terms D_1 and D_2 are functions of wavelength and solar zenith angle, and are found through linear regression pairs of HydroLight-derived ($\overline{k_d}$, $a+b_b$), providing a simple framework for lookup tables to be developed for these two variables. Following this, a given solar zenith angle and diffuse attenuation spectrum can be converted to a

spectrum of $a+b_b$.

Rather than choose a specific phase function, figure 1.4 and the lookup tables used for D_1 and D_2 use the linear fit through all the data available for various scattering phase functions. The uncertainty in this module is derived from the spread in the relationship between a HydroLight-returned k_d and a modeled $\overline{k_d}(a+b_b)$, and they are compared in figure 1.5 (middle row). Figure 1.5 describes the error for several modules, and the respective plots are introduced as their modules are discussed. The standard deviation of $\overline{k_d}/k_d$ is 0.088, and is assumed to represent the ability of the geometric correction to model diffuse attenuation. The error derived from the geometric correction of diffuse attenuation is 8.8%.

Model Constituents

In equation 1.4, the optical constituents are particle absorption (a_p), particle backscattering (b_{bp}) , solubles/CDOM absorption (a_s), and water absorption and backscattering (a_w+b_{bw}) [*Morel and Maritorena*, 2001]. The term "modules" is used in order to compartmentalize the concepts and errors associated with each optical constituent. They are discussed here:

Particles have both absorptive and backscattering scattering properties. Particulate absorption (a_p) is presented as an exponential function of chlorophyll [*Bricaud et al.*, 1998; *Mitchell et al.*, 2000];

$$a_p(\lambda,\langle chl\rangle)=A_p(\lambda)\langle chl\rangle^{E_p(\lambda)} \quad . \tag{1.9}$$

[*Bricaud et al.*, 1998] contains values for A_p and E_p , but they represent

measurements taken from a global dataset. The CalCOFI bio-optical and BOUSSOLE datasets provide local data, more accurately representing the phytoplankton for this region. Following [*Bricaud et al.*, 1998] figure 1.6 gives an example for the CalCOFI dataset; plots of concurrent samples of particulate absorption versus chlorophyll at 412nm and 510nm. Applying this method to hyperspectral measurements of particulate absorption from CalCOFI produces the spectra of both A_p and E_p given in figure 1.6; these spectra are interpolated at the wavelengths used in the model. The result is locally-derived coefficients for particulate absorption as a function of chlorophyll concentration.

Reverse solving equation 1.9 for each wavelength (i.e. using a_p to solve for $\langle chl \rangle$) returns a value of chlorophyll that would give the observed absorption; this value is averaged across each wavelength and compared with observed chlorophyll in figure 1.5 (top row). The error for this module is calculated by dividing this calculated chlorophyll ($\langle chl \rangle (a_p)$) by the HPLC-measured $\langle chl \rangle$ (figure 1.5), and arriving at a standard deviation of a percentage of the true value; this is divided by the square root of the number of wavelengths present to obtain standard error. The result is a standard error of 4.32% associated with particulate absorption, which is applied directly to model output.

Backscattering by particulates is represented by [*Morel and Maritorena*, 2001] equations 13 and 14 ;

$$b_{bp} = \left\{0.002+0.01\left[0.50-0.25\log_{10}\langle chl\rangle\left(\frac{\lambda}{550}\right)\right]\right\}\left[0.416\langle chl\rangle^{0.766}\right]$$
$$\nu = \begin{cases} 0.5\left(\log_{10}\langle chl\rangle-0.3\right), & \text{for } 0.02<\langle chl\rangle\le 2\, mg\, m^{-3} \\ 0, & \text{for } \langle chl\rangle>2\, mg\, m^{-3} \end{cases} . \qquad (1.10)$$

When $\langle chl\rangle<0.02\, mg/m^3$, backscattering is considered negligible. The simplification given by equation 1.10 is advantageous to apply in a bio-optical model for being dependent on chlorophyll, but this assumption must be described during error considerations. In the model, this description of backscattering is assumed to have a 10% error, roughly the range in particulate backscattering for a doubling of chlorophyll [*Morel and Maritorena*, 2001].

CDOM represents dissolved detritus, phytoplankton waste, and terrestrial runoff; it is often called gelbstoff matter, yellow matter, or solubles [*Mobley*, 1994; *Bricaud et al.*, 1998]. The spectral properties of solubles has been shown to vary by composition, location, and water column history, but its most consistent feature is a negative exponential for the spectral absorption slope [*Bricaud and Prieur*, 1981]; this model assumes a function of the form

$$a_s(\lambda, a_s(412)) = a_s(412)\exp(-s(\lambda-412)) \quad . \qquad (1.11)$$

Both datasets have CDOM absorption spectra available, providing a determination of the s term. In CalCOFI, equation 1.11 is fit to 1127 soluble absorption spectra, arriving at the distribution in figure 1.5 (bottom) for values of s ; it has a mean of -0.024 and a spread of 17%. Through personal communication with Emanuele Organelli, the s value for BOUSSOLE is -0.018 with the same assumed spread of 17%.

Water absorption (a_w) and molecular backscattering (b_{bw}) are taken from literature values.

Water absorption parameters are taken from [*Pope and Fry*, 1997], who also provided error estimates. Molecular backscattering by water (b_{bw}) is assumed isotropic [*Morel*, 1974], so forward scattering and backscattering are equivalent; the backscattering by water is taken as ½ the total scattering by water given in [*Morel*, 1974]. Both water absorption and backscattering are assumed to have a 2% associated error.

Model Application and Validation

The full model representation of $\overline{k_d}$ for each wavelength (λ) is repeated here:

$$\begin{aligned} \overline{k_d}(\langle chl \rangle, a_s(412)) &= D_1\left[a(\langle chl \rangle, a_s(412)) + b_b(\langle chl \rangle)\right] + D_2 \\ a(\langle chl \rangle, a_s(412)) &= a_w + a_p(\langle chl \rangle) + a_s(a_s(412)) \\ b_b(\langle chl \rangle) &= b_{bw} + b_{bp}(\langle chl \rangle) \end{aligned} \quad , \qquad (1.12)$$

Equations 1.9, 1.11, and 1.10 are used for the wavelength-dependent terms a_p , a_s , and b_{bp} , respectively. Coefficients in equations 1.9 and 1.11 are derived from the CalCOFI bio-optical dataset and BOUSSOLE monthly cruises, while the representation of 1.10 and a_w and b_{bw} are from the literature. The $D_{1,2}$ coefficients are found using HydroLight, and are dependent on layer depth and zenith angle, and scattering phase function.

The terms $\langle chl \rangle$ and $a_s(412)$ in equation 1.12 are unknown and found using the cost function (equation 1.6) through a least-squares method using the Nelder-Mead algorithm. This algorithm finds a minimum if the error space is smooth [*Nelder and Mead*, 1965]; the error space is assumed smooth with figure 1.7 showing a representative example from the CalCOFI dataset.

In both the BOUSSOLE monthly sampling and CalCOFI bio-optical datasets, concurrent chlorophyll samples provide a direct method to validate results. Results for the three layers of interest (10m, 40m, and 80m) are compared with measured values at both location in figure 1.8. These results are promising except for some outliers in the 40m CalCOFI and 80m BOUSSOLE model-returned values. More work is being completed which may explain these outliers, including using dynamic CDOM representation or more rigorous quality control on irradiance profiles. .

The spread of the model changes with depth, in particular that 10m values have more spread than 40 or 80m values. It is well known optical geometry is most complicated and sensor movement is more prevalent near the surface [*Zaneveld*, 1989]. The effect of sensor movement has been minimized by fitting the E_d profile in to a straight line in logspace (equation 1.2), and ray focusing is minimized by taking the 6 meter median of the diffuse attenuation. Despite these corrections, errors in diffuse attenuation are elevated at the surface, causing larger errors in the model-returned chlorophyll.

The effect of overcast or cloudy days can be examined by comparing model results beneath cloudy or sunny skies. The [*Gregg and Carder*, 1990] model is applied for each datum to find expected sunny-sky irradiance, which gives an average factor (f) between observed (E_s) and expected (E_g) irradiance; $E_s = f * E_g$. Using this model, "sunny" measurements are defined as close to f=1.0 and E_s measurements which deliver a value significantly less than f=1.0 are either cloudy, partly cloudy, or otherwise flawed. In general, cloudy or overcast measurements do not drastically affect

model accuracy; the returned values lie within the standard spread seen by the model without a systematic offset. For this reason, model-returned values during cloudy days are considered accurate. If f >1.0, then either reflection off of clouds is increasing irradiance [*Gregg and Carder*, 1990] or the tilt is too large and the instrument is directly facing the sun [*Mobley*, 1994]. This causes the diffuse attenuation to be overestimated, causing the model to assign more chlorophyll with the model to explain elevated diffuse attenuation; the most striking example occurs for the 10m BOUSSOLE, where sunlight levels on a single observation were described as approximately two times the maximum estimated from [*Gregg and Carder*, 1990] applied for BOUSSOLE data. Those instances where f>1.3 are deemed outside of possible sunny values, and ignored.

Error Analysis

The model consists of several modules each with an associated error. A full understanding of error is provided once the individual sources of errors are combined. The model is run in a Monte Carlo technique through 200 iterations for each measurement. Normally distributed, random numbers are associated with the appropriate coefficients. For example, the s_n used for the model has an associated 17% error; therefore, $s_n = s_{real}(1 + randn * 0.17)$, where randn is a standard normally distributed random number, and s_{real} is the appropriate s term found for each geographic location.

Each of these sources of errors was discussed as their module was introduced, and briefly repeated here. The CDOM was used as an example in the preceding paragraph. Particle absorption imposes a 4.32% error applied to the chlorophyll value

returned by the model. Particle backscattering, water absorption, and water backscattering are assumed to have a 2% error. Diffuse attenuation receives error from assumptions about reflectiveness of the ocean surface (2.54%) and issues with the assumptions about the geometry of light (8.8%). These irradiance errors result in a ~10% applied to each $k_d(\lambda)$ measurement. The median value for each 200 iterations is chosen as the value for that measurement, and displayed on figure 1.7. The vertical spread associated with each measurement are derived from the one (thick) and two (thin) standard error of the average.

Discussion

Moorings allow long-term, continuous measurements that can be used to connect chlorophyll measurements with other time series. An algorithm that returns layer-averaged chlorophyll concentration has been developed. One of the primary features is the algorithm's modularity, as it combines theory for optical geometry, absorption, and backscattering. The opportunity exists for additional modules. For example, a linear adjustment could be applied to the 40m results from CalCOFI when chlorophyll levels are high.

This model has been shown to return realistic chlorophyll for three surface layer depths in two locations with different phytoplankton assemblages, CDOM spectral shapes, latitudes, and cloud estimations. It can directly be applied to paired measurements of diffuse attenuation measured with moorings, or potentially augmented for diffuse attenuation measured from floats or gliders. In order to apply it in those locations, it is important to understand which coefficients need to be calculated locally for the model to

accurately return chlorophyll concentrations. It is shown that particulate coefficients from a general dataset can be used without a large drop in accuracy; however, the representation of CDOM must use locally-derived values.

Absorption due to phytoplankton varies by light availability, life stage, and species. This variance is easily visible in figure 1.6 where A_p and E_p spectra are plotted for BOUSSOLE and CalCOFI. Due to the compartmental nature of the model, the effect of different A_p and E_p values can be easily tested by replacing the dataset-specific with more general [*Bricaud et al.*, 1998] values. When this occurs, the effect is minimal, so local coefficients in particulate absorption are not entirely necessary.

Absorption due to CDOM has a wider range for its functional representation, well documented in the literature [*Bricaud and Prieur*, 1981; *Twardowski et al.*, 2004; *Organelli et al.*, 2014]; here, s =-0.018 at BOUSSOLE and s =-0.024 at CCE. Although the model again allows applying more general values for s, the application would be inappropriate as s has such a wide range. Switching these values degrades model accuracy. Without knowledge of CDOM absorption, it is suggested to use s=-0.018, while a better representation could be gained from region-specific estimations of s.

This bio-optical model can be applied to measurements of layer-averaged diffuse attenuation. In particular, moorings with paired irradiance sensors such as CCE, BOUSSOLE, MOBY, and MBARI-M1 station provide an immediate system on to which this model can be applied. If measurements of a_p, $\langle chl \rangle$, and a_s are available, local-specific coefficients (A_p, E_p, and s) for the bio-optical constituents would provide the best representation of layer-averaged chlorophyll. Without those

measurements, the [*Bricaud et al.*, 1998] (A_p , E_p) values and $s=-0.018$ can be used. As with all science, the model-returned values should be verified against conventional chlorophyll methods to provide data closure.

Concluding Remarks

The power of moorings as a tool for oceanic measurements is in their long-term deployments, sample frequency, and measurement load. A long-term mooring deployment is useful in analyzing trends, while the high frequency sampling allow for small-scale variability to be quantified. Interesting applications combine these two temporal scales. For example, the initiation of the spring bloom at the BOUSSOLE site is not fully understood, and satellite methods which sample once a week often do not capture the specific day on which a bloom initiates. With this method applied to the paired radiometers at the BOUSSOLE site, coupled with the wind and air/sea temperature measurements, the current models for bloom initiation can be investigated. This application of the model would capture the interannual variability of a process which varies by only a few days.

There is also the possibility of using the model-returned chlorophyll to understand the importance of various timescales. With a long enough time series, information can be broken into frequency bands approximately representing different oceanographic features. In the California Current System, upwelling features last approximately 12-30 days, and account for large blooms in chlorophyll. Meander and eddy shearing of the California Current Jet often appear in the signal on longer timescales. With the technique presented in this work applied to the CCE moorings, coupled with the current

measurements, an understanding which features control chlorophyll variability and/or chlorophyll transport could be gained.

Chapter 1, in part, is currently being prepared for submission for publication. Co-authors include Send, Uwe; B. G. Mitchell; D. Antoine. The dissertation author was the primary investigator of this material. The data were collected with California Current Ecosystem Mooring, California Cooperative Oceanic Fisheries Investigations, and the Buoy for the acquisition of long term optical time series (BOUSSOLE). The CCE moorings and some of this analysis work were supported by the NOAA Office of Climate Observation. The National Science Foundation, Graduate Research Fellowship also funded much of this analysis work.

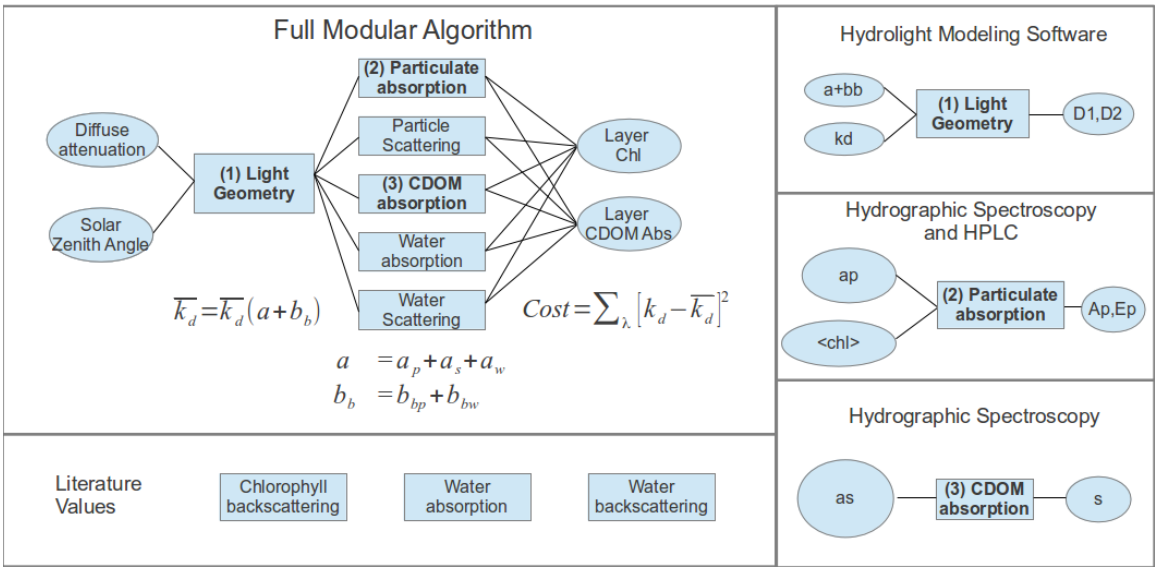

Figure 1.1: A schematic outlining the full algorithm presented in this model; ovals represent data types while rectangles represent modules of the algorithm. The goal is to minimize the difference between spectra of measured attenuation and model attenuation. The modules represent individual components of the model, and their derivation is examined more closely in the boxes around the outside. The (1) light geometry module is derived through Hydrolight Modeling Software. The (2) particulate absorption module is derived through hydrographic sampling of chlorophyll and radiometric spectroscopy. The (3) CDOM absorption module is derived through hydrographic spectroscopy. The other modules (chlorophyll back scattering and water absorption/back scattering) are determined through literature values. Each of these are reviewed more closely in the text.

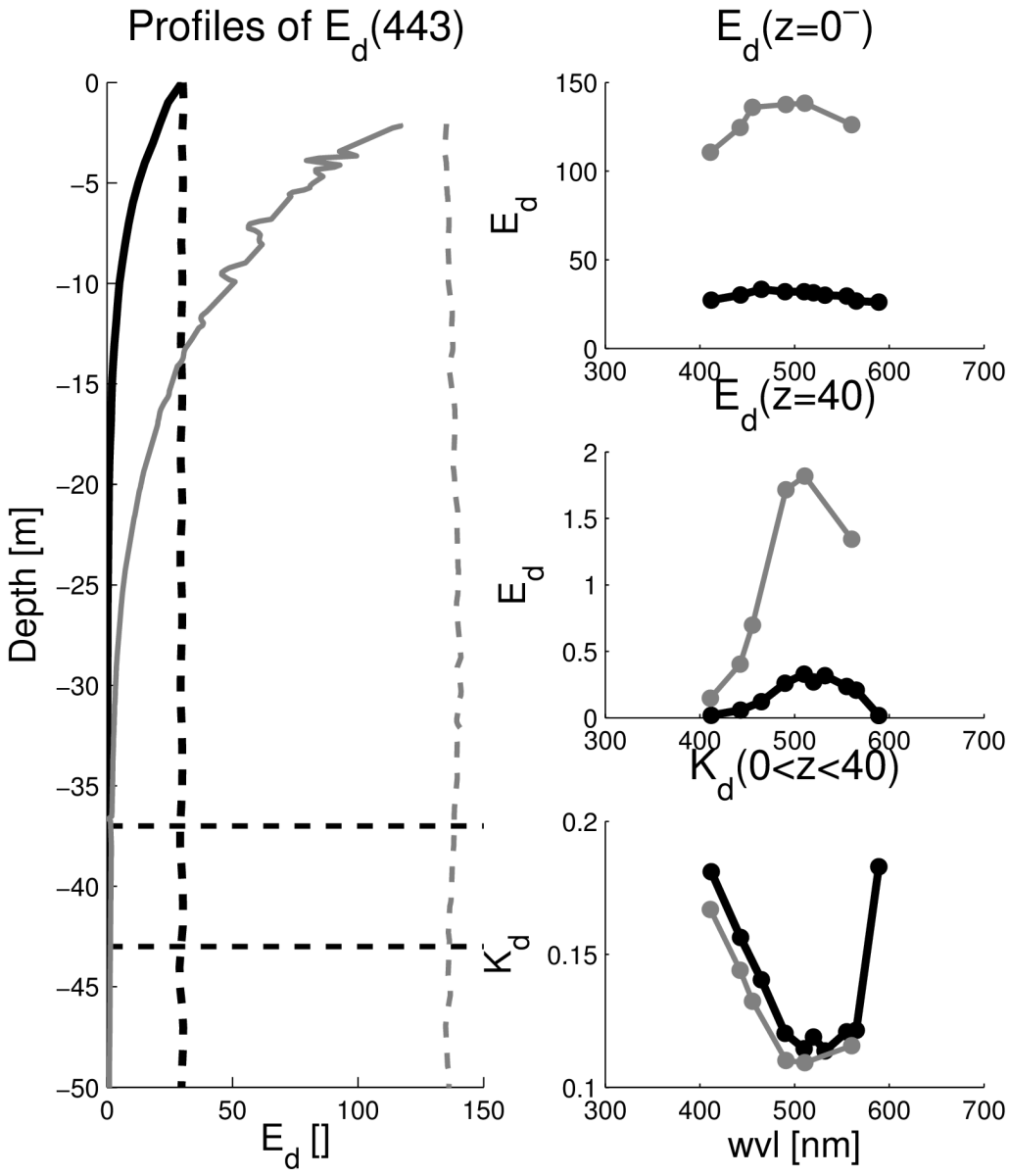

Figure 1.2: One representative sample of shipboard-measured Apparent Optical Properties from CalCOFI (black) and BOUSSOLE (gray). (left) Irradiance profiles measured using a profiling instrument in solid. The vertically dashed lines are the simultaneous surface measurement, referenced to the depth of the instrument below the surface during that same time. The horizontal dashed lines represent the depth of interest (40 +/-3 m). The average spectra of (top right) surface irradiance spectra and (middle right) depth irradiance for measurements taken between the dashed lines in the profile (40 +/- 3m). (bottom right) The diffuse attenuation spectra, calculated between the surface and depth instruments using equation 1.1.

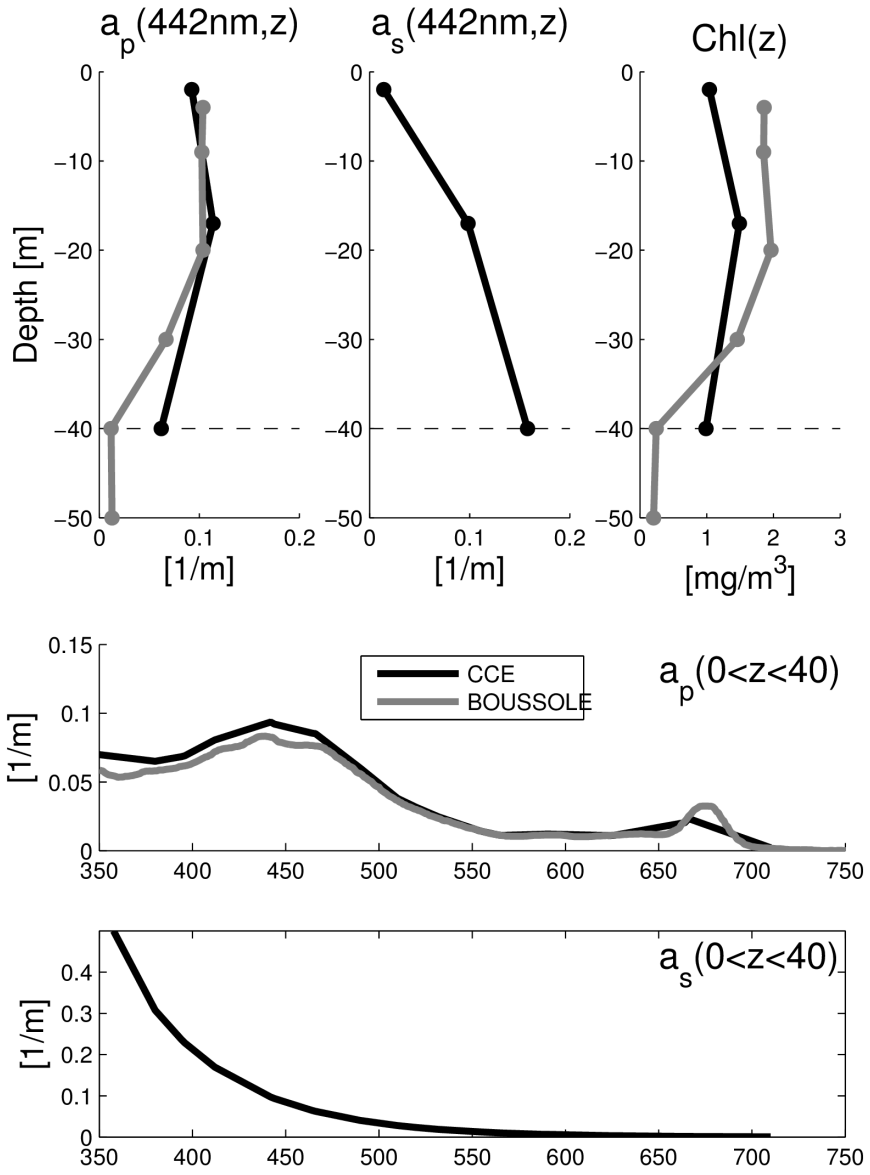

Figure 1.3: One representative sample of shipboard-measured Inherent Optical Properties of CalCOFI (black) and BOUSSOLE (gray). Profiles of (top, left) Absorption due to particulates, (top middle) absorption due to CDOM (data not available for BOUSSOLE), (top right) chlorophyll concentration. For each profile, the average is calculated by integrating using trapezoidal method and dividing by depth. (middle) and (bottom) give the surface averaged absorption spectra due to particulate and CDOM, respectively.

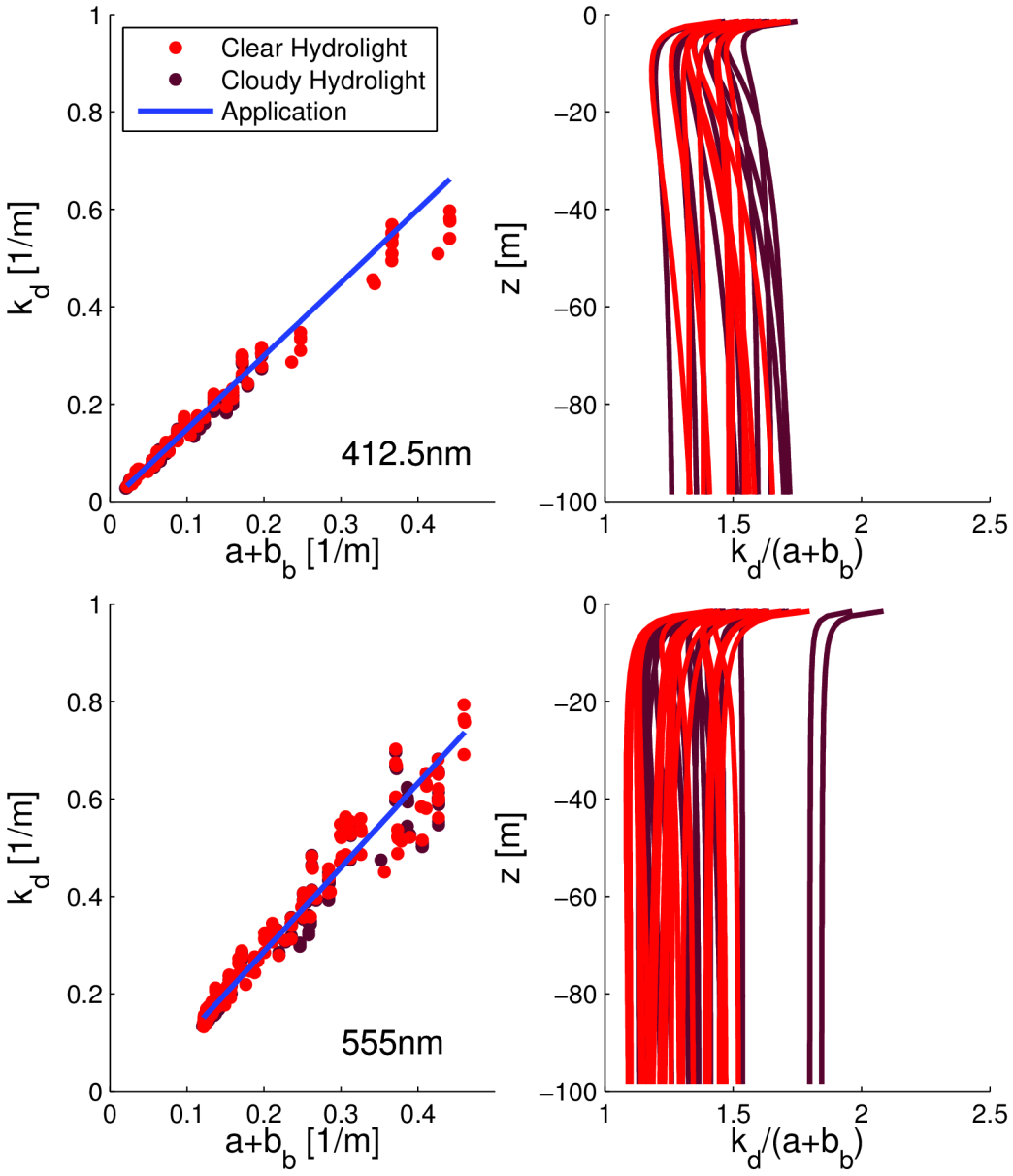

Figure 1.4: Hydrolight is run with a collection of (a, b_b) values taken from IOCG standard values at a selection of zenith angles, arriving at profiles of irradiance, from which diffuse attenuation (k_d) can be found. (top left) Layer diffuse attenuation versus absorption plus backscattering at zenith angle of 20 degrees for 412.5nm (top) and 555nm (bottom). The Geometric relationship used in this model fits the straight blue line to all of the data for a given wavelength and solar elevation combination. (right) The term $D_0 = k_d / (a + b_b)$ plotted versus depth. It is similar to $1/\mu_d$ with it's asymptotic feature.

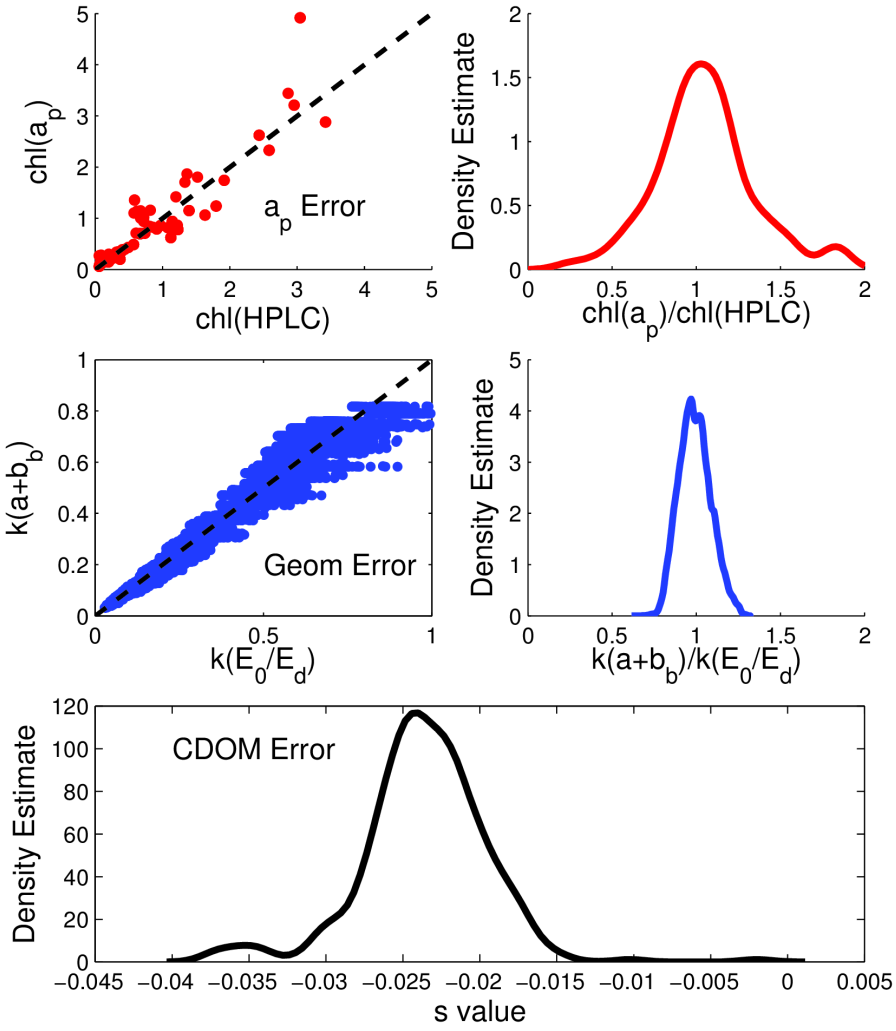

Figure 1.5: Each of the modules has associated error, and three modules have spread represented here. Reverse solving equation 1.9 from absorption returns a $chl(a_p)$ from each wavelength; (top left) is the mean $chl(a_p)$ across each wavelength versus the measured chl(HPLC); the standard deviation of this ratio is 0.0942. (top right) is the spread of ratio chl(a_p)/chl(HPLC) which gives a percentage of error associated with variations in a_p. Hydrolight is used in the geometric relationship deriving equation 1.8; (middle left) is $k_d(a+bb)$ by equation 1.8 versus $kd(E_0/E_d)$ by equation 1.4. The spread can be found as a percentage using the ratio of $kd(a+b_b)/kd(E_0/E_d)$; the standard deviation of this relationship is 0.088. (Bottom) gives the distribution of s found by applying equation 1.11 to CalCOFI Bio-optical data; the mean is -0.024 $1/m$ and the standard deviation is 0.0041 $1/m$.

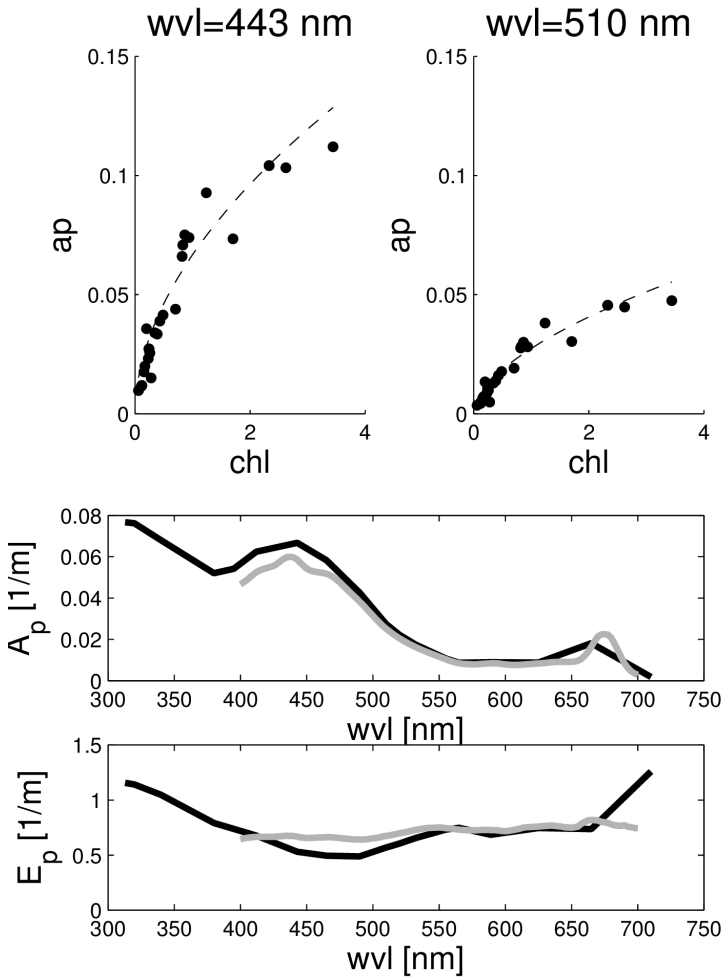

Figure 1.6: (Top) Relationship between particulate absorption and chlorophyll for 443nm and 510nm; the dots are layer-averaged values for absorption and chlorophyll, and the dashed line is the a_p(chl) relationship determined by equation 1.9. In reverse, this attributes a chlorophyll "model value" to a given absorption measurement. (Middle) The spectra of the coefficients for equation 1.9., with California as Gray and BOUSSOLE as black (Bottom) The factor between the "model value" using chl(a_p) for each wavelength versus the measured chlorophyll.

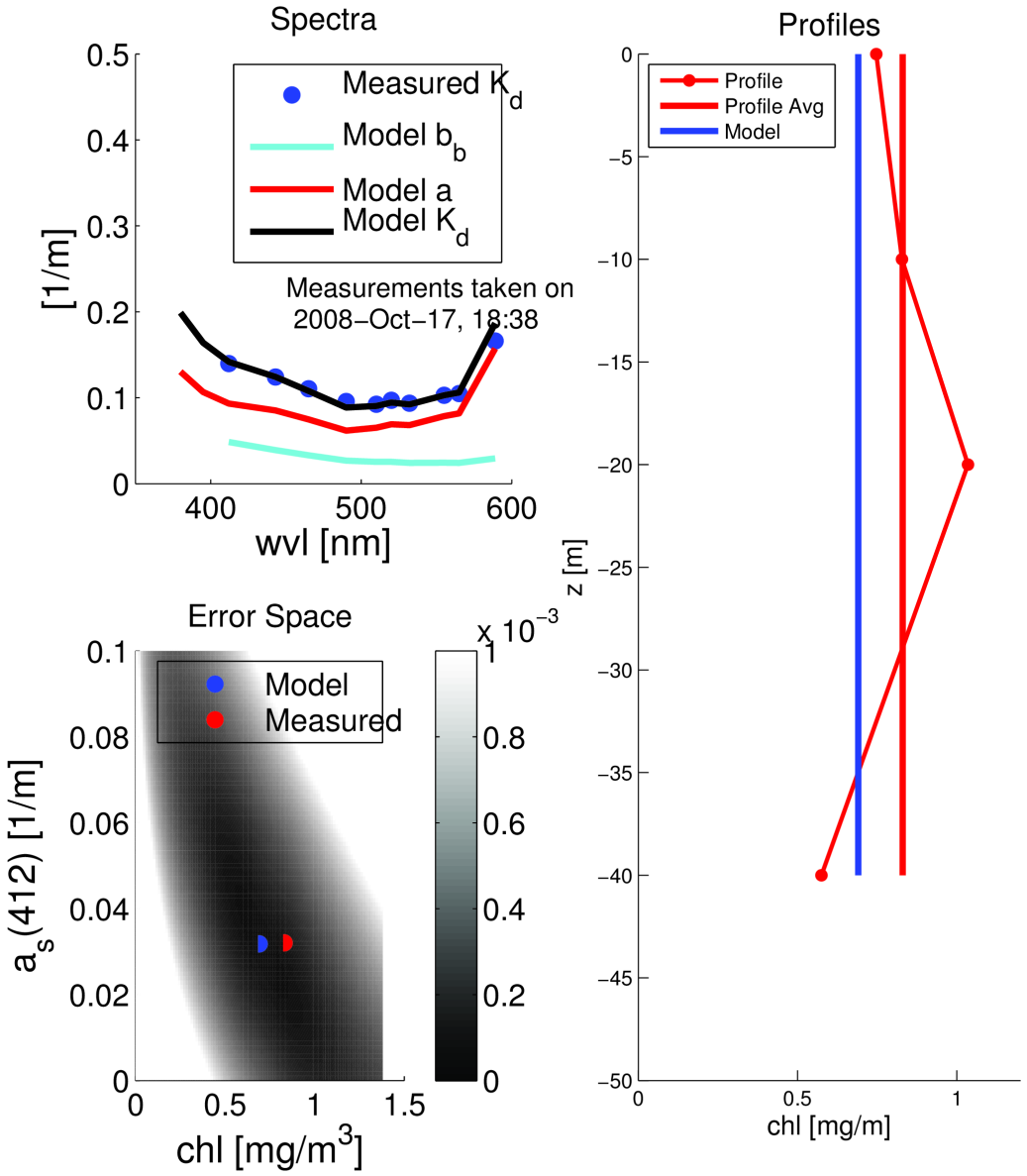

Figure 1.7: The model is applied k_d measurements and compared with chlorophyll profiles. (top left) spectra of measurements (blue dots) and model returned values (lines). (bottom left) gives the error space for various combinations of ($\langle chl \rangle$, $a_s(412)$); the model optimizes within this space and returned the value at the blue dot, while the red dot is the value measured from the bottle samples. (right) the profile of chlorophyll (red with dots) is averaged (solid red) and compared with the model-returned value (blue).

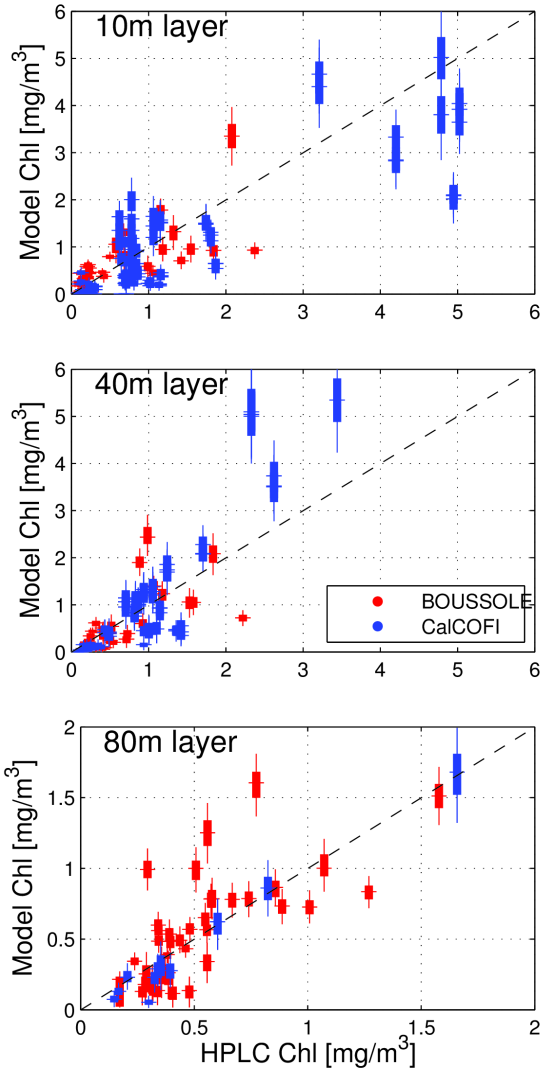

Figure 1.8: Comparison of model-returned chlorophyll values versus chlorophyll values for BOUSSOLE (red) and CalCOFI (blue), for each of 10m (top), 40m (middle), and 80m (bottom). The spread in the y-direction derives from the Monte-Carlo handling of error; this is a compilation of 200 runs with random numbers used to handle errors in the various modules. The thick lines represent the 68% distribution, while the thin lines represent the 95% distribution.

CHAPTER 2: SPATIAL AND TEMPORAL SCALES OF CROSS-SHELF CHLOROPHYLL TRANSPORT OFF POINT CONCEPTION

Introduction

Upwelling systems are an important component of the Oceanic Carbon System, and the California Upwelling System is one of the most studied upwelling systems in the world. Still, the processes transporting carbon between the coast and the open ocean are poorly understood.

The California Current Ecosystem Project (CCE) has two biogeochemical moorings in two major regimes. In the near shore, CCE2 measures in the core of the upwelling regime, where northerly winds drive coastal Ekman pumping, elevate chlorophyll levels, and move water offshore. In the offshore, CCE1 measures in the core of the southward-flowing California Current that oscillates both in distance from the shore and direction. Figure 2.1 gives a map of these two moorings in the context of the ongoing hydrographic sampling program CalCOFI and a representative diagram of the instruments on CCE1. The CCE1 moorings provide physical, chemical, and biological measurements to understand the temporal variability of this dynamic system. Measurements from the moorings include radiometers returning diffuse irradiance at the surface and at depth and an ADCP returning current velocity. These long-term research platforms provide an understanding of chlorophyll transport to the offshore at both locations.

Previously, [*Wilson et al.*, 2016] developed a technique to give chlorophyll concentration using layer-averaged diffuse attenuation. That work was specifically developed with moored measurements in mind, and is directly applied to CCE measurements to obtain over 5 years of layer-averaged chlorophyll concentrations at the CCE moorings; simultaneous ADCP then estimate the currents for the same layers. Combining these measurements provides the chlorophyll transport past the mooring, with 1317 days of chlorophyll transport measurements at CCE1 and 1245 days of measurements at CCE2.

From these estimates of chlorophyll transport, the advection due to the mean flow and the advection of chlorophyll due to events can be studied. Although the processes differ at each mooring, in both locations the cross-shelf transport of chlorophyll is shared between the mean flow and event-scale advection. Further, the event-scale advection of chlorophyll can be associated with specific frequency bands; chlorophyll transport at CCE2 is dominated by the upwelling season (though not necessarily specific upwelling events), and CCE1 chlorophyll transport is dominated by oscillations in the California Current.

The data section applies the [*Wilson et al.*, 2016] chlorophyll retrieval to moored measurements on the CCE moorings and describes ADCP and temperature sensors. The Methods section breaks apart chlorophyll transport into mean and event-scale, and determines their relative importance in cumulative transport. The Results section discusses these results in the context of the full time series and several examples. Finally, the Discussion section provides context for these measurements and suggests future

work.

Data

Chlorophyll Model

The chlorophyll presented here is found through an application of [*Wilson et al.*, 2016] to moored measurements. That model uses irradiance measured from radiometers at two depths to return bulk diffuse attenuation for the layer of water between the two sensors (see figure 1.1). The representation of chlorophyll here follows precisely the technique presented in that work. It is still necessary to discuss the data preparation.

Instrument-returned irradiance is calibrated for each deployment, arriving at a diffuse attenuation. The algorithm defined by figure 1.1 is applied, with the same optical coefficients as derived from the CalCOFI measurements in that work. The result is a chlorophyll value for the 40m layer at CCE2 or 80m layer at CCE1. In [*Wilson et al.*, 2016], the model components are referred to as modules, and coefficients and errors within each module are calculated independent of other modules. Introducing the measurements from a mooring introduces additional steps, and therefore additional errors. Those steps along with their error are discussed here.

Calibrating Irradiance Measurements

The model requires accurate measurements of irradiance just below the surface and at depth. The accuracy of the measurements returned by the sensors is influenced by the calibration factors provided by the manufacturer. This takes the form

$$E = F \cdot (V - N) \quad , \tag{2.1}$$

where F is scale factor, V is voltage returned by the sensor, N is dark counts, and E is irradiance using these calibration factors. The surface measurements undergo three analyses in order to return accurate measurements just below the surface; (1) determine which deployments have incorrect factory calibrations, (2) adjust those measurements, and (3) apply surface reflectance.

In helping determine which deployments have incorrect factory calibrations, [*Gregg and Carder*, 1990] can be used to provide theoretical maritime irradiance from which to determine a clear-sky, climatological irradiance dataset at the mooring locations. Realistic atmospheric parameters derived from CalCOFI historical distributions are passed through [*Gregg and Carder*, 1990] model for surface irradiance in 200 iterations for each measurement closest to local noon [*Gregg and Carder*, 1990], providing clear-sky irradiance values at each wavelength at the mooring locations. These values are plotted in Figure 2.2 along with the daily maximum of irradiance at 490.1nm at CCE2 plotted versus day of the year. Irradiance values less than five standard deviations than the [*Gregg and Carder*, 1990] values are assumed due to clouds and are ignored. Using those values, deployments which have at least 50% of values outside of two standard deviations of the expected wavelengths are considered abnormal. Figure 2.2 (top left) gives surface irradiance during CCE2 at wavelength 490.1nm; deployments CCE2-02 and CCE2-03 are deemed abnormal and need to be adjusted. This adjustment is completed by comparing observed and expected ratios of irradiance.

Ratios comparing irradiance at different wavelengths are a useful tool because clouds, haze, or solar elevation affect the full irradiance spectrum in a similar manner

[*Gregg and Carder*, 1990]. Figure 2.2 compares daily maximum surface irradiances $E_d(555)$ vs $E_d(412.6)$ for CCE2, with the [*Gregg and Carder*, 1990] $E_d(555)$ vs $E_d(412.6)$ in black. CCE2-02 and CCE2-03 do not follow the expected relationship given by [Gregg and Carder, 1990], further corroborating a conceived sensor drift for $E_d(490.1)$ on these deployments. Because of its stability when compared to the [*Gregg and Carder*, 1990], $E_d(412.6)$ is considered stable in each deployment and is therefore used to adjust other wavelengths. The relationship can be determined through linear regression in the following sense, where the subscript g denotes the [*Gregg and Carder*, 1990] values, the subscript m describes measured irradiance, and P and Q are slope and intercept (respectively) derived from using linear regression;

$$\begin{aligned} E_m(412.6) &= P_m \cdot E_m(443) + Q_m \\ E_g(412.6) &= P_g \cdot E_g(443.3) + Q_g \end{aligned} \quad . \tag{2.2}$$

Adjusted irradiance (E_a) is introduced, and represents the measured irradiance after adjusting to the [*Gregg and Carder*, 1990] values. Two assumptions are made; (1) the measured irradiance at 412.6nm($E_m(412.6)$) does not need to be adjusted and (2) the [*Gregg and Carder*, 1990] relationship holds in the adjusted irradiance values (i.e. $E_m(412.6) = M_g \cdot E_a(443) + N_g$). The adjusted values of $E_a(443\text{nm})$ are derived using

$$E_a(443.3) = \frac{P_m}{P_g} \cdot E_m(443.3) + Q_m - \frac{Q_g}{P_g} \quad , \tag{2.3}$$

and are plotted in figure 2.2 (top right) and (middle right).

Finally, reflectance by the sea surface interface is applied following [*Neumann*

and Pierson, 1966]; it is assumed on a clear day, diffuse irradiance accounts for 15% of the measurement, with 6.6% reflectance, and direct irradiance accounts for 85% of the measurements with reflectance following the Fresnel Equations. [*Kirk*, 2010] shows that surface roughness does not affect the interface reflectance for a zenith angle $\theta<70^\circ$, the delineation of daytime for measurement. By the [*Neumann and Pierson*, 1966] equations, solar daytime measurement penetration ranges from 94.0% to 97.4%. [*Neumann and Pierson*, 1966] indicate these measurements have an associated 2.54% error, which accounts for errors in assuming the 15% for diffuse irradiance and 85% for direct irradiance holds during cloudy days. After these penetration estimates are applied, the surface irradiance just below the surface is found.

Though the scale factor for the instrument at depth is checked to be consistent with expected irradiance values, more work is needed to validate these numbers. The instrument at depth requires adjustments to the dark counts, which is found when the instrument is collecting dark measurements (i.e. the sun is more than 6° below the horizon, the definition of civil twilight). Measurements taken during this time show a slight shift over the course of each deployment (see figure 2.2, bottom). This signal is uncorrelated with fluorometric yield, lunar cycles, or other wavelengths, and is sometimes negative in value. It is therefore assumed to represent radiometric dark counts and are corrected via an offset found by applying a 5-day box-car filter to the data (the solid black lines in figure 2.2, bottom). The noise equivalence is what remains when the offset is removed from the nighttime measurements (i.e. black lines minus colored lines in figure 2.2, bottom); it also represents the highest degree of precision the instrument can

achieve. Any measurements less than three times the standard deviation of this noise equivalence are assumed contaminated and ignored. This noise equivalence is also be used for error propagation, which is discussed in the error section. When the filtered offset is subtracted from the daytime radiometer-returned values, the result is downwelling irradiance at depth.

Application of the Model

Following the first corrections and surface penetration adjustments, to the surface instrument, and the offset applied to the instrument at depth, average diffuse attenuation is found by the Beer-Lambert law; $k_d = \frac{-\log(E_d / E_0)}{z}$. With this value of k_d , the model is directly applied using equation 1.12, yielding 1317 days of chlorophyll measurements at CCE1 and 1245 days of measurements at CCE2.

Validation

Model validation comes in three forms: (1) direct comparison with layer-averaged chlorophyll profiles; (2) signal comparison with other proxies of surface chlorophyll; and (3) statistical comparison with historical layer-averaged chlorophyll profiles.

Direct comparisons are available when hydrographic cruises measure chlorophyll profiles at the mooring location. Quarterly CalCOFI cruises have made 12 simultaneous measurements of surface chlorophyll concentrations at CCE1 and 13 measurements at CCE2 which align with measurements at the mooring. The chlorophyll profiles are averaged over the corresponding layer for direct comparison with the model.

Figure 2.3 (top left) and (top middle) gives comparisons at both mooring sites; CCE1 has order $0.1-1.0\,\mu g/L$ and CCE2 has $1.0-10.0\,\mu g/L$. Figure 2.3 (top right) gives the comparison using logarithmic axes. These plots display the model ability to return chlorophyll over several orders of magnitude and two different layer depths. There are some outliers which may be attributed to the model or incorrectly assuming the CalCOFI measurement depicts the result from the mooring. The average distance between the sampling station and the mooring was 4km, and the 2-4 measurements of chlorophyll over the layer depth can't resolve the full integrated information. Examining both of these concerns is part of ongoing research. As with other bio-optical models, the accuracy of the model is better understood as a collection of comparisons, rather than individual direct comparisons [*Morel and Maritorena*, 2001].

The model explains 79% of the variance in linear space and 92% of the variance in logspace for the combined measurements at both moorings. The outliers may be explained by patchiness in the spatial chlorophyll field which can approximately be estimated by the hourly measurements over a single day. This variance is described the the thick (68% of measurements over that day) and thin (95% of measurements over that day) lines in figure 2.3. While hydrographic cruises are useful because they provide a much larger picture of the ecosystem (e.g. a chlorophyll profile instead of a layer average), the model is able to return measurements of much greater temporal resolution for 0-80m or 0-40m chlorophyll at these single locations.

Statistical Comparison is feasible because of the extensive historical data available with the CalCOFI program. Due to the limited sample size of direct comparison

(11 and 13 samples at CCE1 and CCE2), statistically examining the model-returned, layer-averaged chlorophyll versus historical profiles is used to provide another validation technique. By comparing cumulative distribution functions, the Kolmogorov-Smirnov (KS) test for two independent samples shows datasets which are likely sampled from the same signal [*Sheskin*, 2003]. This comparison needs to account for increasing chlorophyll concentrations [*Rykaczewski and Dunne*, 2010; *Kahru et al.*, 2012] , and a linear trend exists for historical measurements of the 0-80m layer at CCE1 and 0-40m layer at CCE2 ($r^2=0.08$ and $r^2=0.025$, respectively). If the CalCOFI historical data are detrended to the average values since the moorings have been deployed, the distributions can be more appropriately compared. Figure 2.3 (bottom) gives that comparison.

The KS test states if there is a significant difference between the cumulative frequency distributions (approximated in figure 2.3, bottom), then the data are likely sampled from different signals; if the largest difference between cumulative frequency distributions is significantly small (i.e. smaller than $D_\alpha=T_\alpha\sqrt{\frac{n+n'}{nn'}}$), the datasets are likely sampled from the same signal. By [*Sheskin*, 2003], T_α is [1.07, 1.22, 1.36, 1.63] at confidence intervals α =[0.20, 0.10, 0.05, 0.001]. The Kolmogorov-Smirnov test requires serial independence, so the chlorophyll from every 20th day is passed into this analysis; this is less frequent than the actual decorrelation scale, defined as the first zero crossing of the signal autocorrelation (typically 5-10 days, depending on season and year), but can be used to show that the signal easily passes the KS test at all confidence

intervals, consistent with the hypothesis that CalCOFI profile averages and the model-returned chlorophyll are likely taken from the same signal.

An Error Analysis for the model considers each module individually, and follows the error analysis of [*Wilson et al.*, 2016]. Each module has an associated error, and for a single measurement, 20 Monte Carlo simulations are run passing this error through the model. All of measurements over a single day are collected to return a single chlorophyll estimate. Estimations of the 68% and 95% distributions are described by the thick and thin lines in figure 2.3, respectively.

ADCP

The Teledyne Long Ranger ADCP is located 1 meter below the surface and provides binned current information every 10 meters, starting at 7 meters and continuing to a depth deeper than the analysis presented here. The currents are assumed constant between 7 meters and the surface [*Dever et al.*, 2006], and the profile is interpolated to 1 meter intervals to the depth of interest. This profile is then averaged to the depth of interest (80m at CCE1 and 40m at CCE2). The result is a layer average matching the chlorophyll layer measured by the model at each mooring. All of the measurements collected over a 24-hour period of time (local midnight to local midnight) are averaged to return a daily, 0-80m or 0-40m current vector for CCE1 or CCE2, respectively.

The current vector is represented as North/South and East/West, but the quantities of interest are cross-shore and alongshore. The CalCOFI grid provides a frame of alongshore and cross-shore, and the moorings are located on line 80. The reference frame of the currents is provided in the standard east-west/north-south frame, but is rotated 37.6

degrees counter-clockwise to match the CalCOFI grid. U describes across-shore and V representing alongshore in this new frame. In this frame, CCE1 is considered directly offshore of CCE2.

Temperature

Temperature sensors on the mooring are deployed over the 0-80m at CCE1 or 0-40m at CCE2 layers. The moorings are equipped with Seabird MicroCATs and SeaCATs giving CTD information at 1-hour intervals. At CCE1, the depths are approximately [1, 10, 21, 31, 41, 61, 76, 150]m, though the 1m instrument is susceptible to biofouling and failure; if both the 1m instrument and 10 m instrument have failed, the entire profile is ignored. At CCE2, the depths are approximately [1, 7, 15, 25, 41] m. As in the ADCP data, temperature is assumed constant above from the first readable measurement (either 1 or 10m), and linearly interpolated between measurements. This profile is averaged over the depth of interest, to produce an average temperature of the layer matching model-returned chlorophyll. As in the ADCP measurements, all measurements taken over a single day are averaged for each daily measurement.

AVISO

The AVISO sea surface height (SSH) product is used to provide context for the measurements at CCE1. The altimeter products were produced by Ssalto/Duacs and distributed by Aviso, with support from CNES (**http://www.aviso.altimetry.fr/duacs/**). The multisatellite altimetry is presented here.

Advective Transport

The focus of this work is to analyze the chlorophyll transport by computing the

product of daily chlorophyll (C) and the simultaneous current measurements (U or V , depending on orientation). The product of these time series provide chlorophyll flux (*UC*). The chlorophyll flux is shown in figures 2.4 and 2.5 at CCE1 and CCE2, respectively. The measurement technique for chlorophyll assumes an average chlorophyll concentration for the layer of interest, and for consistency, the average value for the surface layer currents is also used. The product of these layer averages is assumed to represent the horizontal transport of chlorophyll, despite both chlorophyll and currents having a vertical structure. This assumption is tested by calculating the transport associated with realistic chlorophyll profiles (using CalCOFI) and current profiles (using the mooring) using both methods. The profile method averages the dot-product of the vertical profiles, and then averages the result. The mean method averages both profiles, and multiplies this average. These results are easy to compare, and have r^2 values of (0.995, 0.989) and (0.995, 0.994) for (*UC*, *VC*) at CCE1 and CCE2, respectively. This quick analysis provides a simple estimate of error associated with assuming constant layers. Ultimately, this does not change the result of the study conducted here.

Methods

The methods begin with spectral analysis techniques applied to the individual time series of chlorophyll and temperature (referred to as tracers), and cross-shore and along-shore flow (referred to as currents). There are five unbroken chlorophyll time series longer than 100 days which are analyzed at CCE1 and three at CCE2; they are boxed in the time series of chlorophyll flux in figures 2.4 and 2.5. At CCE1, the dates are (2011-Mar-06 to 2011-Oct-19), (2012-Sep-21 to 2012-Dec-30), (2013-Jan-02 to 2013-Apr-12),

(2013-Oct-01 to 2014-Oct-24), and (2014-Oct-26 to 2015-Oct-22). At CCE2, the dates are (2011-Jul-22 to 2011-Nov-09), (2013-Nov-27 to 2014-May-01), and (2014-Jun-26 to 2015-Apr-27). The Power Spectral Density is estimated using the Welch method [*Welch*, 1967], with Hamming Windows of length 100 days, and maximum 50-day overlap. These spectra are plotted as the individual PSD in figure 2.6; in order to obtain an average spectrum, the PSD are interpolated at 90 frequencies between 1/(100 days) and 1/(2 days). The interpolated spectra for each variable are then averaged to obtain the black-outlined spectra in figure 2.6, top row. The second row of plots in figure 2.6 give the Variance Preserving Spectra (VPS), as defined by [*Thomson and Emery*, 2001], normalized to the maximum value for that spectra. The VPS show the frequencies contain variance of the time series. These plots are discussed in the next section.

Advective transport of a tracer is the current velocity (U) multiplied times the concentration (C). The most immediate result from this work is to arrive at a time series for chlorophyll transport in the CCS for both cross- and along-shore advection (figures 2.4 and 2.5, bottom plot).

Through Reynolds' Decomposition, the currents and chlorophyll variables can be broken into mean ($\overline{\ }$) and eddy terms ($'$). This equation can be averaged in time (denoted by the $\langle\rangle$) in the following manner;

$$\begin{aligned} UC &= (\langle U\rangle + U')(\langle C\rangle + C') \\ UC &= \langle U\rangle\langle C\rangle + \langle U\rangle C' + U'\langle C\rangle + U'C' \\ \langle UC\rangle &= \langle U\rangle\langle C\rangle + \langle U\rangle\langle C'\rangle + \langle U'\rangle\langle C\rangle + \langle U'C'\rangle \\ \langle UC\rangle &= \langle U\rangle\langle C\rangle + \langle U'C'\rangle . \end{aligned} \tag{2.4}$$

Both the mean term ($\langle U\rangle\langle C\rangle$) and eddy term ($\langle U'C'\rangle$) are given as cross-shore

quantities; the same calculation can be applied to alongshore current vector, $V = \langle V \rangle + V'$. The eddy term quantifies how currents may transport low chlorophyll in one direction and high chlorophyll in another direction. The full results for CCE1 and CCE2 are given in table 2.1.

The cumulative-integrated time series for $U'C'$ is now examined more closely in order to understand the dynamics of the region. At both moorings, events are analyzed for their contribution to the eddy advection of the chlorophyll signal. A series of figures (2.7 through 2.13) are shown that have a time series for temperature, chlorophyll, and cross-shore currents during interesting events which occur at the mooring. The cumulative current transport is calculated through trapezoidal integration in time, beginning at the start of the selected time interval; the bottom left plot in each figure 2.7 through 2.13 gives this integral in time and represents the cumulative chlorophyll advection. There are slight differences in analysis between both mooring locations, based on the goals of the analysis for that mooring. In each, the chlorophyll, currents, and chlorophyll transport are discussed in detail, while temperature is discussed only in two examples; temperature is included in all figures where it's available for consistency.

A goal at CCE1 is to discuss the ability of low-frequency measurements to estimate the chlorophyll transport, so an additional breakdown for the transport terms is required. Specifically, the transport is broken into low- and high- frequency terms; $U'C' = (U'_h + U'_l)(C'_h + C'_l)$. If the time series is long enough, once the time series is time-averaged, the low and high frequency component represent the eddy advection of chlorophyll; specifically, $\langle U'C' \rangle = \langle U'_h C'_h \rangle + \langle U'_l C'_l \rangle$. This is demonstrated by the

low frequency signal less than 1/(25 days) representing 97% of the cumulative eddy advection of chlorophyll.

An equiripple, lowpass filter with cutoff frequency 1/(25 days) is applied to the CCE1 time series of temperature, chlorophyll, and currents, highlighting longer events and suppressing shorter events. The cumulative sum of eddy advective transport is plotted in the fourth plot for each figure, and AVISO sea surface height is plotted for three separate days, providing synoptic context for the system. In the results section, these plots are interpreted as showing that low-frequency terms associated with the California Current dominate the chlorophyll transport.

The goal for the analysis at CCE2 is to understand chlorophyll transport associated with a few individual events. At this location, the filter is a useful for discussing dominant features, but is not used to calculate a cumulative transport as it was for CCE1. Before the filter is applied, two periods of 5 days are interpolated to create an unbroken time series; during these periods, the light reaching the instrument at depth was below the noise equivalence for at least 3 wavelengths, so the data were ignored. No other data presented here feature interpolated data. An equiripple, lowpass filter with cutoff frequency 1/(10 days) is applied to the CCE2 time series of temperature, chlorophyll (with interpolated periods), and currents, and plotted in their respective plots for each event. The cumulative chlorophyll transport is calculated from the time series without the two 5-day interpolation. AVISO is not included in the analysis of the near shore, so those plots are not included in tandem with the time series as they are at CCE1.

As a final discussion point, the advective transport of chlorophyll is compared to

previously measured and estimated carbon transport estimates. The standard conversion factors between mg of chlorophyll and mg of Carbon are taken from [*Landry et al.*, 2009].

Results

The various chlorophyll transports are given in table 2.1; as described, transport values are rotated to align with the CalCOFI grid (cross-shore and alongshore). The California Current Jet (CCjet) has been estimated at the CCE1 site using drifter and satellite records [*Matthews and Emery*, 2009], and the mean currents at the CCE1 follow the historical CCjet record, with onshore/southward flow; chlorophyll is low in this region. The mean chlorophyll transport term is onshore/southward; however, the eddy terms are primarily offshore, with very low alongshore eddy transport of chlorophyll. A recirculation current follows the Santa Barbara coastline westward, and dominates the mean CCE2 current [*Matthews and Emery*, 2009]. This causes high northward/alongshore flow, and moderate offshore flow at CCE1. With high chlorophyll, this translates to large northward/alongshore transport in the mean current and offshore transport shared between mean and eddy terms. The mean terms are relatively well understood; the mean current velocities in the region follow the pattern described by [*Matthews and Emery*, 2009] and the mean chlorophyll follows patterns described by [*Kahru et al.*, 2012].

Power Spectral Density

Figure 2.6 gives the power spectral density (PSD) and the variance-preserving spectra (VPS) for currents and tracers (temperature and chlorophyll). The PSD has been

used to connect time series measurements with theories, and can offer insight here. The VPS can quickly provide insight into where the variance is, and is used to contextualize the choice of cutoffs for the filters used previously.

The PSD of current vectors at CCE1 approximately follow the previously described f^{-2} slope for the high frequency measurements at 35 degrees North [*Scharffenberg and Stammer*, 2011]. This extends to temperature measurements, but chlorophyll has a whiter spectrum at higher frequencies. This follows [*Powell and Okubo*, 1994], who modeled 2D turbulence of reactive and non-reactive tracers in the spatial domain and suggests more chlorophyll variance at smaller scales, though it may not be appropriate to cite a specific theory for the patchiness [*Franks*, 2005]. It is clear the patchiness of chlorophyll is evident in the time series at the mooring, which has more variability than temperature starting at approximately 1/(40 days). The peak of the VPS of the chlorophyll tracer shows increased variance for frequencies higher than approximately 1/(25 days), and the ability for frequencies lower than 1/(25 days) to represent cumulative chlorophyll transport is examined in individual cases later.

CCE2 has approximately a white spectrum for cross-shelf and along-shore currents. This region features upwelling occurring on 10-30 day events [*Rykaczewski and Checkley*, 2008; *Checkley Jr. and Barth*, 2009], which adds energy to the system on these timescales. Cross-shelf currents have a peak at approximately 13 days, and along shore currents have a peak at approximately 20 days, implying that energy may be entering the system. Temperature has a moderate peak in spectral energy which approximately matches the 20-day timescale, however chlorophyll does not have such a feature. This

may be because consecutive upwelling events can be featured as one large bloom; an event in 2012 discussed below describes exactly this. Chlorophyll does generally match the spectral slope of temperature until ~13 days, before exhibiting the large variance and flat spectral slope at high frequencies.

Events at CCE1

Four events are shown to discuss eddy advection of chlorophyll at CCE1. These are given in figures 2.7-2.10. The primary goal of this analysis is to show the CCjet as the dominant CCE2 transport mechanism, and the secondary goal is to demonstrate that low-frequency signals can govern the chlorophyll transport at CCE1.

Figure 2.7 shows an example during CCE1-07, in early 2014, where high chlorophyll is transported offshore. SSH and cross-shore currents show a quiescent current field near the mooring on 8-Feb-2014. A current develops which is visible in the ADCP, follows lines of constant SSH in the AVISO plots, and matches the signature of an arm of the California Current [*Matthews and Emery*, 2009]. It is generally offshore and is sustained until approximately 25-May-2014. During the time where currents are directed offshore (negative eddy term), chlorophyll is higher than the time series average (positive eddy term), which causes a negative transport of chlorophyll across the shelf (i.e. high chlorophyll offshore). When the cross-shore currents eventually slow, the chlorophyll drops to the time series average which halts the cumulative transport of chlorophyll offshore.

Figure 2.8 shows low chlorophyll being transported offshore from May to August, 2011. The current velocity initially has a zero cross-shelf component on 2011-May-15

and chlorophyll matches the mean value. Onshore currents develop through 2012-July-25, visible in both the ADCP and AVISO field. Simultaneously, chlorophyll begins to drop from the mean. The eddy transport of chlorophyll is the product of fluctuations from the mean; because chlorophyll concentration is below the average, the eddy transport of chlorophyll is negative (i.e. offshore). In the cumulative transport of chlorophyll, it is clear the product of low frequency terms dominates with an offshore transport of chlorophyll.

Figure 2.9 highlights a period that matches the onset of a hydrological phenomenon known as the warm blob [*Bond et al.*, 2015; *Zaba and Rudnick*, 2016]. Over a period less than one month, the temperature at the mooring rises 3 degrees while the AVISO displays a transition of the CCjet moving from offshore of the mooring to onshore of the mooring. This transition is represented by the 2014-July-6 AVISO plot, and includes a high chlorophyll event and strong offshore currents. Following this, there is a period of low chlorophyll, stagnant currents, and warm temperatures, all features associated with the warm blob [*Bond et al.*, 2015; *Zaba and Rudnick*, 2016]. While this transition of the CCjet past the mooring featured strong currents and high chlorophyll, it was very short, and therefore had small advective transport of chlorophyll. The low frequency terms missed $12\,g/m^2$ during this 20- day transition.

Figure 2.10 highlights the large positive cross-shelf eddy advective event, transporting low chlorophyll offshore in December, 2012. From the AVISO plots, it appears to be the result of either a warm core eddy or arm of the California Current which was low in chlorophyll. While the currents remain in January, 2013, the chlorophyll

begins to rise, transporting high chlorophyll offshore. The result is no net eddy chlorophyll advection.

Events at CCE2

The analysis at CCE2 focuses on upwelling events, using estimated upwelling dates from biogeochemical signals on the mooring (Hey-Jin Kim, personal communication). While the filters are useful in discussing events, it is not used to describe the dominant transport. Examining several transport events aid in understanding the dominant features in transporting chlorophyll past the mooring, in particular linking the event-scales matching upwelling with the transport of chlorophyll. The first example examines a single upwelling event in 2011, while the second considers consecutive upwelling events in 2012. Finally, the third discusses the signature of the recent "warm blob" [*Zaba and Rudnick*, 2016] in the context of chlorophyll transport.

Upwelling events cause chlorophyll to rise and currents flow offshore [*Checkley Jr. and Barth*, 2009]. An example can be seen in figure 2.11, an upwelling event on 25-June-2011 (Hey-Jin Kim, personal communication). This upwelling event exhibits large offshore currents (18-June to 1-July) and elevated chlorophyll (beginning July 3). Notice the offshore current halts before the elevated chlorophyll begins. This event does not contribute to the cumulative eddy advective transport of chlorophyll. The 5-day gap in chlorophyll measurement is during a period of low onshore currents, so would not contradict the concept that offshore transport of chlorophyll is low during this event.

Figure 2.12 shows the upwelling season for 2012. There are several consecutive upwelling events in this season (Hey-Jin Kim, personal communication), specifically

centered on 27-Apr, 24-May, and 8-June. Each of these exhibit offshore transport and a chlorophyll signature. For example, the first upwelling event has offshore flow from 25-Apr to 3-May and a bloom starting on 2-May. If the transport were limited to that single day overlap, the cumulative contribution would be similar to June-2011. However, a second upwelling event began while the chlorophyll levels were still elevated, transporting chlorophyll from the first bloom offshore. This process is repeated a second time, with a new upwelling signature in the currents on 8-June, which transports the chlorophyll from the previous upwelling event offshore. The 5-day gap during this time is associated with offshore currents, and would probably result in more chlorophyll being transported offshore (i.e. not contradicting the concept presented here). Where before a single upwelling event transported very little chlorophyll, the combined transport of consecutive upwelling events has transported more than 500 g/m2 chlorophyll offshore over 2 months.

Finally, figure 2.13 describes the onset of during the hydrological warm blob during the summer of 2014 [*Zaba and Rudnick*, 2016]. During this time, temperature is comparatively high, the chlorophyll varied in the low to medium values while currents oscillated onshore and offshore. These oscillations are not associated with upwelling events (Hey-Jin Kim, personal communication), and the chlorophyll does not experience extreme values as it does during the upwelling events cited in 2011 and 2012. Still, the alignment of currents and chlorophyll oscillations during this time transports low chlorophyll onshore and high chlorophyll offshore.

Discussion

The work here estimates the transport chlorophyll past two moorings. The sampling frequency and length of deployment of multiple measurements allow for an improved understanding of chlorophyll advection, both in the mean and eddy advection. Future work should examine the gradient field in the region, and potentially estimate diffusivity.

One interesting feature in this study is the mean onshore transport of chlorophyll at CCE1, and though it has been seen in previous studies [*Landry et al.*, 2009]. The offshore transport occurs through events, including frontal features, upwelling filaments, mesoscale eddies, and meanders of the California Current system. It is therefore important to understand mean and eddy terms in the transport of chlorophyll, which are analyzed here.

The CCE1 eddy advection of chlorophyll is controlled by the CCJet. Low chlorophyll is advected onshore (figure 2.8), high chlorophyll is advected offshore (figure 2.7). In the events presented here, the low-frequency term has described 97% of the cumulative transport, matching all significant events except the onset of the warm blob in July-2014. Future work should focus on matching the AVISO geostrophic currents and satellite-returned chlorophyll concentrations with values returned from the mooring. Both of these products are able to return signals with a resolution of at least 25 days [*Matthews and Emery*, 2009; *Kahru et al.*, 2012]. If applying the advective transport analysis to the satellite products agrees with the results presented here for the appropriate satellite pixel, the technique can be applied to satellite pixels other than the location of CCE1. For

example, if a line of pixels is drawn parallel to shore, the transport through that line should estimate the total chlorophyll transport to the offshore.

The CCE2 eddy advective chlorophyll transport is characterized by upwelling events. A typical upwelling event [*Checkley Jr. and Barth*, 2009] is characterized by offshore flow and high chlorophyll. However, the time series of these two variables may not perfectly align to achieve offshore transport, as in 2011 and figure 2.11. Instead, consecutive upwelling events transport chlorophyll to the offshore (as in figure 2.12). When an upwelling event occurs before the previous upwelling-induced bloom has dispersed, chlorophyll is transported offshore. This has been specifically shown with three consecutive upwelling events in 2012. This shows the importance of upwelling seasonality in transporting chlorophyll, and the co-spectra between currents and chlorophyll could be used to describe the relationship quantitatively.

Upwelling Filament

Point Conception separates the large upwelling region of Central California from the recirculation featured in the Southern California Bight [*Winant and Dorman*, 1997; *Checkley Jr. and Barth*, 2009]. Where these features meet, they form a semi-permanent meander in the California Current, continuing southward while the coast turns eastward at Point Conception [*Centurioni et al.*, 2008; *Checkley Jr. and Barth*, 2009]. They feature cold water, high currents, and high chlorophyll, and are considered a large cross-shelf transport mechanism for plankton and carbon [*Keister et al.*, 2009]. Current and future studies are investigating these mechanisms for carbon transport and subduction,

Filaments are best characterized using hydrographic profiles, but two features at

CCE1 stand out as mechanisms that transport chlorophyll offshore (figures 8 and 10). Where other examples feature transporting low chlorophyll towards the coast (figures 7 and 9), these two events are actually the primary two events that transport high chlorophyll offshore, and figure 2.15 gives satellite chlorophyll during those two events. A filament-like structure is visible in the chlorophyll signal.

The event in 2014 transported an estimated $80\,m * 120\,g\langle chl\rangle / m^2 = 9.6\,kg\langle chl\rangle / m$ during those 4 months. Those units are kg of chlorophyll per meter of coastline. The event in 2013 transported $36\,kg\langle chl\rangle / m$ over 2 months.

Simple Box Model and Literature Comparison

Previous in situ measurements have been conducted using floats and hydrographic measurements; a particularly useful comparison with [*Landry et al.*, 2009] provides potential for a simple box model. Despite the [*Landry et al.*, 2009] goal of measuring vertical fluxes and chlorophyll growth terms, the work allows for a basic calculation of chlorophyll advection;

$$UC = \langle chl\rangle \frac{D}{T}, \quad . \tag{2.5}$$

where UC is the cross-shelf transport of chlorophyll. The $\langle chl\rangle$ is the surface-averaged chlorophyll concentration calculated from figure 2 in [*Landry et al.*, 2009] as [4, 3.5, .83, .25, .40, 1.30, .80, .32] mg/m^3 at [13.5, 40, 98, 163.5, 382.5, 46.5, 61.5, 281]km. T is the time from column 2 in table 2 in [*Landry et al.*, 2009], given as [4, 5, 5, 5, 5, 5, 6, 4,]. D is the distance traveled relative to shore, given in figure 5 in [*Landry et al.*, 2009] as . This estimates the horizontal displacement of chlorophyll

concentration, and the results are given in figure 2.14. Also plotted in figure 2.14 is the average UC measured from both CCE moorings. The results for both measurement platforms in figure 2.14 compare favorably in magnitude.

A final analysis compares an aspect of the results here with vertical carbon transport calculated by [*Stukel et al.*, 2011]. A box is constructed with the CCE moorings as the inshore and offshore sides. The alongshore transport is assumed negligible or to be equivalent (i.e. ignored). Chlorophyll which enters through the sides of the box (i.e. passes the moorings) passes through the other side or is grazed by zooplankton and sink to depth as fecal pellets of particulate carbon [*Stukel et al.*, 2011]. It is assumed the 80m layer at CCE1 and 40m layer at CCE2 represents the surface chlorophyll at the mooring, and the results in tabel 2.1 represent the chlorophyll transport past the moorings. The flux through the CCE1 mooring is $0.98\,g/(m^2 day)*80\mathrm{m}=78.40\,g/(m\,day)$ onshore and the flux through the CCE2 mooring is $7.27\,g/(m^2 day)*40\mathrm{m}=290.8\,g/(m\,day)$ offshore. Because the transport past each mooring is towards the other mooring, the chlorophyll is assumed to either be grazed away or sink out of the system. The distance separating the moorings is approximately 200km, so the net sink of chlorophyll over this box is $-0.0018\,g\,Chl/m^2 day$, representing the sum of chlorophyll growth, grazing, and sinking in the region between the two moorings. If this is converted to carbon, using a (50 mg C)/(mg Chl) relationship [*Landry et al.*, 2009; *Stukel et al.*, 2011], the region between the moorings sinks $-0.0923\mathrm{gC}/(m^2 day)$.

This can be compared directly to results from [*Stukel et al.*, 2011]. Table 1 in [*Stukel et al.*, 2011] provides vertical Carbon Export estimates of [0.076, 0.072, 0.151,

0.094] $gC/(m^2 day)$ at distances from shore of [50, 100, 180, and 360]km, respectively, estimated from figure 6 of the [*Stukel et al.*, 2011]. A trapezoidal average is applied for these values to obtain the average particulate sinking over this region; the region sinks $-0.1006\,gC/(m^2 day)$ in this region, within 10% of the estimates found from the box model using the moorings. There are many reasons for this result to be a coincidence, though the concept of estimating carbon export through carbon transport at the boundaries of a box should prompt future studies.

This type of analysis could be a very beneficial use of the time series. While only the full time series average is used here, if an understanding of relevant timescales connecting the transport from one mooring to another is gained, then perhaps seasonal or interannual vertical carbon flux estimates could be understood. More work would be required in estimating along-shore carbon transport. For example, did the warm blob increase or decrease vertical carbon flux? Do El Nino or La Nina conditions enhance vertical carbon fluxes? Is the vertical carbon flux changing?

Conclusion

A new chlorophyll retrieval [*Wilson et al.*, 2016] is applied to mooring measurements in the California Current System. A new dataset of bulk, 80m- or 40m-averaged chlorophyll provides several new analysis opportunities. High frequency terms have a large influence on the chlorophyll value at a given time, but ultimately only move chlorophyll back and forth, and do not transport coastal chlorophyll to the deep ocean. At the offshore location, cross-shelf eddy transport of chlorophyll totals 31.20 $g/(mday)$ offshore and is primarily described by the low-frequency events. In the near-shore

location, cross-shore eddy transport is estimated at 94.80 $g/(m\,day)$. Consecutive upwelling events were shown to contribute significantly to this transport, while during single upwelling events, the offshore currents halt before the chlorophyll begins to grow.

Using basic Carbon/Chlorophyll relationship, $392.0\,g\,C/(m\,day)$ are transported onshore at CCE1 and 1454.0 $gC/(m\,day)$ are transported offshore at CCE2. The growth, transport, and sinking of organic material in the California Current System continues to be of interest, and these tools and results can help in this regard.

Chapter 2, in part, is currently being prepared for submission for publication. Co-authors include Send, Uwe; B. G. Mitchell. The dissertation author was the primary investigator of this material. The data were collected from the California Current Ecosystem Mooring, and this research would not be possible without the Mooring Lab at Scripps Institution of Oceanography. The CCE moorings and some of this analysis work were supported by the NOAA Office of Climate Observation. The National Science Foundation, Graduate Research Fellowship also funded much of this analysis work.

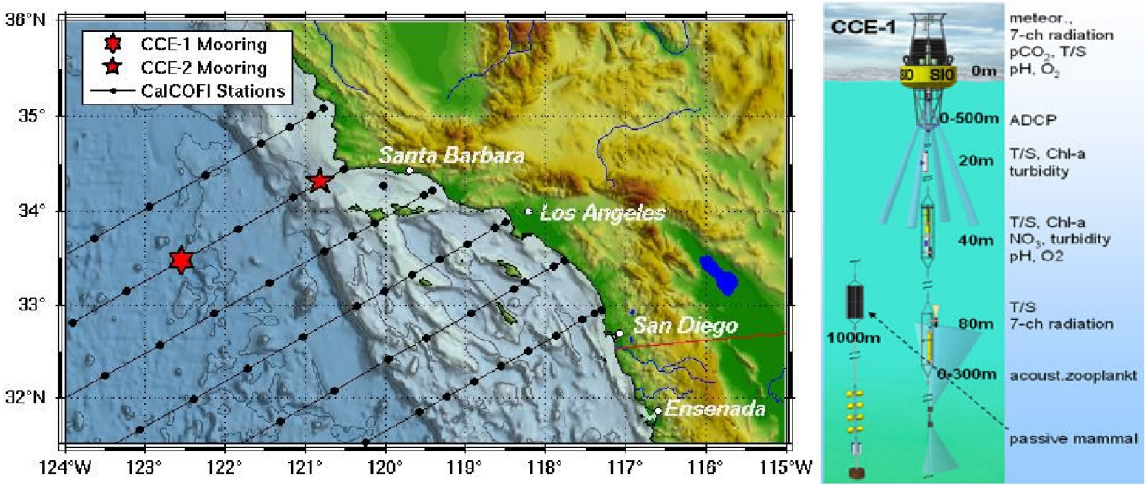

Figure 2.1: The California Current Ecosystem (CCE) moorings are located along CalCOFI's Line 80 near Point Conception, shown here as red stars; CCE1 is offshore and CCE2 is near shore. The diagram provide s representative schematic for the types of measurements made at the mooring; the instruments used in this analysis are the two 7-ch radiation radiometers and the ADCP providing solar irradiance and current velocity, respectively.

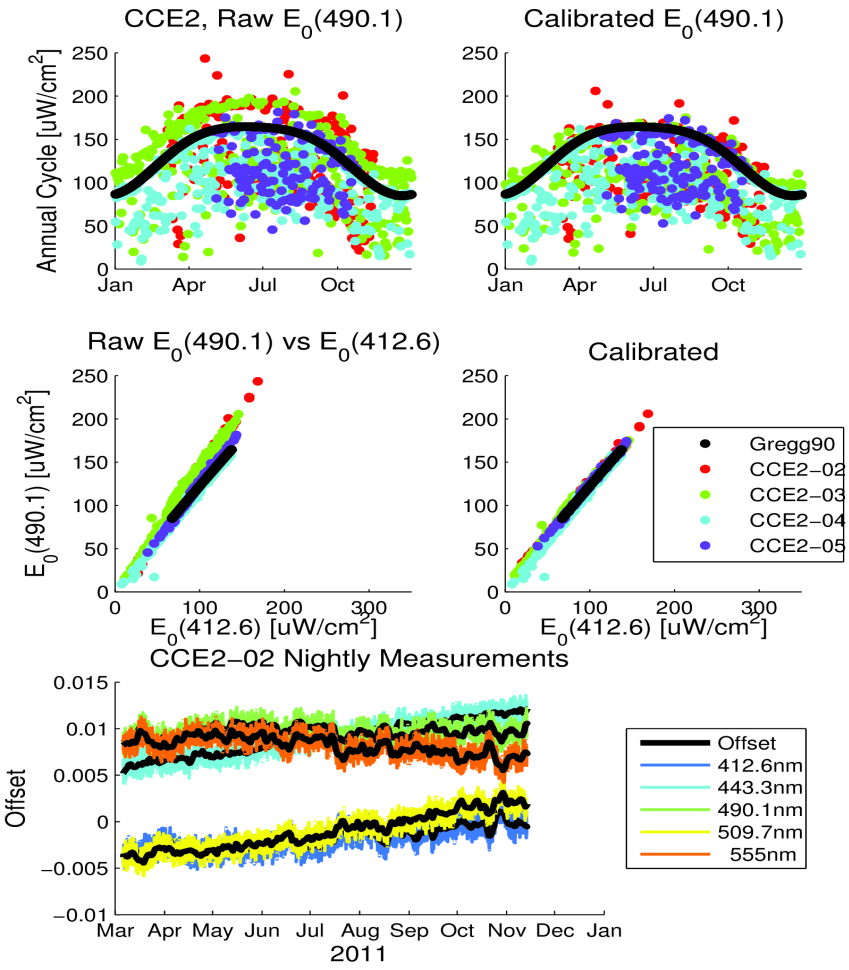

Figure 2.2: The top row gives the annual cycle of irradiance for 490.1nm using *[Gregg and Carder, 1990]* in black and individual deployments in various colors (given in legend), both before (top left) and after (top right) the calibration described by equation 2.3 has been applied to CCE2-02 and CCE2-03. The middle row compares the irradiance at 490.1nm and irradiance at 412.6, both before (middle left) and after (middle right) calibrating irradiance at 490.1 using irradiance at 412.6 by equation 2.3. The bottom figure gives the irradiance at depth when the sun is greater than 6 degrees below the horizon and light is assumed to be absent; the colored lines represent specific wavelengths and black lines represent the data with a 4 day box filter applied. These black lines are used as dark counts for the instrument while the difference between the black lines and colored lines are used as noise equivalence.

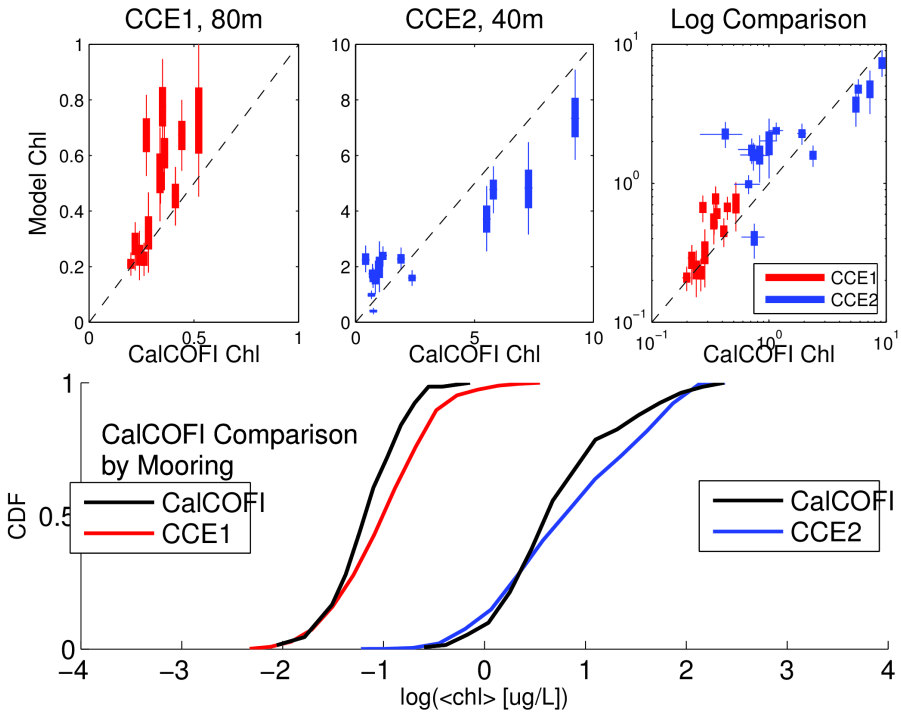

Figure 2.3: Direction comparison of chlorophyll returned from the model versus CalCOFI measured chlorophyll for CCE1 (top left) and CCE2 (top middle). Top right is the logarithmic comparison, displaying agreement over several orders of magnitude. The thick lines represent the model's 68% distribution and thin lines represent the model's 95% distribution. The bottom figure plots the cumulative distribution for the natural log of chlorophyll values taken from CalCOFI (black lines) and each deployment (colors); the lower values correspond to CCE1 and higher values correspond to CCE2, with the appropriate CalCOFI comparison

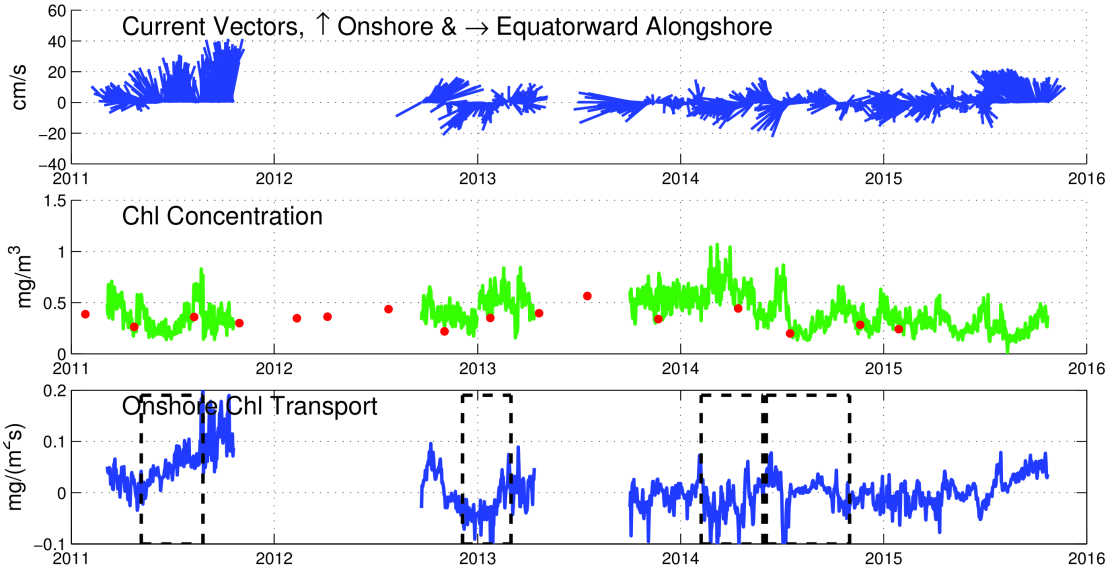

Figure 2.4: CCE1 current, chlorophyll, and chlorophyll flux timeseries. The top gives the daily current vectors, rotated to align with the CalCOFI grid; positive y-axis is towards the shore and positive x-axis is alongshore, towards the equator. The length of the vector corresponds to the current speed, with the y-axis as a reference. The middle time series gives the chlorophyll concentration measured from the model (green) and the CalCOFI bottle values (red dots). The bottom time series is the dot-product of cross-shore currents with chlorophyll concentration, giving the cross-shore transport of chlorophyll concentration. The dashed boxes highlight the sections of time presented in figures 2.7-2.7-2.10. All three panels correspond to average values for the 80m surface layer.

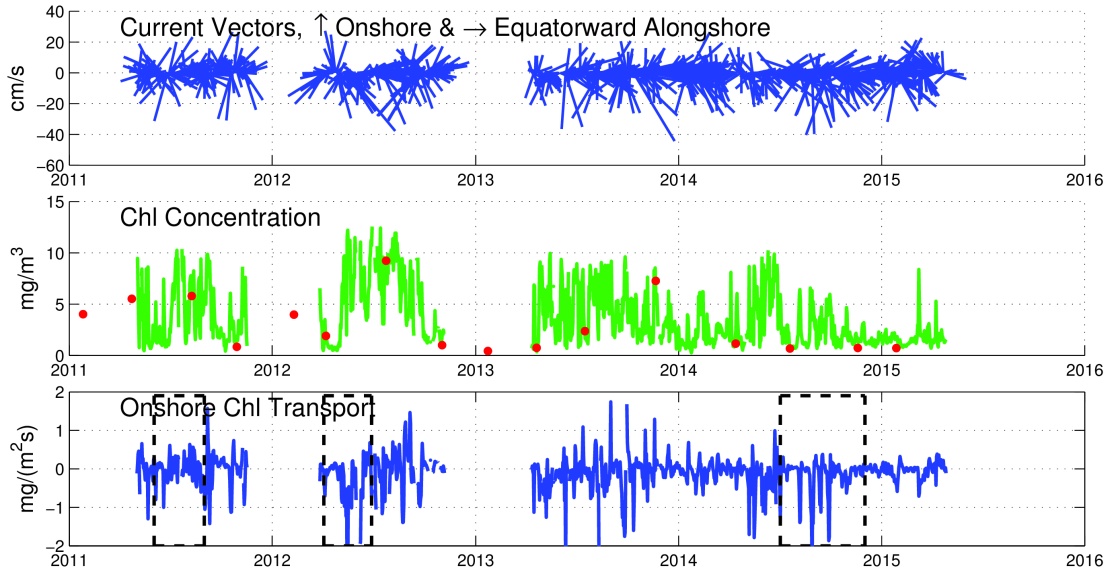

Figure 2.5: Same as figure 4, but for CCE2. These dashed boxes highlight sections presented in figure 2.11 to 2.13. All three panels correspond to average values for the 0-40m surface layer.

Table 2.1: Average values for the listed time series. <U> and <V> are average current velocities for cross-shore and alongshore, respectively. <C> is the average chlorophyll concentration measured from the mooring. <UC> is the average chlorophyll transport measured, and $\langle \overline{U}\,\overline{C} \rangle$ and <U'C'> are the mean and eddy advective terms. <VC> is the alongshore transport of chlorophyll, with similar notation for mean and advective terms..

	$\langle U \rangle$ [cm/s]	$\langle V \rangle$ [cm/s]	$\langle C \rangle$ [mg/m^3]	$\langle UC \rangle$ $\langle \overline{U}\,\overline{C} \rangle$ $\langle U'C' \rangle$ [g/(m^2day)]	$\langle VC \rangle$ $\langle \overline{V}\,\overline{C} \rangle$ $\langle V'C' \rangle$ [g/(m^2day)]
CCE1	3.93	-4.39	0.40	0.98 1.37 -0.39	-1.48 -1.53 0.05
CCE2	-1.71	5.01	3.30	-7.27 -4.89 -2.37	16.05 14.30 1.75

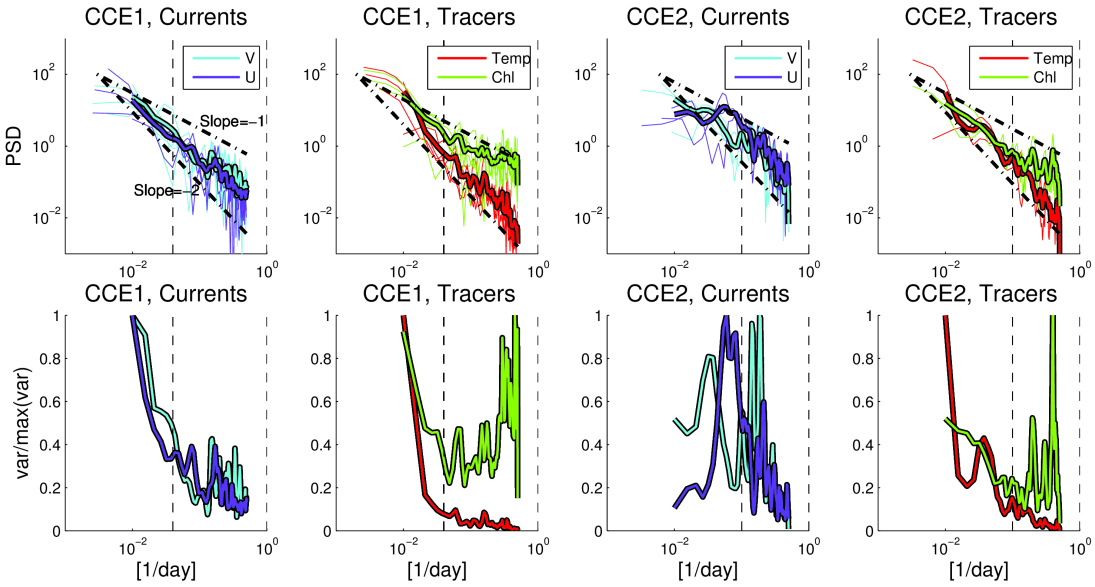

Figure 2.6: (Top row) Power spectral density for (from left to right) CCE1 currents (U-cross shore, V-alongshore), CCE1 tracers (temperature and chlorophyll), CCE2 currents, and CCE2 tracers Faintly colored are PSD of the 4 unbroken time series; outlined in black is the average of those three. (Bottom row) Normalized, variance preserving spectra of the same variables as top row. Vertical dashed lines are the frequency demarcations used as cutoffs for the filters applied to those time series: 1/(25 days) for CCE1 and 1/(15 days) for CCE2.

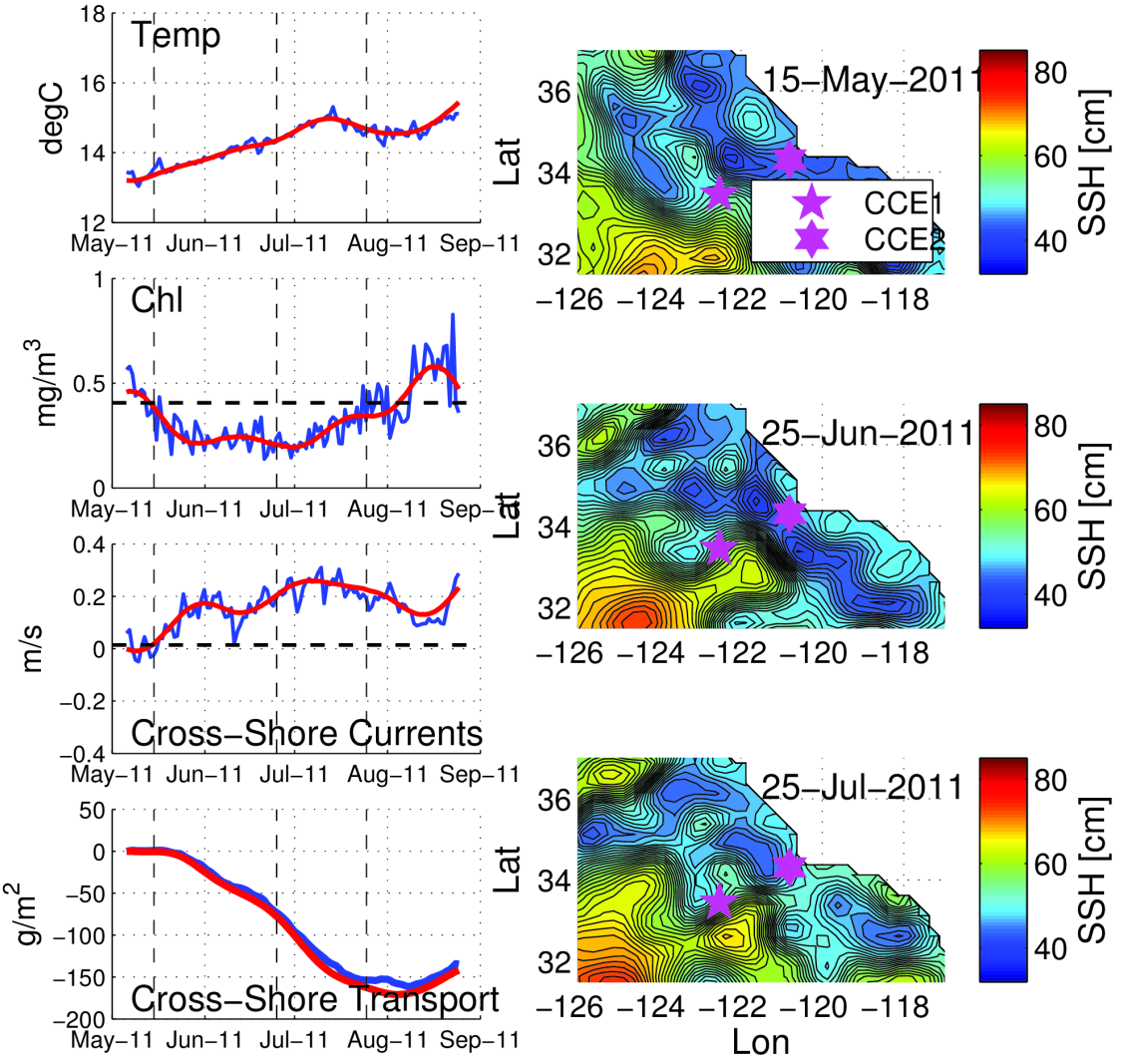

Figure 2.7: CCE1 time series (blue) of temperature, chlorophyll, and cross-shore currents for May to Aug, 2011. Red is the same time series with a lowpass filter corresponding to 1/(25 days).The bottom is the cumulative transport for the U'C' (blue) and low-pass filtered U'C' (red). The vertical dashed lines correspond to the dates on which the synoptic AVISO fields are given; these dates are chosen to correspond with interesting features. Horizontal dashed lines in currents and chlorophyll are the mean for the respective time series, giving rise to the mean ( ) and eddy (′) terms in equation 2.4. Combined, these plots provide an understanding of a period of elevated chlorophyll and offshore currents, causing offshore transport of chlorophyll.

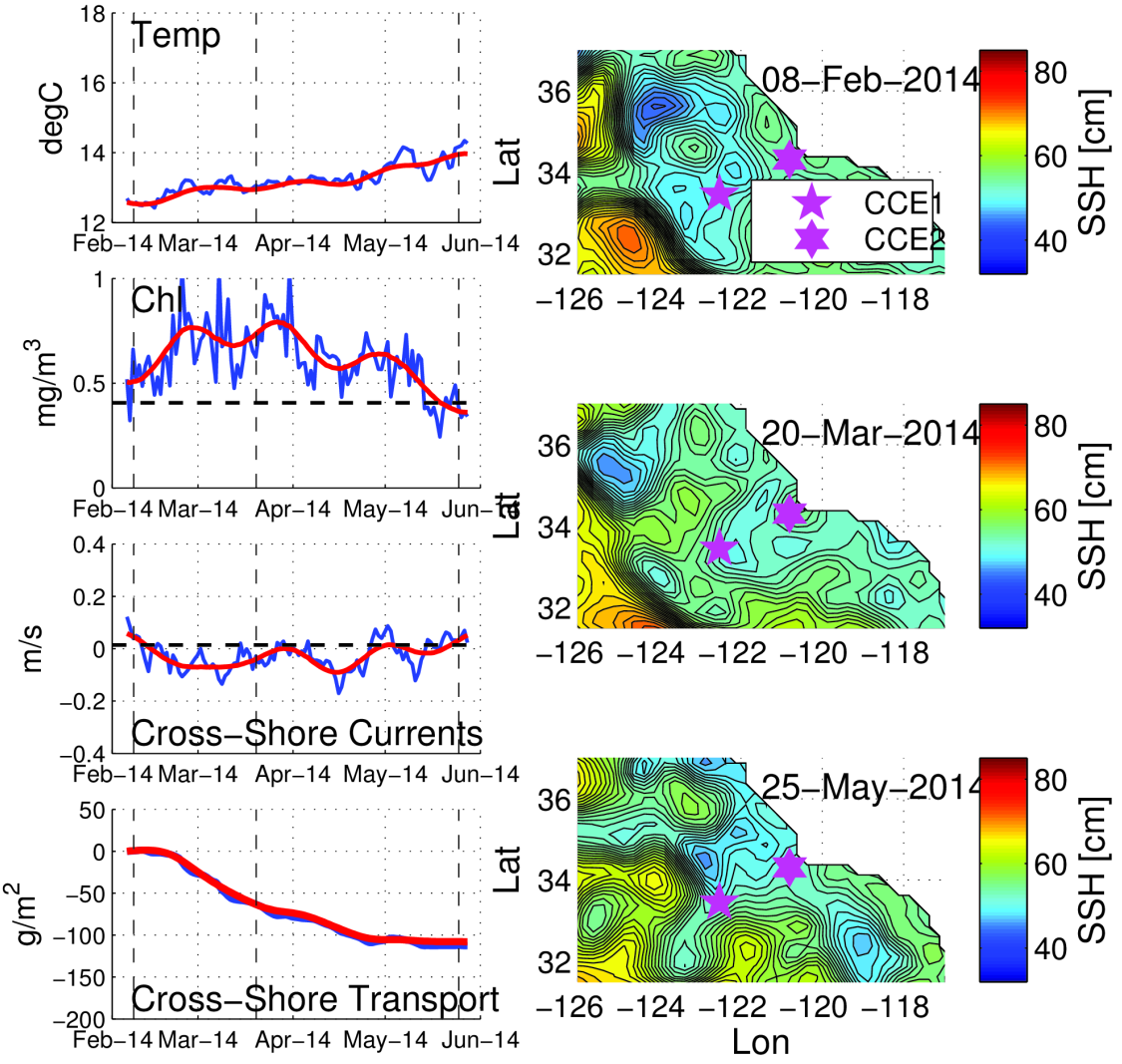

Figure 2.8: Same as previous, but for CCE1, Feb to June, 2014. Combined, these plots show low chlorophyll and onshore currents, causing offshore eddy advection of chlorophyll.

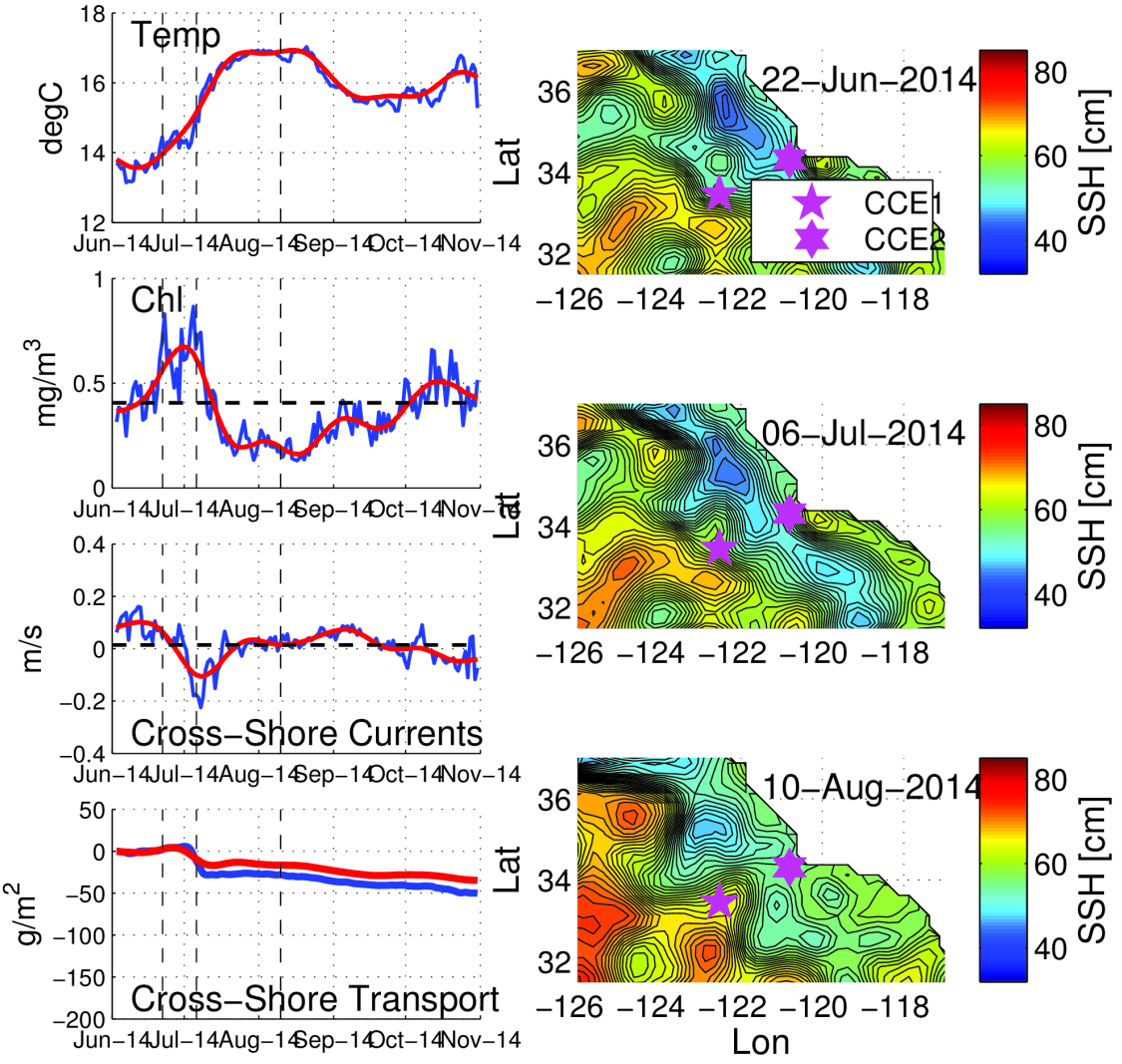

Figure 2.9: Same as previous, but for CCE1, June to Nov, 2014. This shows the CCjet quickly advecting past the mooring, transporting chlorophyll to the offshore.

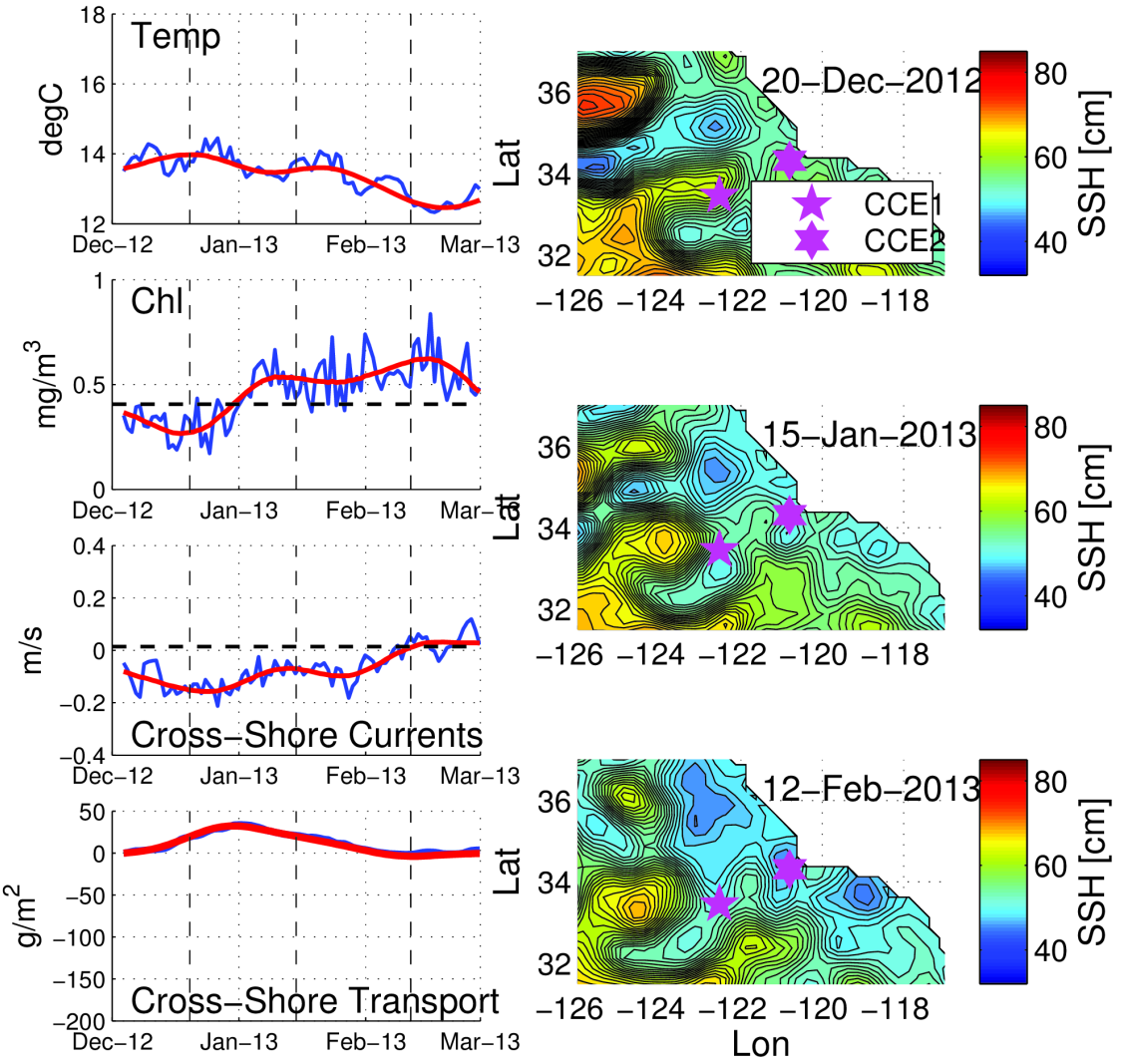

Figure 2.10: Same as previous, but for CCE1, Dec-2012 to Mar-2013. Combined, these show a warm core eddy advecting low chlorophyll water offshore, counter to the previous figures.

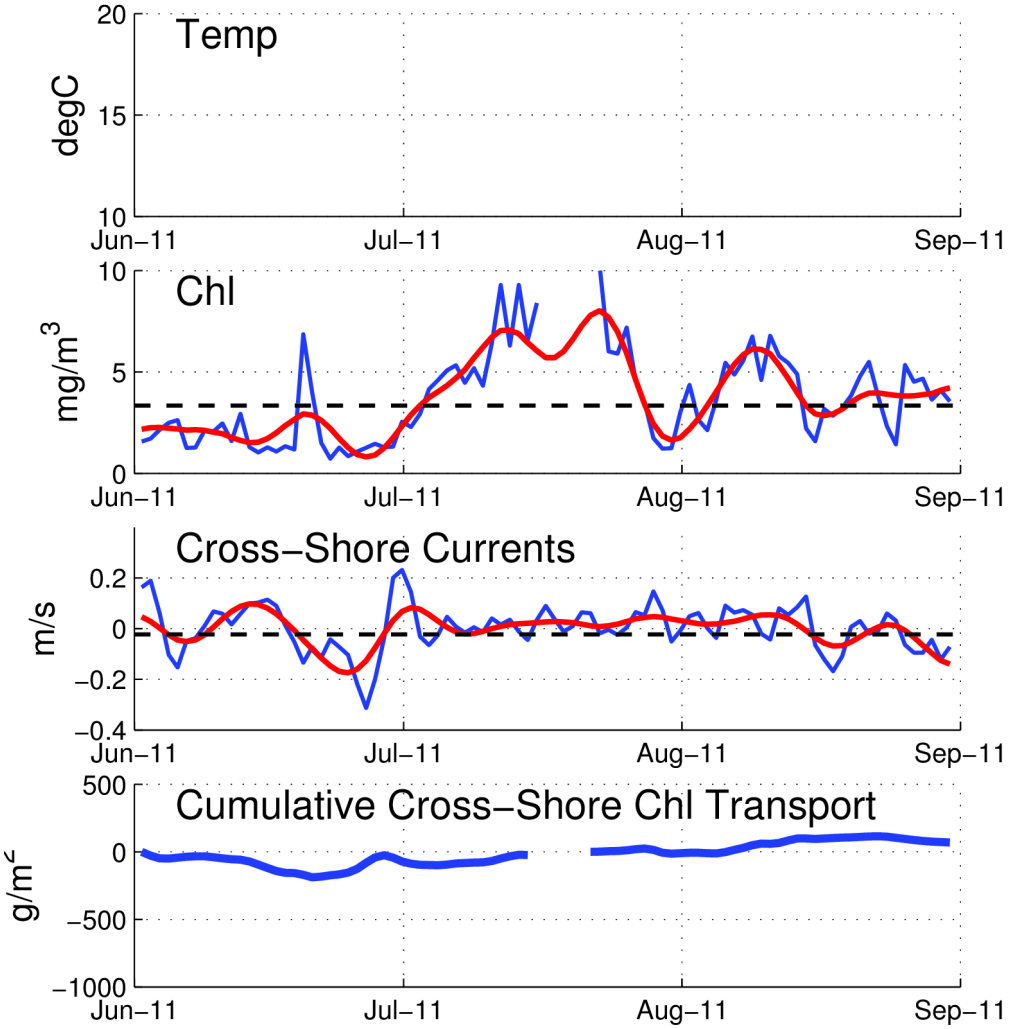

Figure 2.11: The CCE2 equivalent of the previous figures. Here red lines represent a low-pass filter of 15 days, and there are no AVISO plots. Presented here is a single large upwelling even in late June, though it has little corresponding chlorophyll transport.

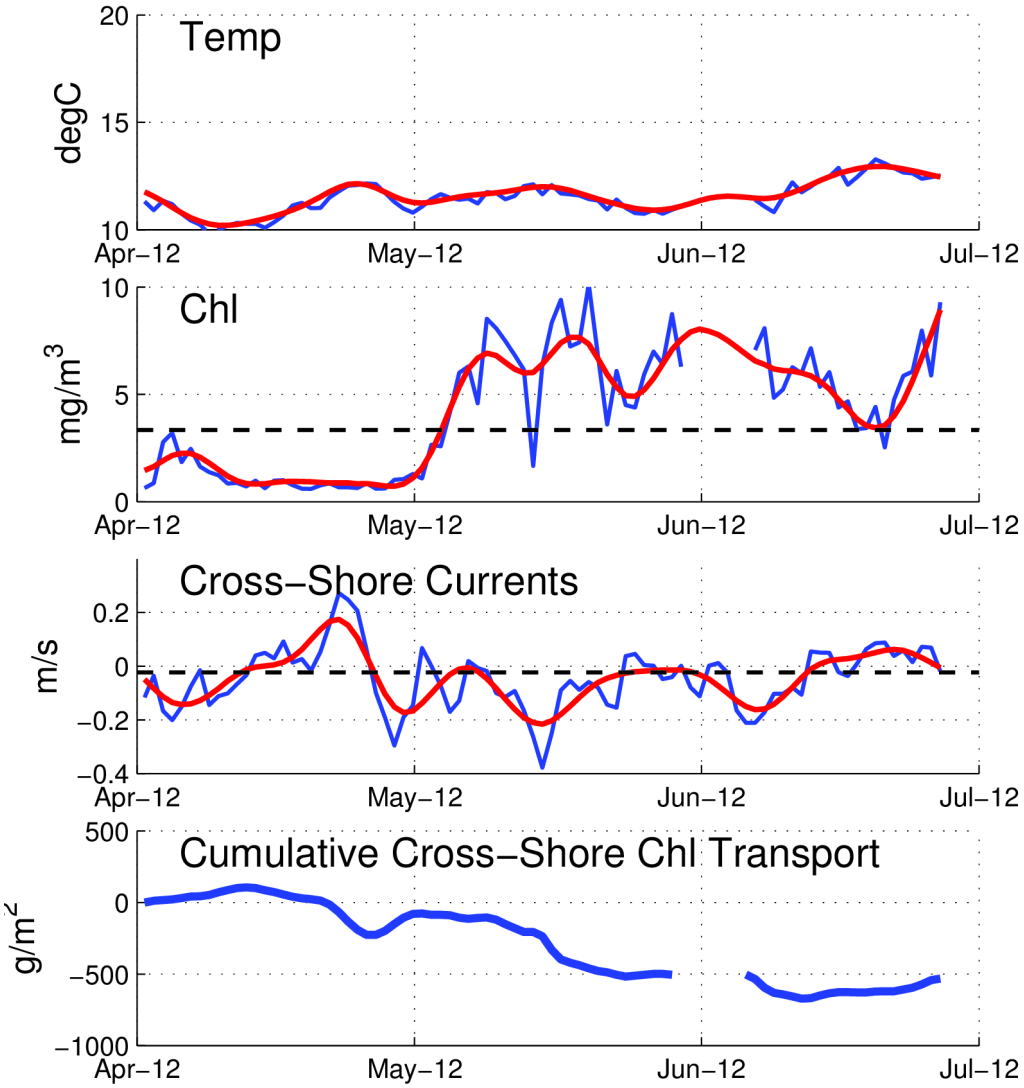

Figure 2.12: Same as previous but for CCE2, Apr-2012 to June-2012. The focus here is several upwelling events in early May, mid-May, and early June; the quick succession of events causes a large offshore transport of chlorophyll, discussed in the text.

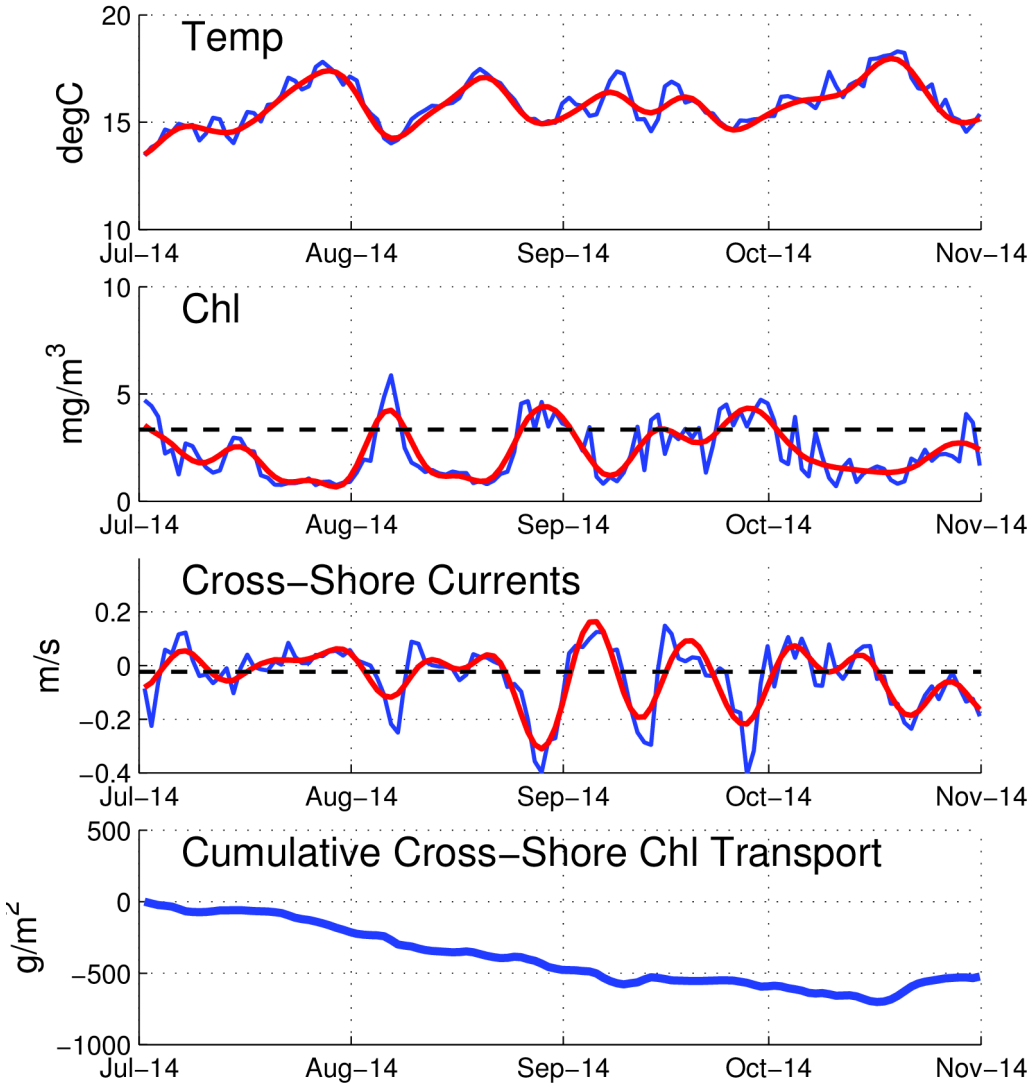

Figure 2.13: Same as previous but for Jul-2014 to Nov-2014. The focus here is a gradual offshore eddy transport associated with low chlorophyll during the Warm Blob in late 2014.

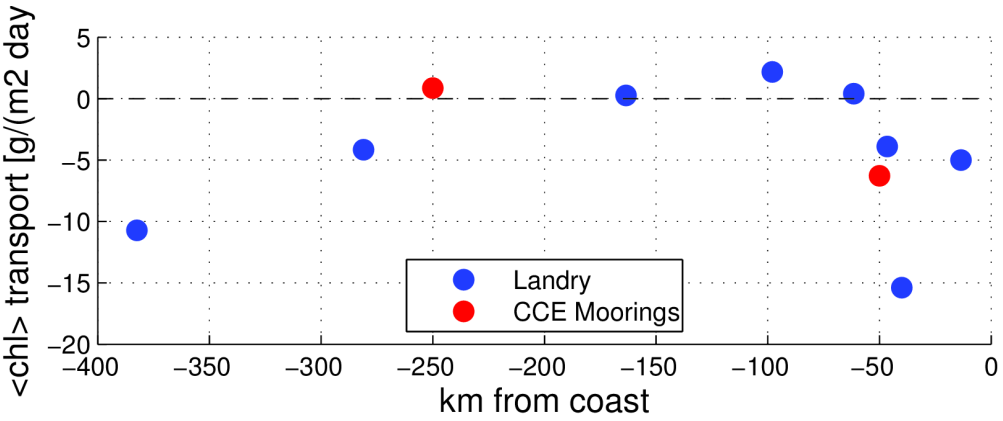

Figure 2.14: Chlorophyll transport calculated from Landry et al. 2009 (blue) and the CCE moorings (red).

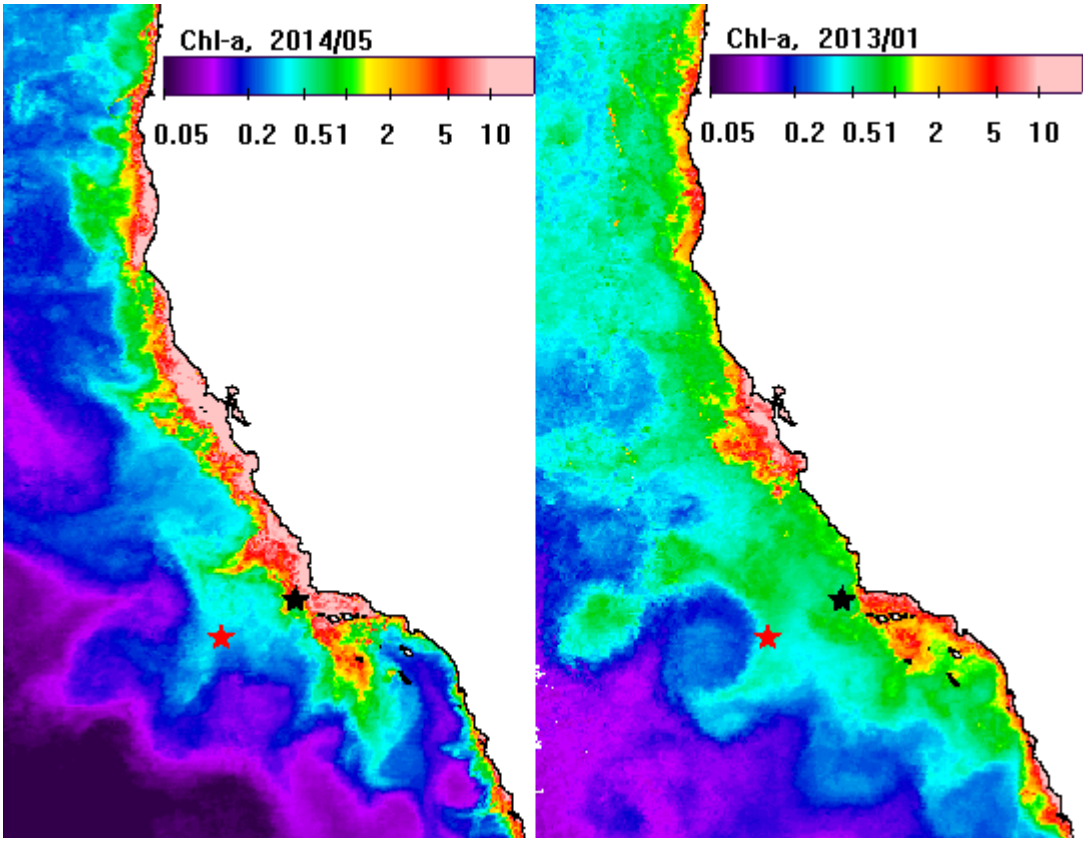

Figure 2.15: Merged, monthly satellite images during the time series represented by figure 2.Error: Reference source not found (left) and figure 2.Error: Reference source not found (right).The red star represents the location of CCE1 and the black star represents the location of CCE2.Satellite pictures provided by B. Greg Mitchell and Mati Kahru.

CHAPTER 3: PHYSICAL DRIVERS RELATIVE TO THE ANNUAL SPRING BLOOM INITIATION: A STUDY IN THE LIGURIAN SEA

Introduction:

The annual spring bloom is a dominant feature in the oceanic carbon cycle and a major mechanism for energy entering the food chain. The initiation of the spring bloom is not perfectly understood, with several major hypotheses put forward [*Behrenfeld and Boss*, 2014]. One of the issues with defining the initiation of the spring bloom is lack of in situ chlorophyll measurements, which require frequent and consistent vertically resolved information for the water column.

The Buoy for the Acquisition of Long-term Optical Time Series (BOUSSOLE) mooring in the Northwest Mediterranean Sea (see figure 3.1) is an optical mooring coupled with monthly hydrographic cruises, frequently used in calibrating satellite sensors [*Antoine et al.*, 2006; *Organelli et al.*, 2014]. Among the optical measurements are moored multi-wavelength irradiance sensors above the surface and 9 meters below the surface; there are also fluorometric counts at 4m and 9m. A new chlorophyll-retrieval technique [*Wilson et al.*, 2016] was developed which returns average chlorophyll concentration for the layer between the moored irradiance sensors. Once applied to BOUSSOLE, a daily time series for 9 years of average chlorophyll over the 0-9m layer is available, along with several other hydrographic variables and monthly hydrographic sampling. These data are used to understand timing and formation of the spring bloom

along with several physical drivers in the region.

An interesting feature in the seasonal bloom cycle is a bloom hiatus, where the surface bloom signature actually lapses before increasing to the year's maximum chlorophyll value. These have been observed before in the Mediterranean Sea [*Bernardello et al.*, 2012] and North Atlantic [*Brody et al.*, 2013]. Through an analysis of the model-returned chlorophyll presented here and oceanic heat flux over the 9 years, the hiatuses appear to be correlated with events that can mix the water column (e.g. periods of high wind and/or upward heat fluxes). These hiatuses in surface chlorophyll can be explained by dilution of existing chlorophyll concentrations due to an increased layer depth. They are ecologically important as they have the potential to mix organic material to depth [*Bernardello et al.*, 2012], and increased mixing has been shown to delay blooms in the North Atlantic [*Henson et al.*, 2009].

This work applies a new chlorophyll retrieval method to moored measurements of irradiance in the Data section. This new time series resolves inter-annual variations in the spring bloom, providing hydrographic context with heat fluxes and temperature signals in section titled Timing of the Spring Bloom. In the Bloom Hiatus Event section, these relationships are discussed, and heat flux events are shown to decrease 0-9m chlorophyll concentration, both in the model-returned values and monthly profiles. The result of this work is an increased understanding of bloom timing in the Northwestern Mediterranean Sea, and an investigation of lapses in spring bloom development.

Data

The primary dataset used in this study is a mooring-derived time series following

[*Wilson et al.*, 2016]. Aspects of that method were developed in order to apply the technique at the BOUSSOLE site, though there are some additional considerations in applying the method here; they are described below. Additional time series providing hydrographic context are also discussed.

BOUSSOLE

The BOUSSOLE Mooring is well established in the optics community, with several research efforts using the available data [*Organelli et al.*, 2014] and published methods for data collection [*Antoine et al.*, 2006]. The optical measurements used in this model are the radiometers at approximately 4.5m (E_0) above the surface and 9m below (E_d) the surface. They measure at 15-minute intervals, and collect irradiance at [442.5, 490.0, 510.0, 560.0]nm and one of [412.5, 555.0] nm, depending on deployment; there are several wavelengths above 600nm, but they are often attenuated and are not used in this model. A single measurement consists of 360 samples of irradiance and buoy tilt in one minute; the median of these samples for each wavelength is used as the measurement. The reflection is handled as described in [*Antoine et al.*, 2006], and diffuse attenuation (k_d) is found using the Beer-Lambert law; $k_d = \frac{-\log(E_d/E_0)}{z}$. The rigid structure of the mooring can cause the effective depth (z) to be greater or less than 9m, so the true depth is found by applying tilt measurements to the geometry of the structure [*Antoine et al.*, 2006]. The E_0 measurements are ignored when the surface instruments are below the water level, which only occurs under extreme conditions. Just as in [*Wilson et al.*, 2016], only measurements with the zenith angle less than 70° are

used in this model-application. Finally, in 2.5% of measurements, the diffuse attenuation is less than the absorption and backscattering of pure water. This can only occur through ray focusing [*Zaneveld*, 1989; *Zaneveld et al.*, 2001], so the data are ignored. In total, the model is applied to 72339 spectra over 2308 days.

A Meteorologial Buoy maintained by the French weather forecasting agency is approximately 3km from the mooring and features a Vector Instruments anemometer providing wind speed and direction at 3.5m above the surface. It is assumed the atmospheric and biological measurements at both locations are the same [*Marty et al.*, 2002; *Antoine et al.*, 2006]. Spatial and temporal measurements in this region have shown that consecutive biological measurements (less than 1 day apart) were larger than variations in adjacent stations (greater than distance between moorings) and that advection is weak in this region [*Andersen and Prieur*, 2000; *Andersen et al.*, 2001].

Hydrographic cruises visit the mooring location each month. Profiles of temperature from a CTD package and chlorophyll-a from an HPLC analysis applied to bottle samples are used here. The process by which these data are collected is heavily documented by [*Antoine et al.*, 2006].

Daily chlorophyll has been derived at the mooring by normalizing the satellite sensors to the HPLC product [*Antoine et al.*, 2008; *Kheireddine and Antoine*, 2014]; while the satellite-based product is helpful in confirming some analyses, it has assumptions associated with it that makes it less ideal than the chlorophyll model presented here. Similarly, there exist fluorometric measurements at 4m and 9m on the BOUSSOLE mooring which can be used as a proxy for chlorophyll-a measurements

[*Antoine et al.*, 2006]. These measurements require empirical corrections using the monthly chlorophyll measurements, and assumptions about how those adjustments are applied ([*Marcel et al.*, 2008 and *Vincenzo Vellucci*, personal communication]. Bio-fouling can present itself as linear drift or step functions, and the priority for the monthly visits is to clean the radiometric sensors, not the fluorometers [*Antoine et al.*, 2006]. The calibration assumptions and/or the potential for biofouling make the retrieval method presented here a more viable time series for the 9 year analysis than both the fluorometric counts and normalized satellite products.

Chlorophyll Model

Chapter 1 fits the absorption and backscattering spectra of constituents in the water column to the measured diffuse attenuation. The model was developed at the BOUSSOLE site, so the various model constituents and spectra are known; specifically, the spectral coefficients for a chlorophyll absorption, A_p and E_p. The general values for particulate backscattering, water absorption, and water backscattering are taken from the literature, and the terms for converting absorption plus backscattering to diffuse attenuation (D_1 and D_2) are taken from Chapter 1.

A feature in the Chapter 1 algorithm is the ability to exchange modules and the CDOM module has been updated to better represent the observed diffuse attenuation at BOUSSOLE. CDOM is represented by the exponential function from [*Bricaud et al.*, 1998]; $a_s(\lambda)=a_s(440\text{nm})\ \exp\left(-s(\lambda-412)\right)$. Using this in the algorithm assumes that the exponent s is independent of $a_s(440\text{nm})$. [*Organelli et al.*, 2014] has shown that these two variables have a dependency (figure 7b in that work), and the

relationship was found as $s = 0.008 * a_s(440)^{-0.205}$, with $r^2 = 0.60$ and $n = 34$ (Organelli, personal communication). This new representation of s has been applied here.

Model Application and Validation

The algorithm defined by equations 1.4, 1.5, and 1.6 from [*Wilson et al.*, 2016] is applied just as it is in that work. Each of the observed measurements has 20 iterations of the model run with the same error considerations described in Chapter 1. The median of all iterations during a single day is used as the chlorophyll concentration for that day, and resulting spread of these measurements is due to both median standard error calculated during the application of the algorithm and phytoplankton patchiness over a day [*Franks*, 2005]. Figure 3.3 provides the full time series; in total, there are 2308 days of chlorophyll concentration over 9 years.

For validation, we use chlorophyll concentrations measured during the monthly cruises visiting the BOUSSOLE site. For appropriate comparison, profiles of chlorophyll are averaged to 9 meters. The bottle samples are linearly interpolated between measurements, and assumed constant for the layer above the most shallow measurement. There must be at least one measurement more shallow than 9 meters and one measurement deeper than 9 meters, and the linear interpolation is averaged for the upper 9 meter layer. Figure 3.2 gives a direct comparison of the model with the monthly chlorophyll. The spread relates to the full spread of 20 model iterations for each measurement. Over all, comparison is strong though variations do exist; with n=202, the correlation of 0.7165 in linear space and 0.4855 in logspace. The largest deviations from

the one-to-one relationship are a group of bottle-measured chlorophyll in the range of 1 mg/m^3 , where the model estimates chlorophyll of approximately 2 to 3 mg/m^3 . These examples are often collected from the research vessel in times of high model variability, either preceding or following abrupt changes in chlorophyll concentration. More work needs to be done, for example, to explain why the method consistently overestimates the results. It may be that a single measurement of chlorophyll may not accurately represent the median chlorophyll concentration over the entire day.

The new CDOM module improves the model. The original optical description of CDOM has a standard error of 3.07e-4 $1/m$, while this new CDOM module has a standard error of 1.21e-4 $1/m$. These are often isolated in specific days. For example, on 2006-April-3, the model returns 8.3 mg/m^3 using the old method, and 1.05 mg/m^3 using the new module; the monthly chlorophyll value is 1.54mg/m^3 . One reason this works so well in the BOUSSOLE region is the relationship between CDOM and chlorophyll concentration and s coefficient [*Organelli et al.*, 2014]; forcing *s* to be the average and/or median value would emphasize the more common low chlorophyll non-blooming conditions and systematically return incorrect chlorophyll during high chlorophyll, blooming conditions. For these reasons, the new CDOM module is used in the model application for chlorophyll at BOUSSOLE.

NCEP/CFSR Products

Also presented here are total heat flux and heat flux components from the NCEP reanalysis [*Kalnay et al.*, 1996]. Mixed-layer depth (MLD) estimates from CFSR [*Saha et al.*, 2010] are also used. Both time series provide atmospheric and hydrographic

context for the analysis presented here. Future work should validate these mixed-layer depth estimates against ship-board data measured during the BOUSSOLE monthly cruises.

Timing the Spring Bloom

Methods

Many previous methods to estimate bloom timing (cumulative biomass method, threshold-based method, and rate of change method) [*Brody et al.*, 2013] fail here due to the gaps in the time series. A cross-correlation method can work because it matches all the measurements which are available between years. For example, the peak correlation between 2011 and 2005 (i.e. Sept-2010 to Aug-2011 and Sept-2004 to Aug-2005) is assumed to represent the delay in the spring bloom between these two years, and the correlation is highest when the 2011 chlorophyll cycle is referenced 21 days before 2005. If each year is compared in the same way with every other year, a lag between each year is developed. Table 3.1 gives those lags, and is symmetrical along the diagonal. The median of each column finds a reference lag for each year. For example, the median lag for 2005 compared to all other years shows the chlorophyll signal for 2005 occurs 20 days late; for 2011, it occurs 15 days early.

In figure 3.4 (top), the January to May model-returned chlorophyll is stacked according to the measured day of year; the reference lags are applied to the chlorophyll time series and replotted in figure 3.4 (middle), tightening the date on which the bloom was at a maximum. This result is highlighted by the peaks in 2004, 2005, 2006, and 2011. The reference lags are plotted by year in figure 3.4 (bottom), with the blue calculated

from the model chlorophyll time series and the green calculated from the diffuse attenuation at 490nm ($k_d(490\text{nm})$). The resulting signal appears to be a sinusoid with approximately 10 year cycle. With the model-derived lags applied in figure 3.4 (middle), the chlorophyll measurements are associated with a reference day of year. A running 10-day mean is applied using these appropriate day-of-year (raw in figure 3.4 (top) and lag-reference in figure 3.4 (middle)) for the stacked 8 years of model-returned chlorophyll, returning the thick black line in the plots. This is considered the cycle for this period of time, and the correlation between this cycle and the time series tests the ability for this cycle to represent the chlorophyll concentration leading up to the bloom maximum. If the correlation is significantly improved when the reference lags are applied to each year, the reference lags may have a physical meaning in that time series.

The reference lags calculated from the model-returned chlorophyll are applied to other time series, and the results are given in figure 3.5. The referenced $k_d(490\text{nm})$ measured from the mooring is given in figure 3.5 (top left). The referenced bottle chlorophyll measured during the monthly cruises is given in figure 3.5 (top right). The HPLC-referenced satellite product [*Antoine et al.*, 2008] is plotted in figure 3.5 (middle left). The referenced wind speed measured from the Meteo mooring is given in figure 3.5 (middle right).

Finally, figure 3.5 (bottom left) and (bottom right) give the reference time series of total heat flux and mixed-layer depth, respectively, derived from climate reanalyses [*Kalnay et al.*, 1996; *Saha et al.*, 2010]. Total heat flux is the daily averaged NCEP reanalysis heat flux for the 0.5x0.5 degree box which contains the BOUSSOLE mooring.

The mixed-layer depth is the daily averaged CFSR reanalysis mixed-layer depth (MLD) for the 0.5x0.5 degree box which contains the BOUSSOLE mooring. These re-analyses have potential to make claims about the spring bloom timing [*Sallée et al.*, 2015]. In this analysis, the NCEP heat flux is used to compare with time series from the mooring and the CFSR MLD product provides context for the cycle of MLD.

The colors in each of the 8 time series in figure 3.5 match the year/colors in figure 3.4. The referenced cycle is calculated for each January to May time series as it was for chlorophyll in figure 3.4, and given as the thick black line in their respective plots. This cycle is replotted for in figure 3.6 for chlorophyll, wind speed, NCEP heat flux, and CFSR MLD; each has been normalized by their maximum value to be easily comparable.

Results

The simple lag correlation technique does not replace the many techniques used to describe the timing of the spring bloom initiation [*Henson et al.*, 2009; *Brody et al.*, 2013]. This method is built on correlation coefficients, so extreme values are the primary driver of calculating the lags. For example, figure 3.3 dictates there were elevated chlorophyll values in December and January preceding the 2007 spring bloom. The monthly cruises returned average chlorophyll concentrations of $0.73\,mg/m^3$ in early December and $0.78\,mg/m^3$ in the late January cruises. In 2005, neither the monthly cruises nor the model-returned chlorophyll rose above $0.50\,mg/m^3$ until March. The lag-correlation method does not focus on this 2- to 3-month delay in growth initiation, but instead focuses on the differences in their relative maximums. More work is needed to examine how smaller variations and gaps in the time series influence this definition of

timing. By the lag-correlation method, the 2005 bloom occurs 9 days after the 2007 bloom.

The January to May cycle of each year is plotted in figure 3.4, with and without the reference lags applied; the reference-lags' effect is easily visible where the bloom peaks are brought together in late March. The lag correlation method was applied to both the full year and the Jan-May (5 month) period of time with no difference to the calculated reference lags for the model-returned chlorophyll, and changes of less than 5 days for 2009 and 2010 and the same otherwise. The 5-month reference lags derived from the model-returned chlorophyll are used in this work unless otherwise noted.

Using the lag correlation method, the model-returned chlorophyll estimates that the bloom varies by 29 days (21 days for $k_d(490\text{nm})$). A similar magnitude in bloom initiation variability has been seen in the North Atlantic [*Henson et al.*, 2009; *Brody et al.*, 2013] and the Northwestern Mediterranean [*Bernardello et al.*, 2012]. In the bloom lags calculated in this work for the Northwestern Mediterranean, a cycle of 9 years or longer could explain the interannual trends. Similar-length periods of variability exist in the bloom start date record for the North Atlantic [*Henson et al.*, 2009].

The cycle in figure 3.6 provides a basic understanding of the cycle for some hydrogprahic processes from Jan to May. In early January, the upward heat flux is high, the MLD is increasing, wind is high, and the chlorophyll is low and rising. There is a drop in wind and NCEP upward heat flux, during a rise in chlorophyll in January. Wind and heat flux rise again, and chlorophyll drops. MLD is deepest in February, and chlorophyll starts increasing again. Chlorophyll increases until a peak in late March, after

which it declines. NCEP turbulent heat flux and winds start decreasing, and sporadically continue to decreases through the end of May. The MLD increases until May, after which it is constant.

The ability for these calculated annual cycles to represent their raw signal is estimated using the correlation before and after the references have been applied, as described in the Methods section. If the lags cause an increase in correlation between the cycle and signal, the lags may correspond to a measured delay in the time series.

Table 3.2 gives the correlation between the signal and the annual cycle for each time series, using the raw signal and the reference lags calculated from the model time series. The Fisher z transformation can be used to evaluate whether the differences in correlation coefficients in table 3.2 are significant. The model-returned chlorophyll, $k_d(490\text{nm})$, and satellite chlorophyll product are improved with some significance using the model-derived chlorophyll lags. Hydrographic chlorophyll is improved, but not significantly, given the sparse measurements. Wind and NCEP heat flux are not significantly improved, and correlation with the mixed-layer depth is made worse by the lag-references. The important concept in these correlation comparisons is that the lag-references are a feature in the interannual chlorophyll signal. It does not appear this technique describes a lag in the NCEP heat fluxes, wind, and MLD, but they play a role in understanding bloom hiatus events.

Bloom Hiatus Events

Methods

The second half of the analysis focuses on several hiatuses in the spring bloom,

defined here as the model-returned chlorophyll concentration decreasing before the maximum spring bloom 0-9m chlorophyll concentration occurs. These can be seen most easily in figure 3.3, years 2005, 2007, and 2009, though other examples exist.

Figure 3.7 gives stacked, reference-lagged time series' of model-returned chlorophyll (blue), hydrographic chlorophyll (red), windspeed (pink), and NCEP upward heat flux (green). In 2005, 2007, and 2009 (and other years, though these are most pronounced), one or more bloom hiatuses occurs before this maximum value, accompanied by a rise in upward total heat flux. These events seem to have an inordinate impact of the timing of the spring bloom, as defined by the correlation lags above. Through chlorophyll profiles and the 0-9m chlorophyll time series, a characteristic chlorophyll hiatus is investigated.

The chlorophyll signals from 2005, 2007, and 2009 are isolated in figure 3.8 (top) which gives the model-returned (gray) and cruise-measured, monthly chlorophyll (red) levels, referenced to the model-returned lags. These years are chosen because they experience a chlorophyll hiatus during the lag-referenced March 5 to March 10. The black line gives the average cycle for these three years, calculated as the annual cycle was in figure 3.5. Several of the monthly chlorophyll events are highlighted, with the corresponding profile example provided in the bottom rows in figure 3.9. While ideally, these profiles would be taken from the same year, the cruises only last 2-3 days, so could not capture a full hiatus events, which typically last 4-8 days. However, the profiles within a single plot are from the same year. The profiles here are assumed to represent a characteristic hiatus event, which corresponds to a lag-referenced period from March 5 to

March 10.

Results

Figure 3.7 gives the normalized time series' of model-returned chlorophyll and NCEP upward heat flux. The highlighted events are the LCJA, which are often accompanied by a drop in chlorophyll concentration. [Bernardello et al., 2012] used a biogeochemical model to show that during high upward heat flux events in 2008 and 2005, the vertical nitrogen export flux increased. In their work, they found the windspeed and upward heat flux increased, MLD deepened, phytoplankton concentrations in the surface layer decreased, and export flux of nitrogen increased. This implies organic material is mixed downward during these surface heat flux events. [*Henson et al.*, 2009; *Brody et al.*, 2013] discussed the delay of the spring bloom, mentioning events where the chlorophyll stops growing or even decreases. These hiatuses and heating events are therefore important for the timing of the spring bloom and the downward flux of organic material.

The profiles in figure 3.8 are used to represent five stages. In order, they are (1) low chlorophyll before the bloom begins, (2) high chlorophyll with the hiatus beginning, (3) well mixed chlorophyll with the main bloom beginning, (4) high chlorophyll during main bloom, and (5) chlorophyll dropping after the main bloom. The dates in the profiles give the lag-referenced dates using the model-returned chlorophyll, and they are color-coordinated in the time series. Though the individual stages may be from separate years, all of the profiles within a single plot are from the same year.

The profiles follow expectations associated with this dilution theory. The bloom is

focused in the surface (04-Mar-2005), until the 0-9m chlorophyll drops from 2.49 to $2.00\,mg/m^3$ as the chlorophyll layer deepens (05-Mar-2005); over this period, the integrated chlorophyll to 80m increases from 1.50 to $1.73\,mg/m^3$. The hiatus exhibits well-mixed chlorophyll (12-Mar-2009), and eventually growth begins near the surface (13-Mar and 14-Mar-2009), and continues to rise (25-Mar and 28-Mar-2005). The surface signature of the chlorophyll bloom decreases as the bloom is diluted to depth [*Marty et al.*, 2002; *Behrenfeld and Boss*, 2014] (30-Mar to 31-Mar-2007). Though this work focuses on the extreme examples for these three years, more work is needed to understand how each cooling event, a bloom can develop.

Heat loss events can deepen the mixed-layer either by convective overturning [*Killworth*, 1983] or wind mixing [*Price et al.*, 1986]. It is proposed that when a significant heat loss and/or wind event occurs in the spring, the surface chlorophyll signal drops because the chlorophyll has been diluted due to a deeper mixed-layer. A significant upward heat flux event is defined here as the NCEP upward heat flux above $100\,W/m^2$. The last significant upward heat flux event in the months of January to April (LCJA) is represented by the vertical dotted line in figure 3.7 for each year, and they follow a similar pattern to the model-derived chlorophyll lags. Figure 3.9 shows the relationship between the chlorophyll lag and the last date of upward heat flux greater than $100\,W/m^2$. That relationship has $r^2=0.88$ with $p<0.01$. The cycle of the LCJA and chlorophyll lags is given in the bottom plot on figure 3.9, along with the average CFSR mixed-layer depth from January to April. These results are discussed in the discussion section.

The timing of the chlorophyll bloom in the Northwestern Mediterranean Sea can shift in date on the order of 30 days. A feature of these blooms are lapses in surface chlorophyll growth, which can coincide with increased heat flux out of the water. A characteristic year of chlorophyll profiles during a hiatus event is presented. The chlorophyll layer becomes thicker, diluting the chlorophyll concentration while increasing the integrated values. The LJCA is shown to be significantly correlated with the chlorophyll lag (figure 3.9), and the mechanism for chlorophyll dilution is shown through characteristic profiles (figure 3.9, bottom plots) which often correspond to cooling events. These results suggest the LJCA is the primary determinant of the model-derived chlorophyll lags measured in the previous section.

Discussion

Full Picture of Bloom

[*Behrenfeld and Boss*, 2014] discuss three main bloom initiation hypotheses; the classic critical depth theory, the critical turbulence theory, and the disturbance recovery theory. The work presented here, does not attempt to delineate between the bloom initiation hypotheses, and focuses only on the surface signature of the chlorophyll bloom. There is an opportunity to apply similar techniques as described here for a full understanding of the full spring bloom.

Several measurements that can help in understanding the spring bloom intitiation are integrated chlorophyll and mixed-layer depth, which could potentially be recovered with a deeper irradiance sensor and vertically-resolved temperature sensors. Chapter 1 developed and applied this model to the BOUSSOLE work for the 10m, 40m, and 80m

surface layer, and Chapter 2 applied this technique to mooring measurements in the California Current System for 40m and 80m. The mixed-layer depth has been estimated using moorings previously [*Cronin and Kessler*, 2002; *Weller et al.*, 2002], if the temperature sensors have sufficient vertical resolution. A mooring design with paired radiometers encompassing 80m and multi-depth MicroCATs collecting CTD measurements, could provide the resolution to resolve the onset of the spring bloom with simultaneous MLD estimates.

Vertical Export through Hiatuses

These hiatuses have been observed to increase nitrogen export flux by [*Bernardello et al.*, 2012], who described a hiatus in mid-April, 2005, using basin-wide satellite records and a bio-geochemical model. Their biogeochemical model by a basin-wide upward heat flux event. This event is seen in the wind record (figure 3.7, pink line, ~2005-April-12) and the subsequent bloom hiatus (figure 3.7, blue line, ~12-April-2005). Interestingly, the BOUSSOLE record describes an additional hiatus event in both the model and monthly chlorophyll profiles (figure 3.7, blue line & red dots, ~25-Mar-2005, also presented in figure 3.8 profile 2). The change in chlorophyll profiles described in figure 3.9, profile 2 would not be described in the [*Bernardello et al.*, 2012] 0-75m chlorophyll layer, but would be described in the 0-9m chlorophyll layer of the model. The 12-April-2005 event does have a 75m nitrogen export signature, but the 25-Mar event does not; again, this is not as unexpected as the event on 25-Mar and only seems to affect the chlorophyll layer to a depth of 60m. Still, more information is needed to determine the extent of the vertical transport of organic material during these bloom hiatuses.

Interannual Bloom Timing

Presented here are 8 lags associated with the surface signature of the spring bloom at the BOUSSOLE mooring location, calculated through lag correlation between different years of the model-derived chlorophyll concentration. These lags have been shown to significantly improve the signal in the cycle description for $k_d(490\text{nm})$ and a satellite chlorophyll product; they are a feature of the spring bloom.

Previously, such lags have been correlated with the maximum depth of the mixed-layer in the North Atlantic by [*Henson et al.*, 2009], who suggested that the chlorophyll bloom occurs later when the mixed-layer is deep. Figure 3.9 (top right) shows the relationship between the average MLD between January to April for each year, showing the opposite of what [*Henson et al.*, 2009] describes. The chlorophyll bloom occurs earlier when the mixed-layer is deep using the model-derived chlorophyll lags. The correlation also holds between lags calculated for $k_d(490\text{nm})$ (i.e. green dots in figure 3.4, bottom) and the average MLD for January to April is $r^2=-0.73$ with $p<0.1$. The LCJA has been suggested as the primary determinant of the spring bloom timing in the Northwest Mediterranean Sea. This has a strong correlation with spring bloom lag, and the mechanism illustrates how such cooling events could delay the bloom. The correlation between the $k_d(490\text{nm})$ lags and LCJA has $r^2=0.86$ with $p<0.01$.

The 2009-2010 winter was considered extreme and associated with a large negative phase of the North Atlantic Oscillation (NAO) [*Cattiaux et al.*, 2010]. It features a very early LCJA, early bloom, and deep mixed-layer. The NAO is not significantly correlated with the signals presented here (bloom lags, average MLD, LCJA) despite a

relative minimum in all three time series for the 2010 spring bloom.

This analysis has shown that the LCJA events dilute 0-9m chlorophyll concentrations and delay the signature of the spring bloom. The reason for the timing of the LCJA or the values of the MLD should be investigated further.

Conclusion

A new time series for chlorophyll has been described at the BOUSSOLE site. A correlation method describes reference lags, showing that the spring bloom varies by 30 days over the 9 years sampled. The lags have been applied to heat fluxes and physical time series at the mooring, describing improved agreement between the signal and calculated cycle in several cases. This means the atmospheric signals and the chlorophyll bloom could be related, though the relationship is known to exist [*Henson et al.*, 2009]. One such example of the relationship between the chlorophyll bloom and the atmospheric signal is with bloom hiatuses during heat flux events.

These heat flux events potentially dilute the chlorophyll concentration over a deeper layer. This dilutes the surface chlorophyll concentration, potentially increases the vertical flux of organic material, and delays the spring bloom's arrival.

Chapter 3, in part, is currently being prepared for submission for publication. Co-authors include Send, Uwe; D. Antoine; J. Uitz. The dissertation author was the primary investigator of this material. The data were collected from the Buoy for the acquisition of long term optical time series (BOUSSOLE). The BOUSSOLE team at Laboratoire Oceanographique de Villefranche was instrumental in collecting that data. The National Science Foundation, Graduate Research Fellowship and Chateaubriand Fellowship

funded this analysis work.

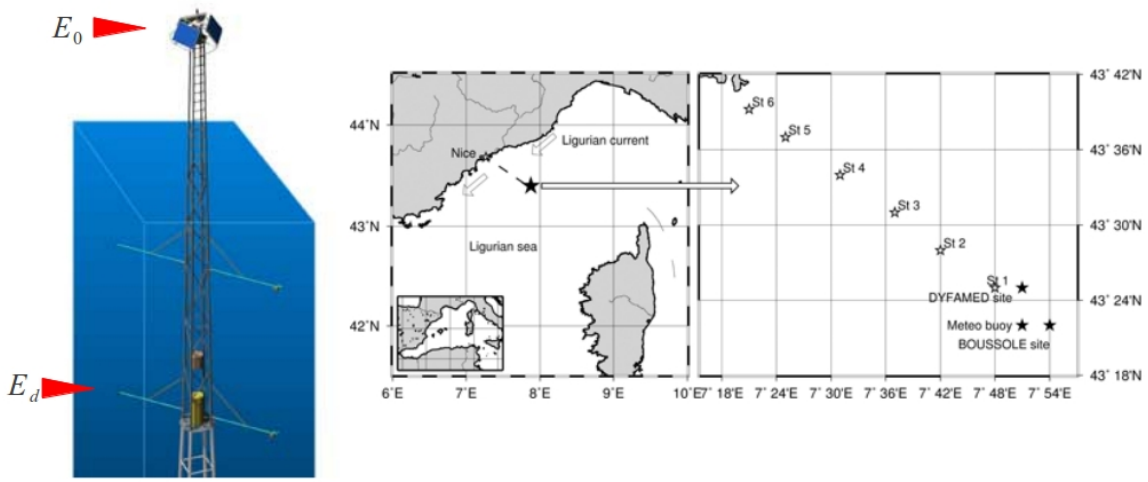

Figure 3.1:Diagram of mooring (left), with the irradiance sensors used in this analysis highlighted. E_0 is approximately 3 meters above the surface, and E_d is approximately 9 meters below the surface. The map gives the location in the Ligurian Sea, along with the nearby DYFAMED site.

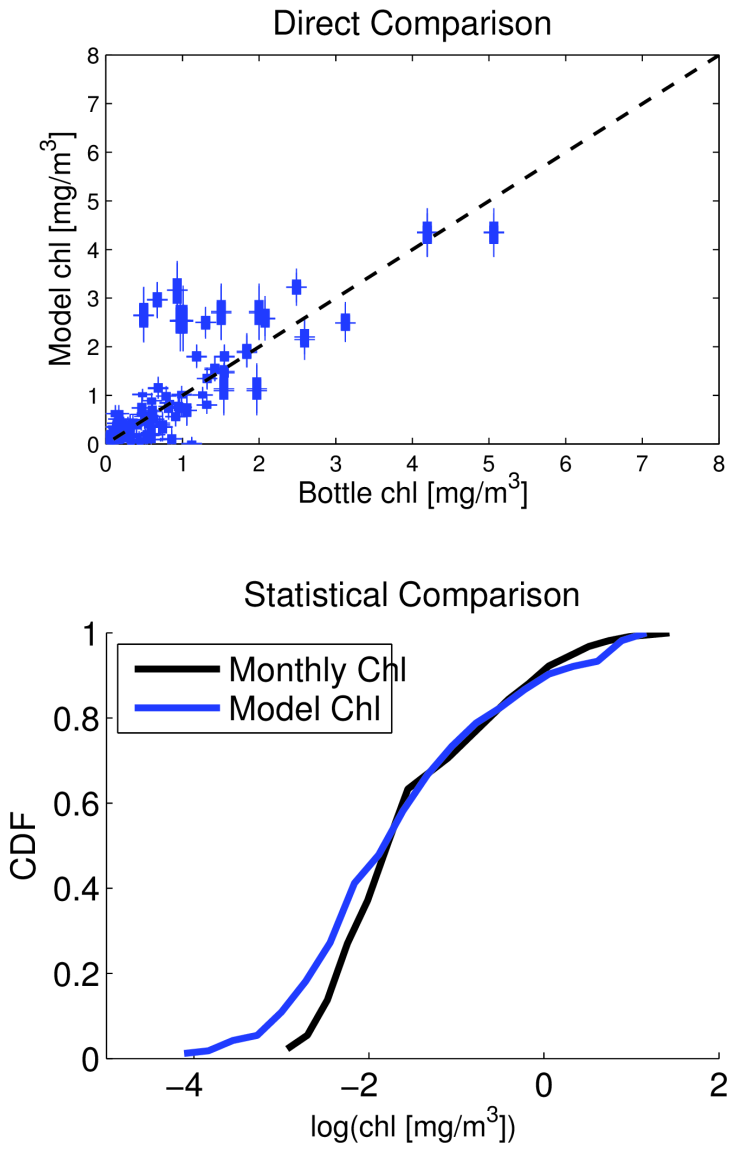

Figure 3.2: (top) Direction comparison monthly-chlorophyll and model-returned chlorophyll. More work is needed to explain the overestimated values with model-returned values of approximately 3 $mg/m^{\dot{c}}$. They exist due to patchiness in the region during times of high variability. (bottom) Cumulative distribution function of both of Monthly and Model chlorophyll.

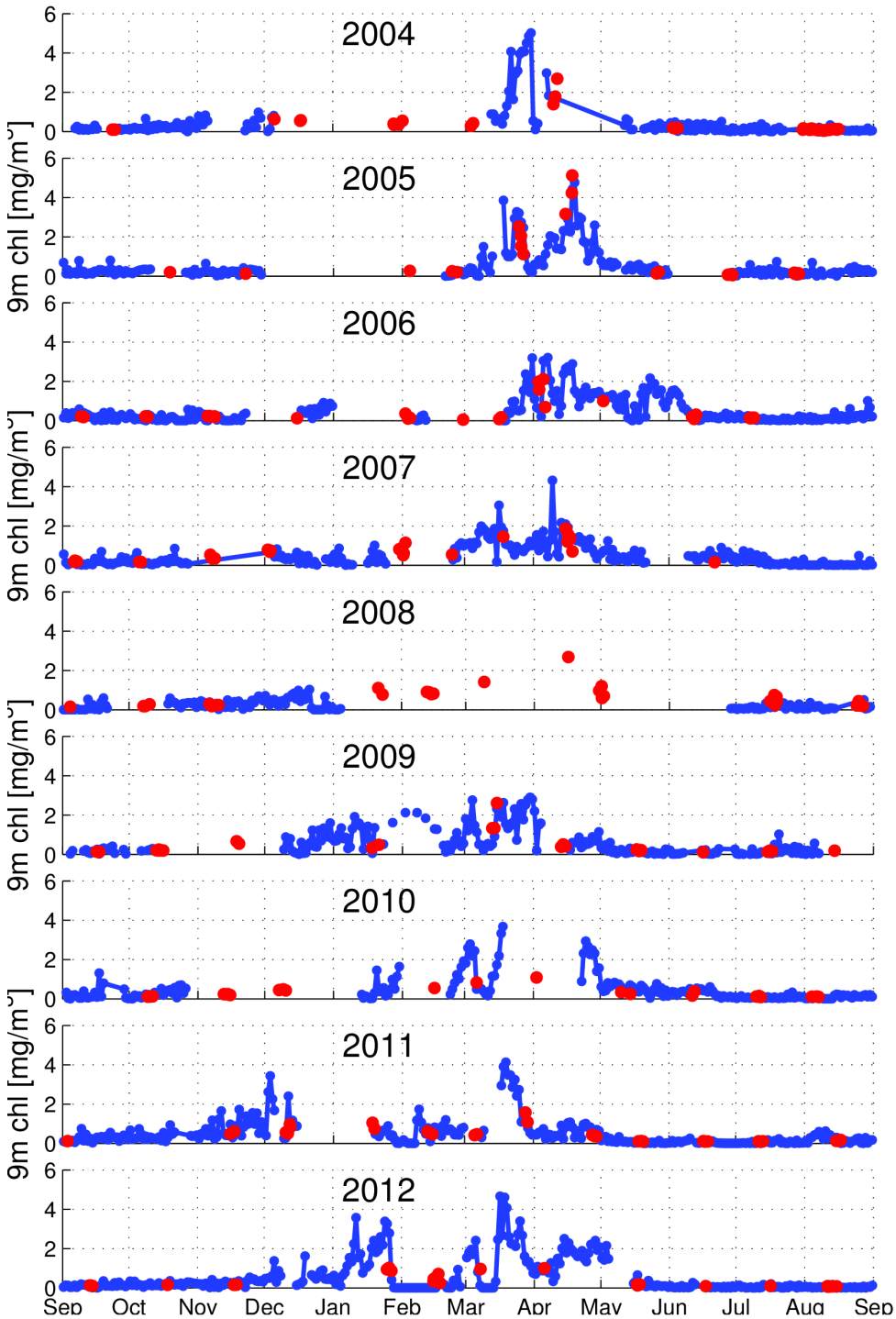

Figure 3.3: The full time series of model-returned (blue) and monthly hydrographic chlorophyll (red) for the 0-9 meter layer. Each year is plotted to from 1-Sept to 31-Aug in order to highlight the Spring Bloom.

Table 3.1: The calculated lags corresponding to highest correlation between years. This table should be read as,"The data from [Left column] occurred [value] days before the data from [Top Row] in their respective years". 2008 does not have enough data to form an appropriate correlation, and the median is the median for the lags in that column.

Year	2004	2005	2006	2007	2009	2010	2011	2012
2004	0 [days]	23	11	19	4	-6	-3	-7
2005	-23	0	-12	-9	-20	-29	-30	-30
2006	-11	12	0	3	-20	-28	-18	-19
2007	-19	9	-3	0	-11	-20	-21	-22
2009	-4	20	20	11	0	-10	-9	-9
2010	6	29	28	20	10	0	-1	-4
2011	3	30	18	21	9	1	0	-2
2012	7	30	19	22	9	4	2	0
Median	-2	21.5	14.5	15	2	8	6	8

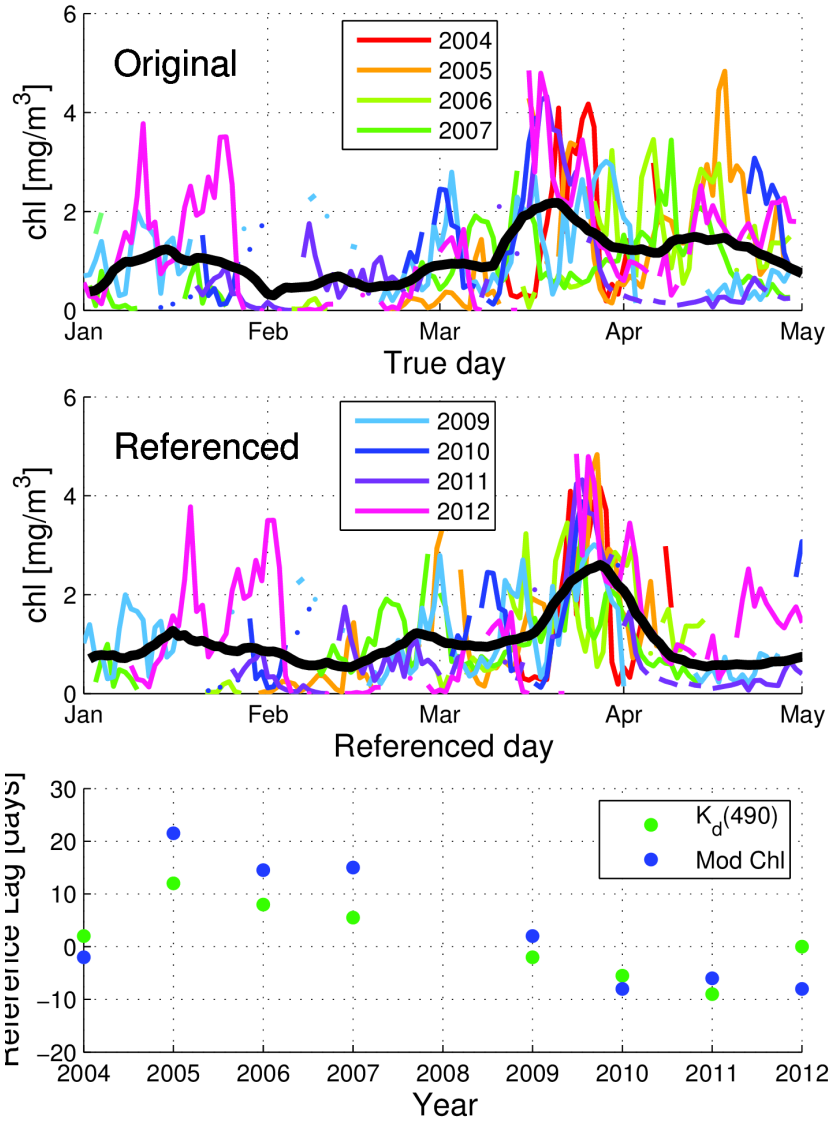

Figure 3.4: (top) The model-returned chlorophyll signal for each year, plotted from Jan-May. (middle) The same 5 months, referenced as per the lag-correlation technique described in the text. The legends in (top) and (bottom) give the years for each signal in both plots. (bottom) The reference lags, calculated using the model-returned

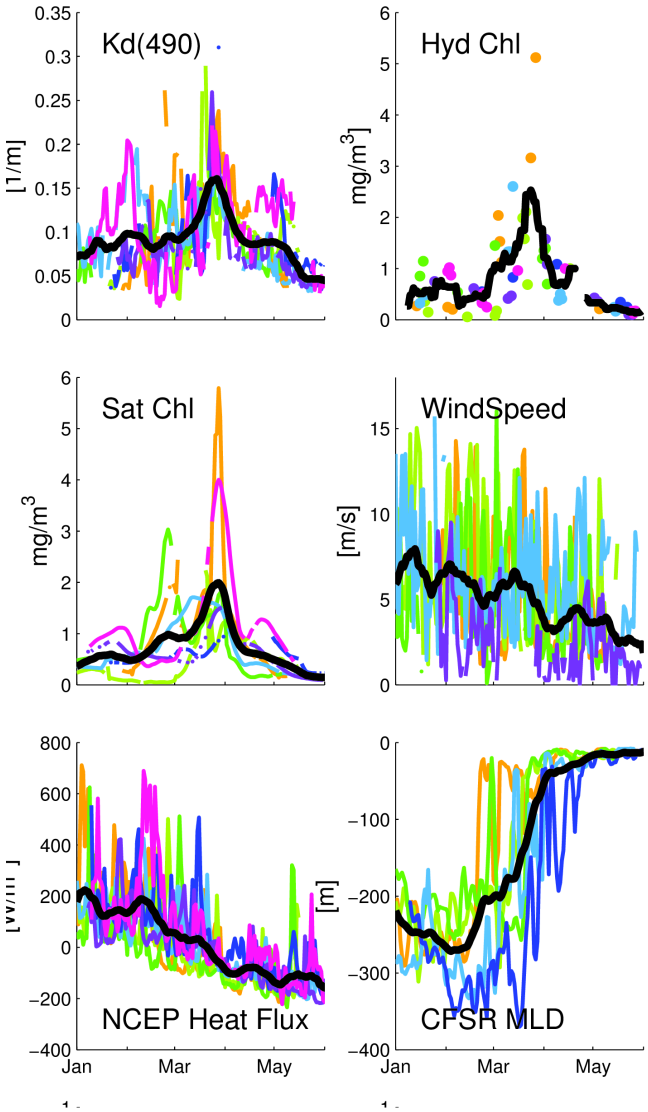

Figure 3.5: Various time series, each referenced to the model-derived reference lags; the colors correspond to the colors given in figure 3.5, and the black lines correspond to the annual cycle, calculated by the method described in the text. (top left) $K_d(490)$ is the diffuse attenuation of irradiance at 490nm. (top right) Hyd chl is the monthly hydrographic chlorophyll collected from bottles and analyzed using HPLC. (middle left) Sat Chl is an interpolated satellite product, normalized to the monthly values [*Antoine et al.*, 2008]. (middle right) Wind is the wind speed, collected at the Meteo Buoy. (bottom) NCEP heat flux and CFSR MLD are the daily-averaged reanalysis products.

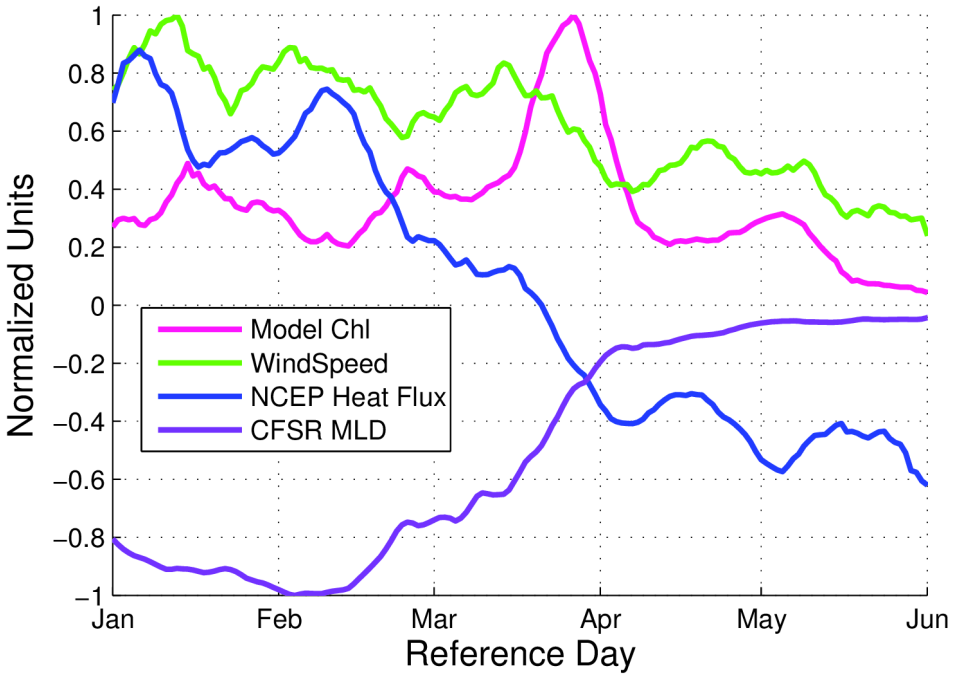

Figure 3.6:The mean cycle for Jan-June of the selected time series using the mooring-derived lags as reference (i.e. black lines in figure 3.4 and figure 3.5).

Table 3.2: The correlation between the signal and the calculated Jan-Jun cycle for the raw time series (column 1) and model-returned reference lags (column 2).(column 3) Is the significance of the difference between the two cycle correlations.

Variable	Raw time series r^2 (n)	Model-returned reference lags r^2 (n)	Fisher z transformation, significantly different
Model-returned chlorophyll	0.3205 (737)	**0.4167** **(738)**	p<0.05
$k_d(490\text{nm})$	0.3163 (764)	**0.4097** **(764)**	p<0.05
Hydrographic chlorophyll	0.3793 (76)	**0.4858** **(76)**	No
Satellite Chlorophyll Product	0.3833 (829)	**0.4570** **(829)**	p<0.1
Wind speed	0.1341 (621)	**0.1694** **(620)**	No
NCEP Total Heat Flux	**0.5560** **(1202)**	0.5446 (1202)	No
CFSR Mixed Layer Depth	**0.8041** **(901)**	0.7230 (901)	p<0.01

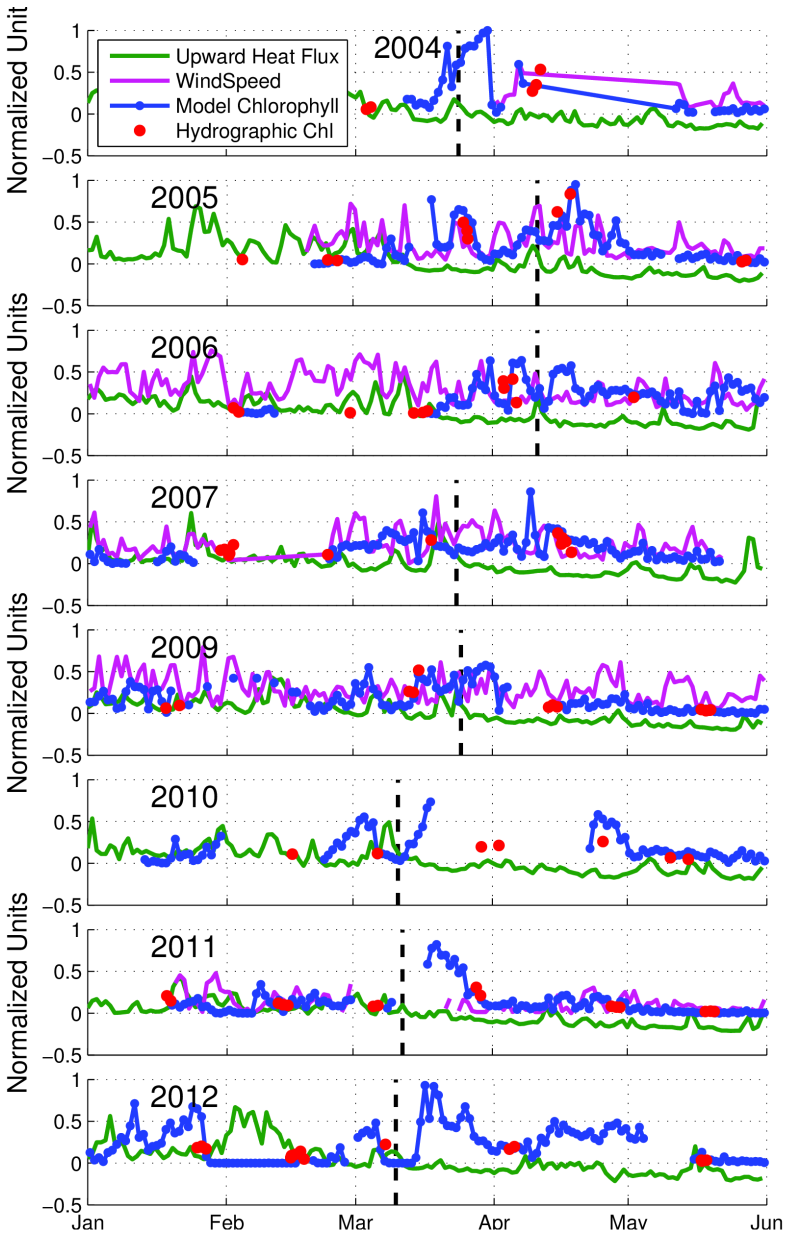

Figure 3.7: The reference-lagged time series for Jan-May for (blue) model-returned chlorophyll, (red dots) monthly chlorophyll, (green) total upwards heat flux, and (pink) wind speed measured at the Meteo Buoy. The hiatuses are defined as those events where model-returned chlorophyll drops, and several are highlighted by the vertically dashed lines.

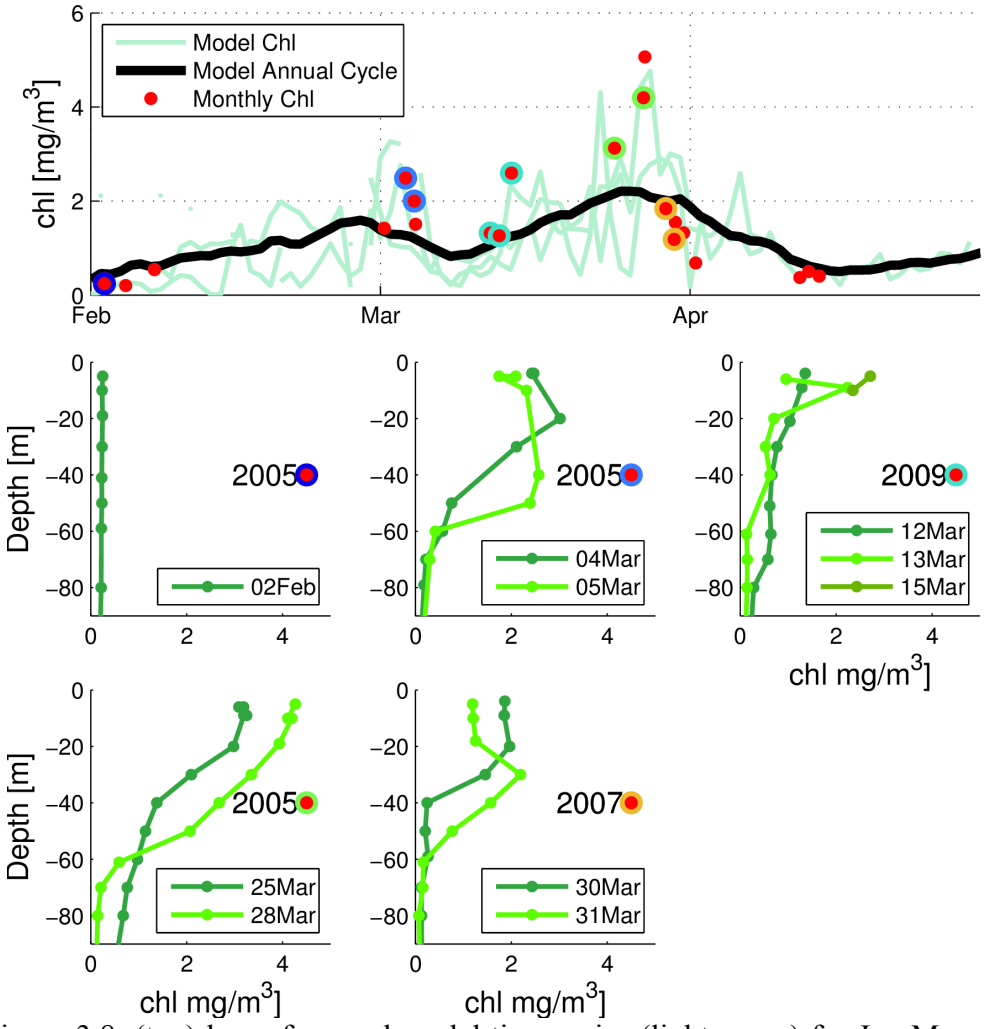

Figure 3.8: (top) lag-referenced model time series (light green) for Jan-May of 2005, 2007, and 2009, and the calculated cycle (black) for these three years. The red dots are the monthly chlorophyll for the same 0-9m layer, with the highlights corresponding to the profiles below the time series. The years for the given profiles are in their respective plots.

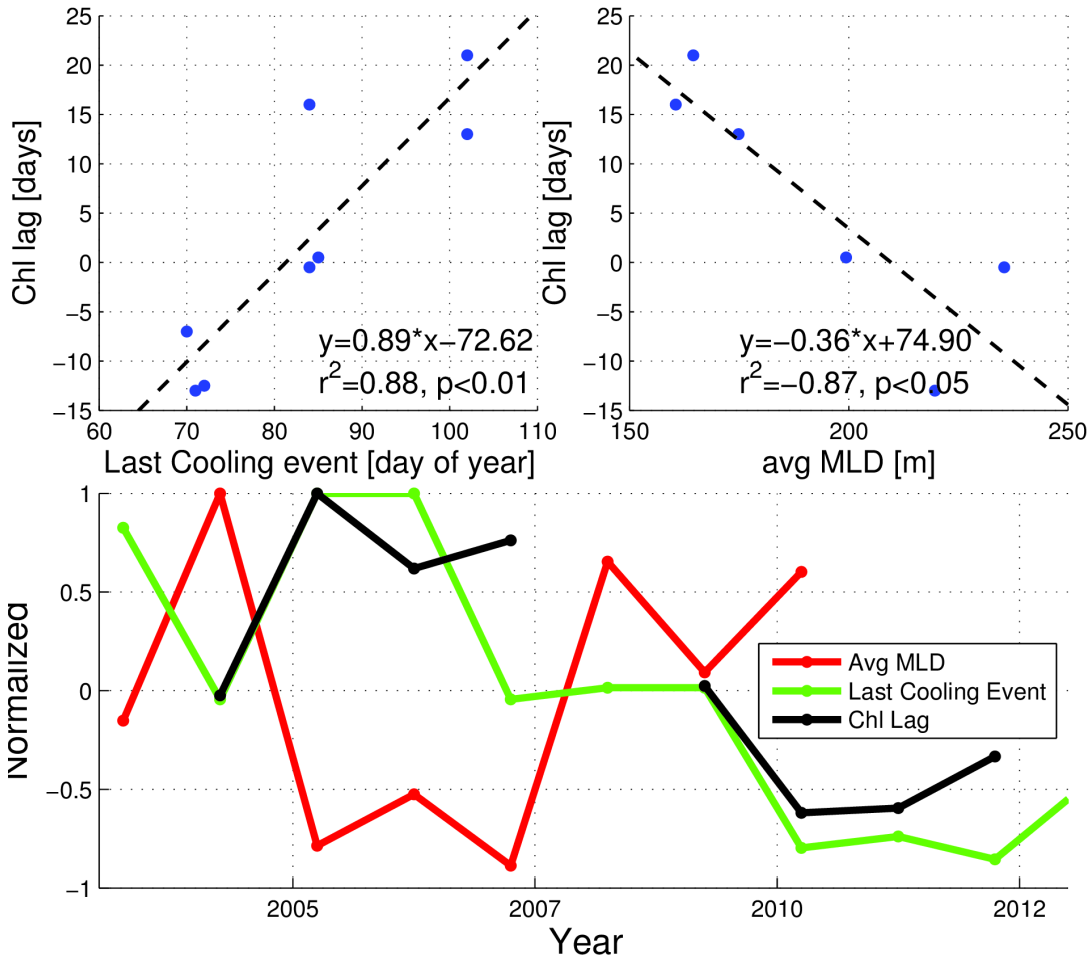

Figure 3.9: Relationship between chlorophyll lags and reanalysis products. (top left) Model-derived chlorophyll versus the last day of winter (Jan-April) with an upward heat flux greater than $100\,W/m^2$ (top right) Model-derived chlorophyll lags versus average MLD over Jan-May. (bottom) The normalized annual values for average MLD (red), day of last cooling event (green), and chlorophyll lag (black).

CONCLUSION

This work has attempted to answer two questions; How much chlorophyll is there? What is it doing? In Chapter 1, a new technique was developed describing layer averaged chlorophyll from moored measurements of diffuse attenuation. This technique is able to return hourly information of the longterm, vertically integrated chlorophyll concentration.

Chapter 2 coupled this model with current measurements, and examined the cross-shelf transport of chlorophyll near the Southern California Coast. The cross-shore eddy transport at the deeper mooring is dominated by large scale features, longer than 25 days, and totals 31.20 $g/(m\,day)$ offshore. The cross-shore eddy transport at the shallow mooring primarily occurs during consecutive upwelling events and is measured at 94.80 $g/(m\,day)$ offshore. As the region's CalCOFI program completes its 7th decade of measurements, these advective flux measurements can perhaps enhance the understanding of changing biogeochemical cycles in Coastal California.

Chapter 3 discussed the timing of the Spring Bloom in the Northwestern Mediterranean, describing how it varied by 30+ days over the 9 years sampled. It then showed mixing events can cause the 0-9m chlorophyll to decrease as the Spring Bloom develops. These events suggest that mixing of the surface chlorophyll concentration caused by surface cooling is diluting chlorophyll downward while the integrated chlorophyll continues to grow. Finally, a hypothesis for the delay in the 0-9m chlorophyll signature of the Spring Bloom is suggested. The last day of large cooling is shown to

significantly correlated with the delays in the Spring Bloom.

This work provides a new technique for determining chlorophyll concentration, and then uses this method to realize several important processes affecting oceanic chlorophyll.

WORKS CITED

Abbott, M. R., and R. M. Letelier (1998), Decorrelation Scales of Chlorophyll as observed from bio-optical drifters in the California Current, *Deep-Sea Res.*, *45*(2), 1639–1667, doi:S0967-0645(98)00046-0.

Andersen, V., and L. Prieur (2000), One-month study in the open NW Mediterranean Sea (DYNAPROC experiment, May 1995): overview of the hydrobiogeochemical structures and effects of wind events, *Deep Sea Res. Part Oceanogr. Res. Pap.*, *47*(3), 397–422, doi:10.1016/S0967-0637(99)00096-5.

Andersen, V., P. Nival, P. Caparroy, and A. Gubanova (2001), Zooplankton Community During the Transition from Spring Bloom to Oligotrophy in the Open NW Mediterranean and Effects of Wind Events. 1. Abundance and Specific Composition, *J. Plankton Res.*, *23*(3), 227–242, doi:10.1093/plankt/23.3.227.

Antoine, D., M. Chami, H. Claustre, F. D'Ortenzio, A. Morel, G. Becu, B. Gentili, F. Louis, J. Ras, E. Roussier, A.J. Scott (2006), BOUSSOLE: A Joint CNRS-INSU, ESA, CNES, and NASA Ocean Color Calibration and Validation Activity, *Tech. Rep.*, (NASA/TM-2006-214147).

Antoine, D., P. Guevel, J.-F. Desté, G. Bécu, F. Louis, A. J. Scott, and P. Bardey (2008), The "BOUSSOLE" Buoy—A New Transparent-to-Swell Taut Mooring Dedicated to Marine Optics: Design, Tests, and Performance at Sea, *J. Atmospheric Ocean. Technol.*, *25*(6), 968–989, doi:10.1175/2007JTECHO563.1.

Behrenfeld, M. J., and E. S. Boss (2014), Resurrecting the Ecological Underpinnings of Ocean Plankton Blooms, *Annu. Rev. Mar. Sci.*, *6*(1), 167–194, doi:10.1146/annurev-marine-052913-021325.

Bernardello, R., J. G. Cardoso, N. Bahamon, D. Donis, I. Marinov, and A. Cruzado (2012), Factors controlling interannual variability of vertical organic matter export and phytoplankton bloom dynamics – a numerical case-study for the NW Mediterranean Sea, *Biogeosciences*, *9*(11), 4233–4245, doi:10.5194/bg-9-4233-2012.

Bograd, S. J., D. A. Checkley, and W. S. Wooster (2003), CalCOFI: a half century of physical, chemical, and biological research in the California Current System, *Deep Sea Res. Part II Top. Stud. Oceanogr.*, *50*(14–16), 2349–2353, doi:10.1016/S0967-0645(03)00122-X.

Bond, N. A., M. F. Cronin, H. Freeland, and N. Mantua (2015), Causes and impacts of the 2014 warm anomaly in the NE Pacific: 2014 WARM ANOMALY IN THE NE PACIFIC, *Geophys. Res. Lett.*, *42*(9), 3414–3420, doi:10.1002/2015GL063306.

Bricaud, A., A. Morel, M. Babin, K. Allali, and H. Claustre (1998), Variations of light

absorption by suspended particles with chlorophyll a concentration in oceanic (case 1) waters: Analysis and implications for bio-optical models, *J. Geophys. Res. Oceans*, *103*(C13), 31033–31044, doi:10.1029/98JC02712.

Bricaud, A., A. ..Morel, and L. Prieur (1981), Absorption by dissolved organic matter of the sea (yellow substance) in the UV and visible domains, edited by B. Hales, W.-J. Cai, B. G. Mitchell, C. L. Sabine, and and O. Schofield, *Limnol. Oceanogr.*, *26*, 43–53.

Brody, S. R., M. S. Lozier, and J. P. Dunne (2013), A comparison of methods to determine phytoplankton bloom initiation, *J. Geophys. Res. Oceans*, *118*(5), 2345–2357, doi:10.1002/jgrc.20167.

Brown, C.A., Y. Huot, M.J. Purcell, J.J. Cullen, and M. R. Lewis (2004), Mapping coastal optical and biogeochemical variability using an autonomous underwater vehicle and a new bio-optical inversion algorithm, *Limnol Ocean.-Methods*, *2*, 262–281.

Cattiaux, J., R. Vautard, C. Cassou, P. Yiou, V. Masson-Delmotte, and F. Codron (2010), Winter 2010 in Europe: A cold extreme in a warming climate: COLD WINTER 2010 IN EUROPE, *Geophys. Res. Lett.*, *37*(20), n/a-n/a, doi:10.1029/2010GL044613.

Centurioni, L. R., J. C. Ohlmann, and P. P. Niiler (2008), Permanent Meanders in the California Current System, *J. Phys. Oceanogr.*, *38*(8), 1690–1710, doi:10.1175/2008JPO3746.1.

Chavez, F. P., N. Gruber, B. Hales, M. Hernandez, and and D. Ianson (2008), North America's Pacific Coast, edited by B. Hales, W.-J. Cai, B. G. Mitchell, C. L. Sabine, and and O. Schofield, *North Am. Cont. Margins Synth. Plan. Workshop*, 35–48.

Checkley Jr., David M., and J. A. Barth (2009), Patterns and processes in the California Current System, *Prog. Oceanogr.*, *83*(1–4), 49–64, doi:http://dx.doi.org/10.1016/j.pocean.2009.07.028.

Clark, D. K., M. E. Fenholz, M. A. Yarbrough, B. C. Johnson, S. W. Brown, Y. S. Kim, and R. A. Barnes (2002), Overview of the radiometric calibration of MOBY, in *Proceedings of SPIE Reprent*, vol. 4483, Society of Photo-Optical Instrumentation, San Diego.

Cronin, M. F., and W. S. Kessler (2002), Seasonal and interannual modulation of mixed layer variability at 0°, 110°W, *Deep Sea Res. Part Oceanogr. Res. Pap.*, *49*(1), 1–17, doi:10.1016/S0967-0637(01)00043-7.

Dever, E. P., C. E. Dorman, and J. L. Largier (2006), Surface boundary-layer variability

off Northern California, USA, during upwelling, *Deep Sea Res. Part II Top. Stud. Oceanogr.*, *53*(25–26), 2887–2905, doi:10.1016/j.dsr2.2006.09.001.

Franks, P. J. S. (2005), Plankton patchiness, turbulent transport and spatial spectra, *Mar. Ecol. Prog. Ser.*, *294*, 295–309.

Gordon, H. R. (1989), Can the Lambert-Beer law be applied to the diffuse attenuation coefficient of ocean water?, *Limnol Ocean.*, *34*(8), 1389–1409, doi:10.1364/AO.36.008710.

Gregg, Watson W., and K. L. Carder (1990), A simple spectral solar irradiance model for cloudless maritime atmospheres, *Limnol Ocean.*, *35*(8), 1657–1675, doi:10.4319/lo.1990.35.8.1657.

Henson, S. A., J. P. Dunne, and J. L. Sarmiento (2009), Decadal variability in North Atlantic phytoplankton blooms, *J. Geophys. Res.*, *114*(C4), doi:10.1029/2008JC005139.

Horwood, J. (1981), Variation of fluorescence, particle-size groups, and environmental parameters in the southern North Sea, *J. Cons.*, *39*(3), 261–270, doi:10.1093/icesjms/39.3.261.

Jerlov, N. G. (1968), *Optical Oceanography*, Elsevier Oceanography Series, Elsevier Science.

Kahru, M., E. Di Lorenzo, M. Manzano-Sarabia, and B. G. Mitchell (2012), Spatial and temporal statistics of sea surface temperature and chlorophyll fronts in the California Current, *J. Plankton Res.*, doi:10.1093/plankt/fbs010.

Kalnay, E., M. Kanamitsu, R. Kistler, W. Collins, D. Deaven, L. Gandin, M. Iredell, S. Saha, G. White, J. Woollen, Y. Zhu, A. Leetmaa, R. Reynolds (1996), The NCEP/NCAR 40-Year Reanalysis Project, *Bull. Am. Meteorol. Soc.*, *77*(3), 437–471, doi:10.1175/1520-0477(1996)077<0437:TNYRP>2.0.CO;2.

Keister, J. E., W. T. Peterson, and S. D. Pierce (2009), Zooplankton distribution and cross-shelf transfer of carbon in an area of complex mesoscale circulation in the northern California Current, *Deep Sea Res. Part Oceanogr. Res. Pap.*, *56*(2), 212–231, doi:10.1016/j.dsr.2008.09.004.

Kheireddine, M., and D. Antoine (2014), Diel variability of the beam attenuation and backscattering coefficients in the northwestern Mediterranean Sea (BOUSSOLE site), *J. Geophys. Res. Oceans*, *119*(8), 5465–5482, doi:10.1002/2014JC010007.

Killworth, P. D. (1983), Deep convection in the World Ocean, *Rev. Geophys.*, *21*(1), 1, doi:10.1029/RG021i001p00001.

Kirk, J. T. O. (2010), *Light and Photosynthesis in Aquatic Ecosystems*, Light and Photosynthesis in Aquatic Ecosystems, Cambridge University Press.

Landry, M. R., M. D. Ohman, R. Goericke, M. R. Stukel, and K. Tsyrklevich (2009), Lagrangian studies of phytoplankton growth and grazing relationships in a coastal upwelling ecosystem off Southern California, *Prog. Oceanogr.*, *83*(1–4), 208–216, doi:http://dx.doi.org/10.1016/j.pocean.2009.07.026.

Lee, Z.-P., K.-P. Du, and R. Arnone (2005), A model for the diffuse attenuation of downwelling irradiance., *J. Geophys. Res.*, *110*, doi:10.1029/2004JC002275.

Marcel, B., R. S Collin, and C. J John (2008), *Real-time Coastal Observing Systems for Marine Ecosystem Dynamics and Harmful Algal Blooms: theory, instrumentation and modelling*, UNESCO.

Marty, J.-C., J. Chiavérini, M.-D. Pizay, and B. Avril (2002), Seasonal and interannual dynamics of nutrients and phytoplankton pigments in the western Mediterranean Sea at the DYFAMED time-series station (1991–1999), *Deep Sea Res. Part II Top. Stud. Oceanogr.*, *49*(11), 1965–1985, doi:10.1016/S0967-0645(02)00022-X.

Matthews, D. K., and W. J. Emery (2009), Velocity observations of the California Current derived from satellite imagery, *J. Geophys. Res.*, *114*(C8), doi:10.1029/2008JC005029.

Mitchell, B. G., A. Bricaud, K. Carder, J. Cleveland, G. Ferrari, R. Gould, M. Kahru, M. Kishino, H. Maske, T. Moisan, L. Moore, N. Nelson, D. Phinney, R. Reynolds, H. Sosik, D. Stramski, S. Tassan, C. Trees, A. Weidemann, J. Wieland, and A. Vodacek (2000), Determination of spectral absorption coefficients of particles, dissolved material and phytoplankton for discrete water samples, edited by G. S. Fargion and J. L. Mueller, *Ocean Opt. Protoc. Satell. Ocean Color Sens. Valid. Revis. 2*, 125–153.

Mobley, C. D. (1994), *Light and water: radiative transfer in natural waters*, Academic Press.

Mobley, C. D., and L. Sunman (2012), Hydrolight 5.1 and Ecolight 5.1 Technical Documentation,

Morel, A. (1974), Optical Properties of pure water and pure seawater, in *Optical Aspects of Oceanography*, edited by N. G. Jerlov and E. S. Nielsen, pp. 1–24, Academic.

Morel, A., and S. Maritorena (2001), Bio-optical properties of oceanic waters: A reappraisal, *J. Geophys. Res. Oceans*, *106*(C4), 7163–7180, doi:10.1029/2000JC000319.

Musavi, M. T., R. L. Miller, H. Ressom, and P. Natarajan (2002), Neural network-based estimation of chlorophyll-a concentration in coastal waters, vol. 4488, pp. 176–183.

Nagamani, P. V., P. Chauhan, and R. M. Dwivedi (2007), Estimation of chlorophyll-A concentration using an artificial neural network (ANN)-based algorithm with oceansat-I OCM data, *J. Indian Soc. Remote Sens.*, *35*(3), 201–207, doi:10.1007/BF03013488.

Nahorniak, Jasmine S. ..Mark R.Abbott, Ricardo M.Letelier, and W. S. Pegau (2001), Analysis of a Method to Estimate Chlorophyll-a Concentration from Irradiance Measurements at Varying Depths., *J. Atmospheric Ocean. Technol.*, *18*(12), 2063–2073, doi:10.1029/JC090iC06p11779.

Nelder, J. A., and R. Mead (1965), A Simplex Method for Function Minimization, *Comput. J.*, *7*(4), 308–313, doi:10.1093/comjnl/7.4.308.

Neumann, Gerhard, and W. J. Pierson (1966), *Principles of Physical Oceanography*, Prentice-Hall, Englewood Cliffs, N.J.

Organelli, E., A. Bricaud, D. Antoine, and A. Matsuoka (2014), Seasonal dynamics of light absorption by chromophoric dissolved organic matter (CDOM) in the NW Mediterranean Sea (BOUSSOLE site), *Deep Sea Res. Part Oceanogr. Res. Pap.*, *91*, 72–85, doi:10.1016/j.dsr.2014.05.003.

Pope, R. M., and E. S. Fry (1997), Absorption spectrum (380–700 nm) of pure water. II. Integrating cavity measurements, *Appl Opt*, *36*(33), 8710–8723, doi:10.1364/AO.36.008710.

Powell, T. M., and A. Okubo (1994), Turbulence, Diffusion and Patchiness in the Sea, *Philos. Trans. R. Soc. B Biol. Sci.*, *343*(1303), 11–18, doi:10.1098/rstb.1994.0002.

Price, J. F., R. A. Weller, and R. Pinkel (1986), Diurnal cycling: Observations and models of the upper ocean response to diurnal heating, cooling, and wind mixing, *J. Geophys. Res.*, *91*(C7), 8411, doi:10.1029/JC091iC07p08411.

Rykaczewski, R., and J. P. Dunne (2010), Enhanced nutrient supply to the California Current Ecosystem with global warming and increased stratification in an earth system model, *Geophys Res Lett*, *37*(L21606), doi:10.1073/pnas.0711777105.

Rykaczewski, R. R., and D. M. Checkley (2008), Influence of ocean winds on the pelagic ecosystem in upwelling regions, *Proc. Natl. Acad. Sci.*, *105*(6), 1965–1970, doi:10.1073/pnas.0711777105.

Saha, S., S. Moorthi, H. Pan, X. Wu, J. Wang, S. Nadiga, P. Tripp, R. Kistler, J. Woollen,

D. Behringer, H. Liu, D. Stokes, R. Grumbine, G. Gayno, J. Wang, Y. Hou, H. Chuang, H. H. Juang, J. Sela, M. Iredell, R. Treadon, D. Kleist, P. V. Delst, D. Keyser, J. Derber, M. Ek, J. Meng, H. Wei, R. Yang, S. Lord, H. V. D. Dool, A. Kumar, W. Wang, C. Long, M. Chelliah, Y. Xue, B. Huang, J. Schemm, W. Ebisuzaki, R. Lin, P. Xie, M. Chen, S. Zhou, W. Higgins, C. Zou, Q. Liu, Y. Chen, Y. Han, L. Cucurull, R. W. Reynolds, G. Rutledge, and M. Goldberg (2010), The NCEP Climate Forecast System Reanalysis, *Bull. Am. Meteorol. Soc.*, *91*(8), 1015–1057, doi:10.1175/2010BAMS3001.1.

Sallée, J.-B., J. Llort, A. Tagliabue, and M. Lévy (2015), Characterization of distinct bloom phenology regimes in the Southern Ocean, *ICES J. Mar. Sci. J. Cons.*, *72*(6), 1985–1998, doi:10.1093/icesjms/fsv069.

Scharffenberg, M. G., and D. Stammer (2011), Statistical parameters of the geostrophic ocean flow field estimated from the Jason-1–TOPEX/Poseidon tandem mission, *J. Geophys. Res.*, *116*(C12), doi:10.1029/2011JC007376.

Sheskin, D. J. (2003), *Handbook of Parametric and Nonparametric Statistical Procedures: Third Edition*, CRC Press.

Sosik, H. M., and B. G. Mitchell (1995), Light absorption by phytoplankton, photosynthetic pigments and detritus in the California Current System, *Deep-Sea Res. I*, *42*, 1717–1748, doi:10.1016/0967-0637(95)00081-G.

Stukel, M. R., M. R. Landry, C. R. Benitez-Nelson, and R. Goericke (2011), Trophic cycling and carbon export relationships in the California Current Ecosystem, *Limnol. Oceanogr.*, *56*(5), 1866–1878, doi:10.4319/lo.2011.56.5.1866.

Thomson, R. E., and W. J. Emery (2001), *Data Analysis Methods in Physical Oceanography*, 2nd Revised edition., edited by W. J. Emery and R. E. Thomson, Elsevier Science, Amsterdam ; New York.

Twardowski, M. S., E. Boss, J. M. Sullivan, and P. L. Donaghay (2004), Modeling the spectral shape of absorption by chromophoric dissolved organic matter, *Mar. Chem.*, *89*(1–4), 69–88, doi:http://dx.doi.org/10.1016/j.marchem.2004.02.008.

Welch, P. (1967), The use of fast Fourier transform for the estimation of power spectra: A method based on time averaging over short, modified periodograms, *IEEE Trans. Audio Electroacoustics*, *15*(2), 70–73, doi:10.1109/TAU.1967.1161901.

Weller, R. A., A. S. Fischer, D. L. Rudnick, C. C. Eriksen, T. D. Dickey, J. Marra, C. Fox, and R. Leben (2002), Moored observations of upper-ocean response to the monsoons in the Arabian Sea during 1994–1995, *Deep Sea Res. Part II Top. Stud. Oceanogr.*, *49*(12), 2195–2230, doi:10.1016/S0967-0645(02)00035-8.

Wilson, S., U. Send, B. G. Mitchell, and D. Antoine (2016), A new bulk chlorophyll retrieval using paired measurements of wavelength-specific diffuse attenuation, Doctoral, University of California, San Diego, La Jolla.

Winant, C. D., and C. E. Dorman (1997), Seasonal patterns of surface wind stress and heat flux over the Southern California Bight, *J. Geophys. Res. Oceans*, *102*(C3), 5641–5653, doi:10.1029/96JC02801.

Xing, X., A. Morel, H. Claustre, F. D'Ortenzio, and A. Poteau (2012), Combined processing and mutual interpretation of radiometry and fluorometry from autonomous profiling Bio-Argo floats: 2. Colored dissolved organic matter absorption retrieval, *J. Geophys. Res. Oceans*, *117*(C4), doi:10.1029/2011JC007632.

Zaba, K. D., and D. L. Rudnick (2016), The 2014-2015 warming anomaly in the Southern California Current System observed by underwater gliders: The 2014-2015 Warm Anomaly in the CCS, *Geophys. Res. Lett.*, *43*(3), 1241–1248, doi:10.1002/2015GL067550.

Zaneveld, J. R. V. (1989), An asymptotic closure theory for irradiance in the sea and its inversion to obtain the inherent optical properties, *Limnol. Oceanogr.*, *34*(8), 1442–1452, doi:10.4319/lo.1989.34.8.1442.

Zaneveld, J. R. V., E. Boss, and A. Barnard (2001), Influence of surface waves on measured and modeled irradiance profiles, *Appl. Opt.*, *40*(9), 1442, doi:10.1364/AO.40.001442.